NASA
Technical
Paper
2579

April 1986

Effects of Upper-Surface Nacelles on Longitudinal Aerodynamic Characteristics of High-Wing Transport Configuration

Lawrence E. Putnam

NASA

NASA Technical Paper 2579

1986

Effects of Upper-Surface Nacelles on Longitudinal Aerodynamic Characteristics of High-Wing Transport Configuration

Lawrence E. Putnam

Langley Research Center
Hampton, Virginia

NASA
National Aeronautics
and Space Administration

Scientific and Technical Information Branch

Summary

An investigation has been conducted in the Langley 16-Foot Transonic Tunnel to determine the effects of installing and streamline contouring upper-surface nacelles on the longitudinal aerodynamic characteristics of a high-wing transport configuration. Also investigated were the effects of adding a fairing under the nacelle. The investigation was conducted at free-stream Mach numbers from 0.60 to 0.83 at angles of attack from $-2°$ to $4°$. Flow-through nacelles were used.

The results of the investigation indicated that installing straight upper-surface nacelle configurations caused the drag of the configuration to increase more than twice the friction drag of the nacelles. Streamline contouring these nacelles in an attempt to make the inboard side of the nacelle essentially invisible to the wing-fuselage flow substantially reduced the interference drag. The installation drag of the contoured nacelles was about 1.5 times the friction drag. The addition of an undernacelle fairing had essentially no effect on the drag of the configuration.

Introduction

If the competitive position of the United States aircraft industry is to be maintained, future transport airplanes must have substantially better performance than today's airplanes. Because today's airplanes are already very efficient, the task of improving their performance will be very demanding and will require the development and application of many new and innovative technologies. Among the technologies that must be improved are the methods used to install the engine on the airframe. Transport airplanes in the future will have advanced high-aspect-ratio (> 10) wing designs and larger engines because of higher bypass ratios for increased engine efficiency. This combination results in an engine that is considerably larger relative to the wing chord than present-day designs. As a result, the integration of the engine will become considerably more difficult.

Therefore, the NASA Langley Research Center has initiated a research program to study the effects of nacelle location, nacelle shape, and pylon geometry on the interference drag associated with installing the engine on transport airplane configurations. Reference 1 presents data that illustrate the sensitivity of several geometric parameters on the nacelle/pylon/wing interference drag. Studies have been conducted to find alternate nacelle arrangements for eliminating the unfavorable interference drag associated with engine installation. (See refs. 2 through 6.) These studies investigated the effects of conventional under-the-wing pylon-mounted nacelles (ref. 2), pylon-mounted over-the-wing nacelles (refs. 3 and 4), and nacelles mounted under the wing with the nacelle inlet at about 70 percent of the local chord (refs. 5 and 6) on the aerodynamic characteristics of a high-wing transport airplane configuration. These investigations also explored the effects of nacelle contouring and pylon contouring on propulsion-system interference drag. All these studies except reference 6 used long-duct, mixed-flow nacelles. Reference 6 investigated the effects of under-the-wing separate-flow nacelles on engine installation aerodynamics. Reference 7 studied the effects on engine installation aerodynamics of a nacelle designed to encourage natural laminar flow.

Upper-surface nacelles have also been studied to determine their potential as a viable engine installation arrangement. (See refs. 8 through 10, for example.) Typically, this engine location has been suggested for short-haul high-wing transports or for STOL airplane configurations in which the aerodynamic benefits of upper-surface blowing can be used to reduce takeoff and landing lengths. With increasing engine size relative to the wing, raising the engine location until the exhaust blows over the wing may provide a means for overcoming the clearance problem between the bottom of the nacelle and the ground for low-wing transport configurations.

Because of the high velocities over the upper surface of the wing, the use of upper-surface nacelles can result in significant interference drag penalties. References 11 and 12 indicate that contouring the nacelle along streamlines of the flow over the wing can reduce these drag penalties.

The purpose of the present investigation is, therefore, to determine the effects of installing an upper-surface nacelle and the effects of streamline contouring this nacelle on the aerodynamic characteristics of a transport airplane configuration. In order to provide a consistent basis for comparing this engine installation arrangement with other possible locations, the same high-wing transport of references 1 through 7 was used. The investigation was conducted in the Langley 16-Foot Transonic Tunnel at Mach numbers from 0.60 to 0.83 at angles of attack up to about $4°$. Flow-through nacelles were used.

Symbols

A_c	cross-sectional area at given longitudinal location inside flow-through nacelle
$A_{c,s}$	cross-sectional area inside flow-through nacelle at location of static pressure ring
A_{exit}	cross-sectional area at exit of nacelle flow-through duct

A_w	wetted area inside flow-through duct from inlet to a given longitudinal location
A_{wet}	total internal wetted area of flow-through duct
b	wingspan
C_D	drag coefficient, Drag/$q_\infty S$
$C_{D,i}$	internal drag coefficient for two nacelles, Internal drag/$q_\infty S$
C_F	total skin-friction coefficient based on mean dynamic pressure inside flow-through duct
C_L	lift coefficient, Lift/$q_\infty S$
C_m	pitching-moment coefficient about 25 percent of wing mean aerodynamic chord, Pitching moment/$q_\infty S\bar{c}$
C_p	pressure coefficient, $(p - p_\infty)/q_\infty$
$C_{p,\text{cr}}$	critical pressure coefficient
c	local chord
c_{av}	average chord
c_f	local skin-friction coefficient
$\bar{c}$	mean aerodynamic chord
D_i	internal drag
F_i	internal thrust
$F_{i,f}$	internal thrust force due to skin friction
i_n	incidence angle of nacelle relative to model body axis system
L	length of duct of flow-through nacelle
M	local Mach number inside flow-through duct
M_s	local Mach number at static pressure ring inside duct
M_∞	free-stream Mach number
$\bar{M}$	average Mach number inside flow-through duct
$\dot{m}$	mass flow through duct
$\dot{m}_\infty$	free-stream mass flow based on inlet highlight area
N_{Re}	Reynolds number
p	local static pressure
p_{exit}	average static pressure at exit of flow-through duct
$p_{t,\infty}$	free-stream stagnation pressure
p_∞	free-stream static pressure
$\bar{p}_s$	average static pressure at static pressure ring inside duct
q	local dynamic pressure inside flow-through duct
q_∞	free-stream dynamic pressure
$\bar{q}$	average dynamic pressure inside flow-through duct
R	gas constant
r	radius
S	wing reference area (trapezoidal planform), 3416.66 cm^2
$T_{t,\infty}$	free-stream stagnation temperature
t	maximum local airfoil thickness
V_{exit}	average velocity at exit of flow-through duct
V_{inlet}	average velocity at inlet of flow-through duct
V_∞	free-stream velocity
x	streamwise distance from wing leading edge parallel to wing reference plane, positive rearward
y	spanwise distance from fuselage centerline
z	vertical distance normal to wing reference plane, positive upward
α	angle of attack, deg
ϵ	angle between wing reference plane and straight line through local wing section leading edge and average of trailing-edge ordinates, positive leading edge up
η	fraction of wing semispan, $2y/b$
ϕ	meridian angle about axis of symmetry of left nacelle, advances clockwise from 0 at top of nacelle when looking upstream

Subscript:

max	maximum

Abbreviations:

BL	buttline
FS	fuselage station
LER	leading-edge radius
MHB	maximum half-breadth
NS	nacelle station
NWL	nacelle waterline
WL	waterline
WRP	wing reference plane
USBC	configuration with contoured nacelle
USBC-F	configuration with contoured nacelle and undernacelle fairing
USBS	configuration with straight nacelle

Experimental Apparatus and Procedures

Wind Tunnel

This investigation was conducted in the Langley 16-Foot Transonic Tunnel, which is an atmospheric, single-return wind tunnel with continuous air exchange for cooling. The test section is octagonal with eight longitudinal slots. The tunnel is capable of operating at Mach numbers from 0.20 to 1.30. The average Reynolds number per meter ranges from 4.5×10^6 at a free-stream Mach number of 0.20 to 12.6×10^6 at a free-stream Mach number of 1.30. A detailed description of the tunnel can be found in references 13 and 14.

Model

A sketch presented in figure 1 provides the overall dimensions of the transport model. This figure shows the basic configuration with straight nacelles. The configuration has a high-wing and a T-tail arrangement.

Fuselage. The fuselage was circular in cross section, had an ellipsoid forebody, and had a fineness ratio of 6.89. Geometric details of the fuselage are provided in figure 2. Since the model was sting mounted in the wind tunnel, it was necessary to modify the aft geometry of the fuselage to provide adequate clearance for the sting. Details of the sting cavity cutout are given in figure 2(b).

Wing. The wing planform dimensions and other details are provided in figure 3. The wing had an aspect ratio of 7.52, a taper ratio of 0.328, and the quarter chord was swept 30°. Dihedral and incidence angles were both 0°. The wing reference plane intersected the vertical plane of symmetry of the model at WL 8.255. (See fig. 1.) The wing shape was defined by the supercritical airfoil sections located at the fuselage side, the planform break, and the tip, as shown in figure 4. Table I provides a listing of the airfoil coordinates relative to the wing reference plane at these span stations. At other wingspan stations the wing airfoil coordinates can be determined by linear interpolation between adjacent defining sections along lines of constant x/c. The variation of wing thickness and twist with wing semispan location is presented as figure 5. The wing has a washout of approximately 3.7°.

Figure 6 shows the geometry of the wing-fuselage fairing. This fairing was designed to provide smooth shape transitions and to control boundary-layer growth in the wing-fuselage juncture. (See ref. 2.)

Empennage. Details of the vertical tail are provided in figure 7. The vertical tail had symmetrical airfoil coordinates, which are given in the table in figure 7. The maximum percent thickness of the airfoils did not change with waterline. A bullet fairing was mounted on top of the vertical tail. The nose and afterbody of this fairing were ogives with the same profile radius and length. The horizontal tail was attached to this bullet fairing. The horizontal tail, shown in figure 8, was a one-piece, all-movable, negatively cambered surface. The airfoil coordinates for the horizontal tail are also presented in figure 8. The maximum percent thickness of the airfoils was the same at all span stations. A negatively cambered airfoil was chosen for the horizontal tail in order to counteract the increased nose-down pitching moment of the supercritical wing as compared with conventional designs. Provisions were made in the model for deflecting the horizontal tail. However, in the present investigation only an incidence angle of 0° was used.

Nacelle installations. Two upper-surface nacelle configurations were tested: a straight nacelle and a contoured nacelle. In addition, an undernacelle fairing was tested with the contoured nacelle. A sketch showing the straight nacelle (USBS) installed on the wing is presented as figure 9, and photographs of the model with the straight nacelle mounted in the Langley 16-Foot Transonic Tunnel are presented as figure 10. The centerline of the nacelle was located at BL 19.812 and at WL 12.191. The nacelle was mounted parallel to the wing reference plane. The inlet section, the first 20.32 cm of the nacelle, was removable and was used on all three nacelle configurations. Details of this inlet section, designated as

NACA 1-83-75, are given in figure 11. The ratio of highlight diameter to maximum diameter for the inlet was 0.83 and the external length was 0.75 maximum diameter. The contraction ratio of the inlet (the ratio of highlight area to throat area) was 1.09.

A sketch showing the contoured nacelle (USBC) mounted on the wing is presented as figure 12. This figure also provides details of the undernacelle fairing used to obtain configuration USBC-F. The interchangeable inlet section was modified by the addition of a fairing on the inboard side when used with the contoured nacelle configurations. Photographs of the contoured nacelle configuration and the contoured nacelle configuration with undernacelle fairing are presented as figure 13. The inlet section of these nacelle configurations is drooped 1.5° and canted inboard 1.2°. The center of the nozzle exit is located at BL 20.574 and WL 12.192. Cross-sectional drawings of the contoured nacelle aft of FS 35.560 are presented in figure 14. This figure also shows details of the undernacelle fairing. (Note that cross sections for the straight nacelle configuration aft of FS 51.036 can be obtained from these contoured nacelle cross sections by translating to the centerline of the straight nacelle as required.)

Instrumentation

The model used in this investigation was mounted on a conventional six-component strain-gauge balance that measured its overall aerodynamic force and moments. Pressure orifices were located on the wing upper and lower surfaces at nine spanwise stations and along the top of the fuselage over the length of the wing root chord. Pressure orifices were also located on the nacelles. The nacelle pressure orifices were located in longitudinal rows lying in several meridian planes. There were also four pressure orifices located inside the nacelle approximately 6.350 cm downstream of the inlet lip. These internal nacelle pressures were required for the calculation of nacelle internal drag. The wing and nacelle pressures were measured with 12 pressure-scanning units mounted in the hollow removable nose section of the fuselage. Each scanning unit contained a transducer and was capable of measuring 47 pressures sequentially.

Pressures were measured at 16 positions in the fuselage sting cavity by individual transducers located outside the tunnel test section. These pressures were used in computations of the base drag corrections.

Tests

This investigation was conducted in the Langley 16-Foot Transonic Tunnel at Mach numbers from 0.60 to 0.83. The angle of attack was varied from about $-2°$ to $4°$, and the angle of sideslip was $0°$. The average Reynolds number over all test conditions was 11.88×10^6 per meter. The model was tested without any nacelles (referred to as a "clean wing configuration") and with each of the nacelle configurations installed. For all tests the horizontal-stabilizer incidence angle was set at $0°$.

Boundary-layer transition was fixed on the model using 0.25-cm-wide strips of carborundum grit. The location and size of these transition strips were selected based on the recommendations of references 15 and 16. No. 100 grit was applied 2.54 cm behind the fuselage nose and along $x/c = 0.10$ for the horizontal and vertical tails. No. 120 grit was used on the bullet tail fairing and on the nacelles. These strips were located 2.54 cm aft of the leading edge of the bullet fairing and 0.95 cm behind the inlet lip on both the inside and outside of the nacelles. Transition was fixed on the wing upper and lower surfaces, as indicated by the sketches presented in figure 15. These transition locations were selected based on the recommendations of reference 16.

Corrections to Data

Measured normal force, axial force, and pitching moment were corrected for the base pressure tares acting on the sting cavity in the aft fuselage. These corrections were determined by applying the measured base pressures to the appropriate area for each force and moment. The angle of attack of the model was corrected for sting and balance deflections and for tunnel upflow.

The drag coefficient data have also been corrected for the internal drag of the nacelles. The internal drag corrections are based on measured static pressures inside the nozzle. Internal drag is calculated using the following equation:

$$-D_i = F_i = \dot{m}\left[V_{\text{exit}} - V_\infty \cos(\alpha + i_n)\right] - (p_{\text{exit}} - p_\infty) A_{\text{exit}} \cos(\alpha + i_n) \quad (1)$$

Figure 16 shows a schematic drawing of a flow-through nacelle and provides a definition of some of the parameters used in the calculation. Equation (1) can be rewritten as

$$F_i = \dot{m}(V_{\text{inlet}} - V_\infty) - \left(\int_0^L C_p q_\infty \frac{dA_c}{dx} dx + \int_0^L c_f q \frac{dA_w}{dx} dx \right) \cos(\alpha + i_n) \quad (2)$$

Assuming that there is no loss in total pressure through the duct, the mass flow through the nacelle

can be calculated using the static pressure measured inside the nacelle at some longitudinal station well inside the duct as follows when the ratio of specific heat is 1.4:

$$M_s = \left\{5\left[(p_{t,\infty}/\bar{p}_s)^{0.2857} - 1\right]\right\}^{1/2} \quad (3)$$

$$\dot{m} = \frac{(1.4)^{1/2} p_{t,\infty} M_s A_{c,s}}{(RT_{t,\infty})^{1/2}(1 + 0.2M_s^2)^3} \quad (4)$$

Knowing the Mach number at the static pressure measurement station and the internal cross-sectional area distribution, the Mach number distribution and the C_p distribution through the duct as well as the velocity at the inlet can be determined using one-dimensional flow relationships. The skin-friction drag inside the nacelle, which is computed based on the local Mach numbers inside the duct derived from one-dimensional relations and the Von Kármán equation for local skin friction (ref. 17), is calculated using the following equations:

$$F_{i,f} = \int_0^L c_f q \frac{dA_w}{dx} dx \approx C_F \bar{q} A_{\text{wet}} \quad (5)$$

where

$$C_F = \frac{0.472}{(\log_{10} N_{\text{Re}})^{2.58}(1 + 0.2\bar{M}^2)^{0.467}} \quad (6)$$

$$\bar{M} = \frac{1}{L}\int_0^L M \, dx$$

$$\bar{q} = \frac{1}{L}\int_0^L q \, dx$$

and N_{Re} is computed based on the length of the duct and $\bar{M}$. The results of these calculations for internal drag and for flow-through mass flow ratio are presented in figures 17 and 18. For the present flow-through nacelles, the one-dimensional calculations are based on an equivalent axisymmetric nacelle with the same internal area distribution.

Presentation of Results

The effects of nacelle addition, nacelle contouring, and undernacelle fairing on the basic longitudinal aerodynamic characteristics are shown in figure 19. Figure 20 summarizes the effect of nacelle geometry on drag coefficient at $C_L = 0.45$. Effects of the various nacelle installations on the wing pressure distributions are shown in figures 21 and 22. Contour plots of the pressure distributions on the wing are presented as figures 23 and 24. The effects of streamline contouring of the nacelle and the undernacelle fairing on the nacelle pressure distributions are shown in figures 25 through 27.

Discussion

Effect of Straight Nacelle Installation

Installing the straight nacelle configuration on the basic clean wing configuration caused a small decrease in lift coefficient. (See fig. 19.) This lift decrement increased with increasing Mach number. Nacelle installation also caused an increase in pitching moment at zero lift and a decrease in longitudinal stability.

As expected, the nacelle addition also caused a significant increase in drag coefficient. For example, at $C_L = 0.45$, which corresponds to the cruise lift coefficient, the increase in drag coefficient is more than twice the computed skin-friction drag for this nacelle arrangement. (See fig. 20.) The transonic drag rise for this wing/fuselage/nacelle configuration also has more creep (premature increase in drag with Mach number before the transonic drag rise) than the basic wing-fuselage configuration. Examination of the pressure distributions on the nacelle (figs. 25 and 26) shows that the pressures on the nacelle afterbody are much lower than free stream. In fact, at $M_\infty = 0.70$ and $\phi = 90°$, there is a significant region of supersonic flow ($C_{p,\text{cr}} = -0.78$). (See fig. 25(a).) At $M_\infty = 0.80$ (where $C_{p,\text{cr}} = -0.43$), the region of supersonic flow extends completely around the nacelle (fig. 26).

At $M_\infty = 0.70$, the low pressures on the inboard side of the nacelle afterbody feed onto the upper surface of the wing and cause substantially lower pressures in the vicinity of $x/c = 0.2$. (See fig. 21 for $\eta < 0.154$.) Downstream of the nozzle exit (FS 70.721), the upper-surface wing pressures inboard of the nacelle are more positive than the clean wing configuration pressures. These pressure increases are favorable since the maximum thickness of the supercritical airfoil used for this configuration occurs near $x/c = 0.31$. The addition of the nacelle caused a shock wave to occur at about $x/c = 0.1$ at $\eta = 1.54$, which should produce some wave drag. At the fuselage centerline, these effects are small.

At $M_\infty = 0.80$ (on the inboard side of the nacelle), the addition of the nacelle caused a strong shock wave to occur at about $x/c = 0.31$. (See figs. 22 and 26.) The wave drag produced by this shock is, of course, unfavorable. However, the more negative pressures ahead of the shock wave are ahead of the wing maximum thickness location and are favorable. At this Mach number, the pressure perturbations

caused by the nacelle feed all the way to the fuselage centerline.

Very near the nacelle on the outboard wing upper surface ($\eta = 0.328$), the straight nacelle caused an increase in pressure over the entire wing chord at both $M_\infty = 0.70$ and 0.80. (See figs. 21 and 22.) The increase in pressures over the first 31 percent of the airfoil should cause an increase in drag, whereas the increase in pressures aft of 31 percent are favorable. Further outboard ($\eta = 0.370$), nacelle addition caused decreases in pressure very near the wing leading edge (a favorable effect). Aft of $x/c \approx 0.15$, however, the pressure perturbations were positive. Installing the straight nacelle increased the strength of the shock wave that is located between $x/c = 0.1$ and 0.2 that increases the drag of the configuration. At $M_\infty = 0.80$ the effects of nacelle installation on the wing upper-surface pressures extended all the way to the wingtip. At $M_\infty = 0.70$ (outboard of a semispan station of about 0.44), however, the pressure perturbations were small.

Therefore, installing the straight nacelle on the wing resulted in some favorable effects on the wing upper-surface pressures on the inboard side of the nacelle. However, the large negative pressure coefficients on the nacelle boattail and the unfavorable effects on the wing upper-surface pressures outboard of the nacelle caused the large interference drag penalties.

Effect of Nacelle Contouring

To overcome the large interference penalties associated with installing the straight upper-surface nacelle, the design approach suggested by reference 11 was implemented. According to reference 11, any disturbance of the wing flow field by the nacelle should be in a favorable direction. The nacelle must not cause isobar unsweeping but may be allowed to increase isobar sweep. Reference 11 suggests that this can be accomplished by making the nacelle invisible to the wing inboard of the nacelle by designing the nacelle inboard contour such that it follows a wing-fuselage streamsheet. Also according to reference 11, placing the nacelle contour on a streamsheet tends to prevent the occurrence of a stagnation condition at the nacelle exit.

However, if the inboard nacelle contour follows the wing-fuselage streamsheet, then it is impossible for the outer nacelle contour to follow a streamsheet because of the required thickness distribution of the nacelle. Reference 11 states that this condition is favorable in that the resulting boattail and the resulting stagnation condition at the nacelle exit on the outboard side will terminate the supersonic flow over the wing at that point and cause a shock to form in the wing flow. This wing shock will have a higher sweep than the wing-alone shock, which is desirable.

To determine the wing-fuselage streamsheet, it is necessary that a theoretical procedure be used. When the present configuration was designed, the only methods available that provided the necessary detail were panel aerodynamic codes. Therefore, the present nacelle contouring was developed using such a code and the design was done at a Mach number of 0.70 because panel codes are not capable of computing supercritical flows. At $M_\infty = 0.70$ the flow over the wing of the present wing-fuselage configuration is subcritical.

Contouring the nacelles caused a small increase in lift coefficient. (See fig. 19.) Nacelle contouring also produced a decrease in pitching moment at zero lift and a small decrease in stability.

Streamline contouring the inboard side of the nacelle also produced a reduction in drag coefficient (fig. 19) as desired. However, the contoured nacelle configuration still has a significant level of interference drag (fig. 20). The installed drag is approximately 50 percent greater than the skin-friction drag for the nacelles. The nacelle contouring also improved the drag rise characteristics of the configuration (as compared with those of the straight nacelle configuration). Examination of the pressures on the inboard side of the nacelle at $M_\infty = 0.70$ shows that nacelle streamline contouring caused a significant increase in pressure (fig. 25(a)) on the nacelle afterbody compared with the straight nacelle, indicating that the boattailing of the nacelle relative to the local flow has been reduced. Because this part of the nacelle faces forward, this positive increment is unfavorable. However, since the pressure coefficients are still significantly negative, a thrust force is being generated on the inboard side of the nacelle. At $M_\infty = 0.80$ the pressures on the inboard side of the contoured nacelle are essentially the same as those on the straight nacelle except very near the nacelle exit (fig. 26(a)). Again, these negative pressure coefficients on the forward-facing surfaces on the inboard side of the nacelle are favorable. On the outboard side of the nacelle, contouring had only a small effect on the pressures at both $M_\infty = 0.70$ and 0.80. However, because of the increased boattail angles relative to the free stream, the negative pressures probably cause greater drag on the contoured nacelle than on the straight nacelle.

Outboard of the nacelle, the installation of the contoured nacelle had essentially the same effect on the wing upper-surface pressure distributions as the installation of the straight nacelle at both $M_\infty = 0.70$ and 0.80. (See figs. 21 and 22.) Very near the nacelle on the outboard side at $\eta = 0.328$ and at

$M_\infty = 0.80$, there is evidence that the contoured nacelle produced a greater peak negative pressure coefficient at the wing leading edge than the straight nacelle configuration. (See fig. 22.) This increase in leading-edge suction on the wing would cause the drag of the contoured nacelle configuration to be lower than the drag of the straight nacelle configuration. However, the increased shock strength may counteract this favorable effect.

Inboard of the nacelle, contouring substantially increased the pressures between $x/c = 0.1$ and 0.3 at $M_\infty = 0.70$. (See fig. 21.) In fact, the pressures on the upper surface of the wing at $\eta = 0.154$ between $x/c = 0.1$ and 0.3 are very close to those of the clean wing configuration, indicating that the attempt to make the inboard side of the nacelle essentially invisible to the flow over the wing was partially successful. Ahead of $x/c = 0.1$, contouring the nacelle did not change the increased negative pressure-coefficient peak resulting from nacelle installation; that is, the negative pressure-coefficient peak for the straight and contoured nacelles was essentially the same. Downstream of $x/c = 0.30$ the pressures on the upper surface of the wing were essentially the same with or without nacelle contouring and were more positive than the clean wing configuration. These more positive pressures are in the direction to reduce the drag of the configuration.

At $M_\infty = 0.80$ on the inboard side of the nacelle, contouring the nacelle moved the shock forward and increased its strength. The shock resulting from the installation of the contoured nacelle is located at approximately 30 percent of the wing chord at $\eta = 0.154$. (See fig. 22.) Since the maximum thickness for the supercritical airfoil used for the present configuration occurs at 31 percent of the local chord, the increased negative pressure coefficients ahead of the shock wave caused by the nacelle contouring and the more positive pressures downstream of the shock are both in the direction to reduce the drag of the configuration. A comparison of the pressure distributions on the inboard side of the wing at $M_\infty = 0.80$, when the contoured nacelle is installed with the clean wing pressure distributions, shows clearly that at this Mach number, contouring the inboard side of the nacelle did not make the nacelle invisible to the flow over the wing. This result indicates that even though contouring reduced the installation drag, it is necessary that transonic theoretical methods be used to design the nacelle contour if streamline contouring is to work at transonic speeds.

From the analysis of the wing and nacelle pressure distributions, it appears, therefore, that at subcritical speeds the reductions in drag due to nacelle contouring occur primarily on the nacelle. At supercritical speeds, however, the effects of nacelle contouring on drag result primarily from changes in both the wing upper-surface pressure distributions inboard of the nacelle and the pressures on the nacelle afterbody.

Effect of Undernacelle Fairing

Adding the large fairing under the nacelle caused a very small reduction in lift coefficient and a small increase in drag coefficient. (See figs. 19 and 20.) The fairing did cause a decrease in pitching-moment coefficient at zero lift and a decrease in longitudinal stability. The pressure distributions on the wing and nacelle (figs. 21, 22, and 26) were not significantly affected by the fairing except for the lower-surface pressures very near the fairing. Therefore, such a fairing could be used to provide additional volume in the aircraft for engine support structure or instrumentation without significant performance penalties.

Conclusions

An investigation has been conducted in the Langley 16-Foot Transonic Tunnel to determine the effects of installing and streamline contouring upper-surface nacelles on the longitudinal aerodynamic characteristics of a high-wing transport configuration. Also investigated were the effects of adding a fairing under the nacelle. The investigation was conducted at free-stream Mach numbers from 0.60 to 0.83 at angles of attack from $-2°$ to $4°$. The conclusions are presented as follows:

1. Installing a straight nacelle configuration caused the drag of the configuration to increase more than twice the friction drag of the nacelles.

2. Streamline contouring the nacelle in an attempt to make the inboard side of the nacelle invisible to the wing-fuselage flow substantially reduced the interference drag. The installation drag of the contoured nacelles was about 1.5 times their friction drag.

3. At subcritical speeds, the drag reduction due to contouring occurred primarily on the nacelle boattail. At supercritical speeds, the drag reduction resulted from pressure changes on both the wing and nacelle.

4. The undernacelle fairing had essentially no effect on the drag of the configuration.

5. All three nacelle configurations caused small losses in lift coefficient, increases in pitching-moment coefficient at zero lift, and reductions in longitudinal stability.

References

1. Henderson, William P.; and Patterson, James C., Jr.: Propulsion Installation Characteristics for Turbofan Transports. AIAA-83-0087, Jan. 1983.
2. Lee, Edwin E., Jr.; and Pendergraft, Odis C., Jr.: *Installation Effects of Long-Duct Pylon-Mounted Nacelles on a Twin-Jet Transport Model With Swept Supercritical Wing.* NASA TP-2457, 1985.
3. Henderson, William P.; and Abeyounis, William K.: *Aerodynamic Characteristics of a High-Wing Transport Configuration With an Over-the-Wing Nacelle-Pylon Arrangement.* NASA TP-2497, 1985.
4. Abeyounis, William K.; and Patterson, James C., Jr.: *Effect of Underwing Aft-Mounted Nacelles on the Longitudinal Aerodynamic Characteristics of a High-Wing Transport Airplane.* NASA TP-2447, 1985.
5. Putnam, Lawrence E.; Reubush, David E.; and Lee, Edwin E., Jr.: Effects of Over-the-Wing Pylon-Mounted Engines on Transport Airplane Performance. *Proceedings of the Workshop on Engine-Airframe Integration (Short-Haul Aircraft),* S. N. B. Murthy, ed., Rep. No. PU-R1-78, Project SQUID Hdqts., Purdue Univ., May 1977, pp. 265–289.
6. Lamb, Milton; and Abeyounis, William K.: *Integration Effects of Underwing Forward- and Rearward-Mounted Separate-Flow, Flow-Through Nacelles on a High-Wing Transport.* NASA TM-87627, 1986.
7. Lamb, Milton; Abeyounis, William K.; and Patterson, James C., Jr.: *Nacelle/Pylon/Wing Integration on a Transport Model With a Natural Laminar Flow Nacelle.* NASA TP-2439, 1985.
8. Wells, O. D.; Lopez, M. L.; Welge, H. R.; Henne, P. A.; and Sewell, A. E.: *Wind Tunnel and Analytical Investigation of Over-the-Wing Propulsion/Airframe Interferences for a Short-Haul Aircraft at Mach Numbers From 0.6 to 0.78.* NASA CR-2905, 1977.
9. Braden, J. A.; Hancock, J. P.; Hackett, J. E.; Burdges, K. P.; and Lyman, V.: *Exploratory Studies of the Cruise Performance of Upper Surface Blown Configurations. Summary Report.* NASA CR-3193, 1980.
10. Riddle, D. W.; Innis, R. C.; Martin, J. L.; and Cochrane, J. A.: Powered-Lift Takeoff Performance Characteristics Determined From Flight Test of the Quiet Short-Haul Research Aircraft (QSRA). AIAA-81-2409, Nov. 1981.
11. Gillette, W. B.; Mohn, L. W.; Ridley, H. G.; and Nark, T. C.: *Upper-Surface Blowing Nacelle Design Study for a Swept Wing Airplane at Cruise Conditions.* NASA CR-2427, 1974.
12. Gillette, W. B.: Nacelle Installation Analysis for Subsonic Transport Aircraft. AIAA Paper 77-102, Jan. 1977.
13. Corson, Blake W., Jr.; Runckel, Jack F.; and Igoe, William B.: *Calibration of the Langley 16-Foot Transonic Tunnel With Test Section Air Removal.* NASA TR R-423, 1974.
14. Peddrew, Kathryn H., compiler: *A User's Guide to the Langley 16-Foot Transonic Tunnel.* NASA TM-83186, 1981.
15. Braslow, Albert L.; Hicks, Raymond M.; and Harris, Roy V., Jr.: *Use of Grit-Type Boundary-Layer-Transition Trips on Wind-Tunnel Models.* NASA TN D-3579, 1966.
16. Blackwell, James A., Jr.: *Preliminary Study of Effects of Reynolds Number and Boundary-Layer Transition Location on Shock-Induced Separation.* NASA TN D-5003, 1969.
17. Shapiro, Ascher H.: *The Dynamics and Thermodynamics of Compressible Fluid Flow. Volume II.* Ronald Press Co., c.1954.

TABLE I. WING STREAMWISE AIRFOIL COORDINATES

(a) $\eta = 0.127$ (fuselage side)

x/c	z/c	
	Upper surface	Lower surface
0	-.0016	-.0016
.002	.0104	-.0136
.005	.0164	-.0196
.010	.0229	-.0266
.020	.0304	-.0351
.030	.0359	-.0401
.040	.0394	-.0446
.050	.0419	-.0486
.060	.0441	-.0521
.070	.0460	-.0553
.080	.0477	-.0581
.090	.0492	-.0607
.100	.0506	-.0632
.110	.0518	-.0655
.120	.0529	-.0676
.130	.0539	-.0695
.140	.0548	-.0713
.150	.0556	-.0730
.160	.0563	-.0746
.170	.0570	-.0760
.180	.0576	-.0773
.190	.0582	-.0785
.200	.0587	-.0796
.210	.0591	-.0805
.220	.0593	-.0813
.230	.0595	-.0820
.240	.0596	-.0826
.250	.0596	-.0832
.260	.0596	-.0837
.270	.0595	-.0842
.280	.0593	-.0846
.290	.0591	-.0850
.300	.0588	-.0853
.310	.0585	-.0856
.320	.0581	-.0858
.330	.0577	-.0860
.340	.0572	-.0862
.350	.0567	-.0863

x/c	z/c	
	Upper surface	Lower surface
.360	.0561	-.0864
.370	.0555	-.0864
.380	.0548	-.0863
.390	.0541	-.0862
.400	.0534	-.0860
.410	.0526	-.0858
.420	.0518	-.0855
.430	.0510	-.0852
.440	.0501	-.0848
.450	.0492	-.0843
.460	.0483	-.0838
.470	.0473	-.0832
.480	.0463	-.0825
.490	.0453	-.0817
.500	.0442	-.0809
.510	.0431	-.0800
.520	.0420	-.0790
.530	.0408	-.0779
.540	.0396	-.0767
.550	.0384	-.0754
.560	.0371	-.0741
.570	.0358	-.0727
.580	.0345	-.0713
.590	.0331	-.0698
.600	.0317	-.0683
.610	.0303	-.0668
.620	.0289	-.0652
.630	.0274	-.0636
.640	.0259	-.0620
.650	.0244	-.0604
.660	.0229	-.0588
.670	.0213	-.0573
.680	.0197	-.0558
.690	.0181	-.0543
.700	.0164	-.0529
.710	.0147	-.0515
.720	.0130	-.0502
.730	.0113	-.0489

TABLE I. Continued

(a) Concluded

x/c	z/c	
	Upper surface	Lower surface
.740	.0095	-.0477
.750	.0077	-.0465
.760	.0059	-.0454
.770	.0041	-.0444
.780	.0022	-.0434
.790	.0003	-.0425
.800	-.0016	-.0417
.810	-.0036	-.0410
.820	-.0056	-.0404
.830	-.0076	-.0399
.840	-.0096	-.0394
.850	-.0116	-.0390
.860	-.0136	-.0387
.870	-.0156	-.0385
.880	-.0176	-.0384
.890	-.0196	-.0385
.900	-.0216	-.0387
.910	-.0236	-.0390
.920	-.0256	-.0394
.930	-.0276	-.0400
.940	-.0296	-.0407
.950	-.0316	-.0415
.960	-.0336	-.0424
.970	-.0356	-.0435
.980	-.0376	-.0447
.990	-.0396	-.0460
1.000	-.0416	-.0476
$c = 37.899$ cm $\varepsilon = 2.462°$ $t/c = .144$		

TABLE I. Continued

(b) $\eta = 0.410$ (planform break)

x/c	z/c	
	Upper surface	Lower surface
0	-.0044	-.0044
.002	.0049	-.0131
.005	.0099	-.0181
.010	.0148	-.0230
.020	.0210	-.0290
.030	.0253	-.0329
.040	.0286	-.0360
.050	.0312	-.0386
.060	.0336	-.0408
.070	.0357	-.0427
.080	.0376	-.0444
.090	.0393	-.0459
.100	.0409	-.0473
.110	.0424	-.0487
.120	.0436	-.0499
.130	.0448	-.0510
.140	.0460	-.0520
.150	.0471	-.0529
.160	.0481	-.0538
.170	.0491	-.0546
.180	.0500	-.0554
.190	.0508	-.0561
.200	.0516	-.0567
.210	.0523	-.0573
.220	.0530	-.0579
.230	.0537	-.0584
.240	.0543	-.0588
.250	.0548	-.0593
.260	.0554	-.0597
.270	.0559	-.0600
.280	.0563	-.0603
.290	.0568	-.0605
.300	.0571	-.0607
.310	.0575	-.0609
.320	.0577	-.0611
.330	.0580	-.0612
.340	.0582	-.0612
.350	.0585	-.0612

x/c	z/c	
	Upper surface	Lower surface
.360	.0587	-.0611
.370	.0589	-.0610
.380	.0590	-.0609
.390	.0590	-.0608
.400	.0591	-.0606
.410	.0591	-.0603
.420	.0591	-.0601
.430	.0591	-.0597
.440	.0591	-.0593
.450	.0590	-.0589
.460	.0588	-.0584
.470	.0587	-.0578
.480	.0585	-.0572
.490	.0584	-.0562
.500	.0582	-.0558
.510	.0579	-.0549
.520	.0577	-.0541
.530	.0573	-.0531
.540	.0570	-.0520
.550	.0567	-.0508
.560	.0563	-.0496
.570	.0559	-.0482
.580	.0555	-.0468
.590	.0550	-.0454
.600	.0544	-.0438
.610	.0539	-.0422
.620	.0534	-.0405
.630	.0528	-.0387
.640	.0522	-.0369
.650	.0515	-.0351
.660	.0509	-.0332
.670	.0500	-.0314
.680	.0493	-.0294
.690	.0485	-.0275
.700	.0476	-.0255
.710	.0467	-.0235
.720	.0458	-.0215
.730	.0448	-.0195

TABLE I. Continued

(b) Concluded

x/c	z/c	
	Upper surface	Lower surface
.740	.0438	-.0175
.750	.0427	-.0155
.760	.0415	-.0135
.770	.0404	-.0116
.780	.0391	-.0098
.790	.0378	-.0081
.800	.0365	-.0064
.810	.0351	-.0048
.820	.0336	-.0034
.830	.0320	-.0020
.840	.0304	-.0008
.850	.0288	.0003
.860	.0271	.0011
.870	.0253	.0017
.880	.0235	.0021
.890	.0215	.0024
.900	.0195	.0025
.910	.0174	.0023
.920	.0152	.0019
.930	.0130	.0011
.940	.0107	.0001
.950	.0083	-.0012
.960	.0058	-.0027
.970	.0033	-.0046
.980	.0005	-.0067
.990	-.0025	-.0092
1.000	-.0056	-.0120
$c = 23.249$ cm $\varepsilon = 0.256°$ $t/c = .12$		

TABLE I. Continued

(c) $\eta = 1.000$ (tip)

x/c	z/c	
	Upper surface	Lower surface
0	-.0175	-.0175
.002	-.0095	-.0240
.005	-.0053	-.0284
.010	-.0012	-.0323
.020	.0041	-.0367
.030	.0079	-.0397
.040	.0109	-.0420
.050	.0134	-.0439
.060	.0157	-.0455
.070	.0177	-.0468
.080	.0195	-.0480
.090	.0213	-.0491
.100	.0229	-.0500
.110	.0245	-.0509
.120	.0258	-.0516
.130	.0272	-.0523
.140	.0284	-.0530
.150	.0296	-.0535
.160	.0308	-.0540
.170	.0318	-.0544
.180	.0329	-.0548
.190	.0339	-.0551
.200	.0349	-.0554
.210	.0357	-.0557
.220	.0366	-.0559
.230	.0374	-.0561
.240	.0382	-.0562
.250	.0390	-.0563
.260	.0397	-.0563
.270	.0404	-.0564
.280	.0410	-.0564
.290	.0417	-.0563
.300	.0422	-.0563
.310	.0428	-.0561
.320	.0433	-.0560
.330	.0437	-.0558
.340	.0442	-.0556
.350	.0446	-.0553

x/c	z/c	
	Upper surface	Lower surface
.360	.0451	-.0551
.370	.0455	-.0548
.380	.0459	-.0544
.390	.0462	-.0541
.400	.0465	-.0536
.410	.0468	-.0532
.420	.0470	-.0527
.430	.0473	-.0522
.440	.0475	-.0516
.450	.0478	-.0510
.460	.0479	-.0503
.470	.0481	-.0495
.480	.0482	-.0488
.490	.0483	-.0479
.500	.0484	-.0471
.510	.0484	-.0462
.520	.0485	-.0451
.530	.0485	-.0441
.540	.0486	-.0429
.550	.0485	-.0418
.560	.0485	-.0405
.570	.0484	-.0392
.580	.0484	-.0378
.590	.0482	-.0364
.600	.0481	-.0348
.610	.0479	-.0333
.620	.0477	-.0316
.630	.0475	-.0299
.640	.0472	-.0281
.650	.0470	-.0264
.660	.0467	-.0245
.670	.0464	-.0227
.680	.0460	-.0208
.690	.0457	-.0189
.700	.0452	-.0170
.710	.0448	-.0150
.720	.0443	-.0131
.730	.0437	-.0111

TABLE I. Concluded

(c) Concluded

x/c	z/c	
	Upper surface	Lower surface
.740	.0432	-.0092
.750	.0426	-.0072
.760	.0420	-.0052
.770	.0413	-.0034
.780	.0406	-.0015
.790	.0398	.0003
.800	.0391	.0020
.810	.0382	.0037
.820	.0372	.0052
.830	.0362	.0067
.840	.0351	.0081
.850	.0340	.0094
.860	.0328	.0104
.870	.0316	.0113
.880	.0302	.0119
.890	.0288	.0123
.900	.0273	.0127
.910	.0258	.0127
.920	.0241	.0126
.930	.0224	.0122
.940	.0207	.0114
.950	.0188	.0104
.960	.0168	.0091
.970	.0146	.0076
.980	.0123	.0057
.990	.0097	.0036
1.000	.0069	.0012

$c = 10.521$ cm

$\varepsilon = -1.229°$

$t/c = .10$

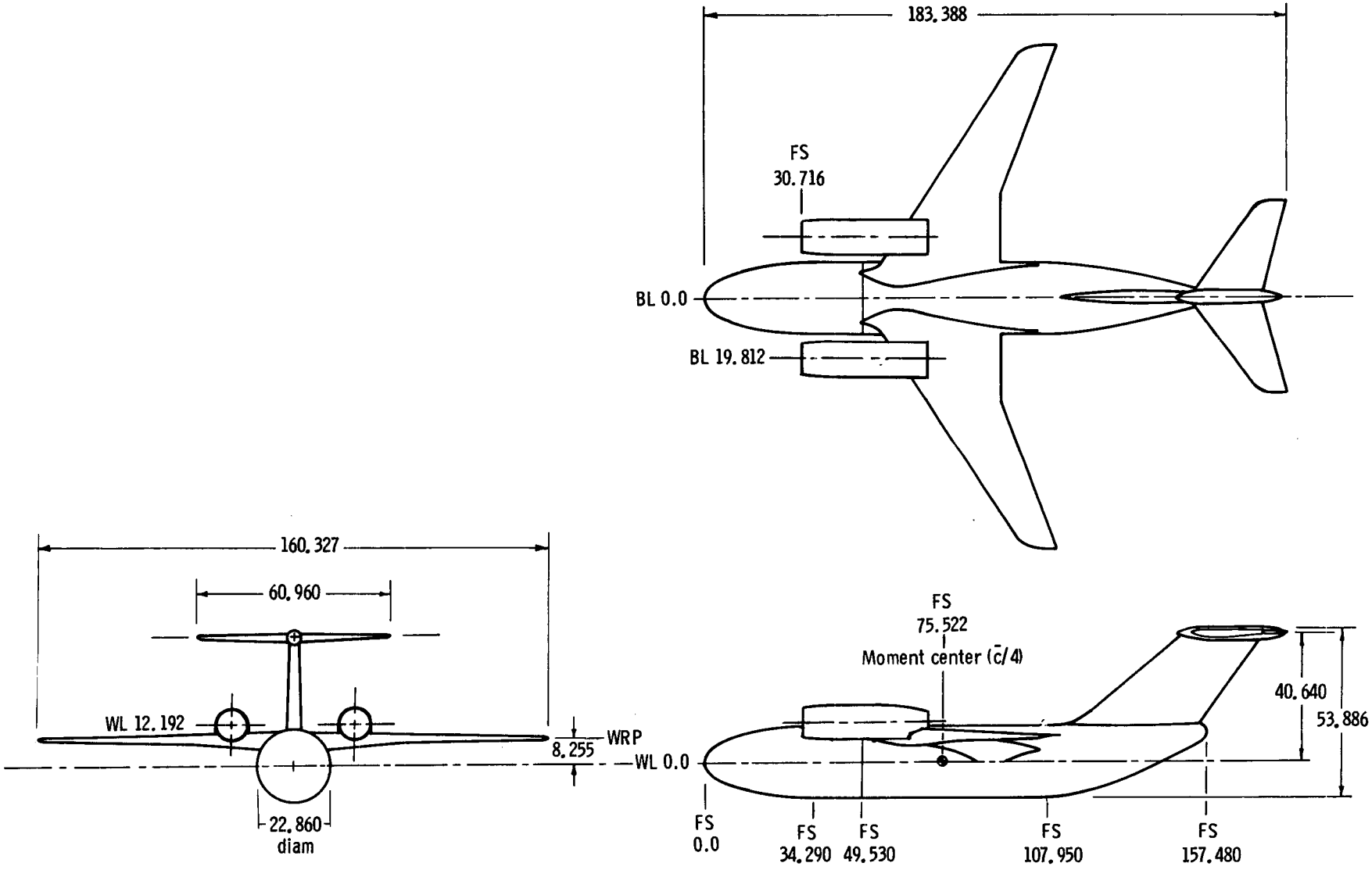

Figure 1. Sketch of basic transport model with straight nacelle. Linear dimensions are in centimeters.

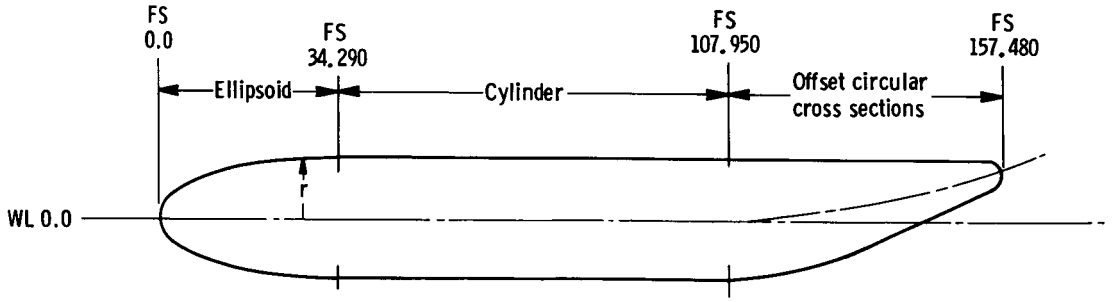

Closure detail

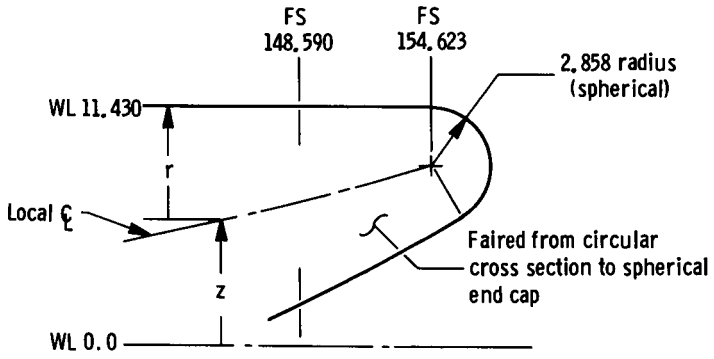

Ellipsoidal nose coordinates	
FS	r
0	0
.254	1.389
.508	1.961
.635	2.189
.952	2.675
1.270	3.081
1.905	3.757
2.540	4.318
3.175	4.803
3.810	5.237
5.080	5.987
6.350	6.627
8.890	7.678
11.430	8.519
13.970	9.208
16.510	9.774
19.050	10.239
24.130	10.917
29.210	11.303
34.290	11.430

Afterbody coordinates		
FS	z	r
107.950	0	11.430
113.030	.254	11.176
118.110	.711	10.719
123.190	1.397	10.033
128.270	2.184	9.246
133.350	3.112	8.319
138.430	4.216	7.214
143.510	5.410	6.020
148.590	6.731	4.699
154.622	8.573	2.858

(a) Basic shape.

Figure 2. Sketch showing details of fuselage geometry. All dimensions are in centimeters.

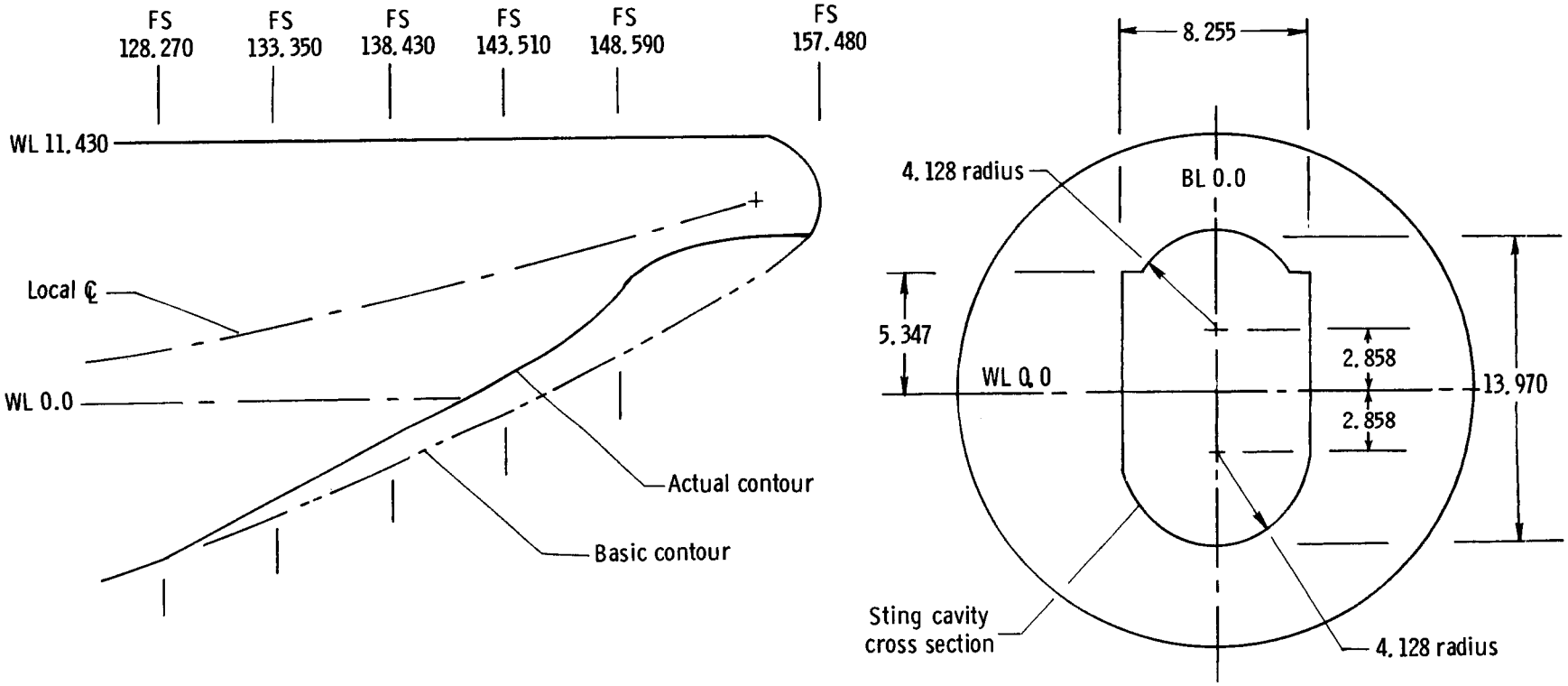

(b) Fuselage closure with sting cavity.

Figure 2. Concluded.

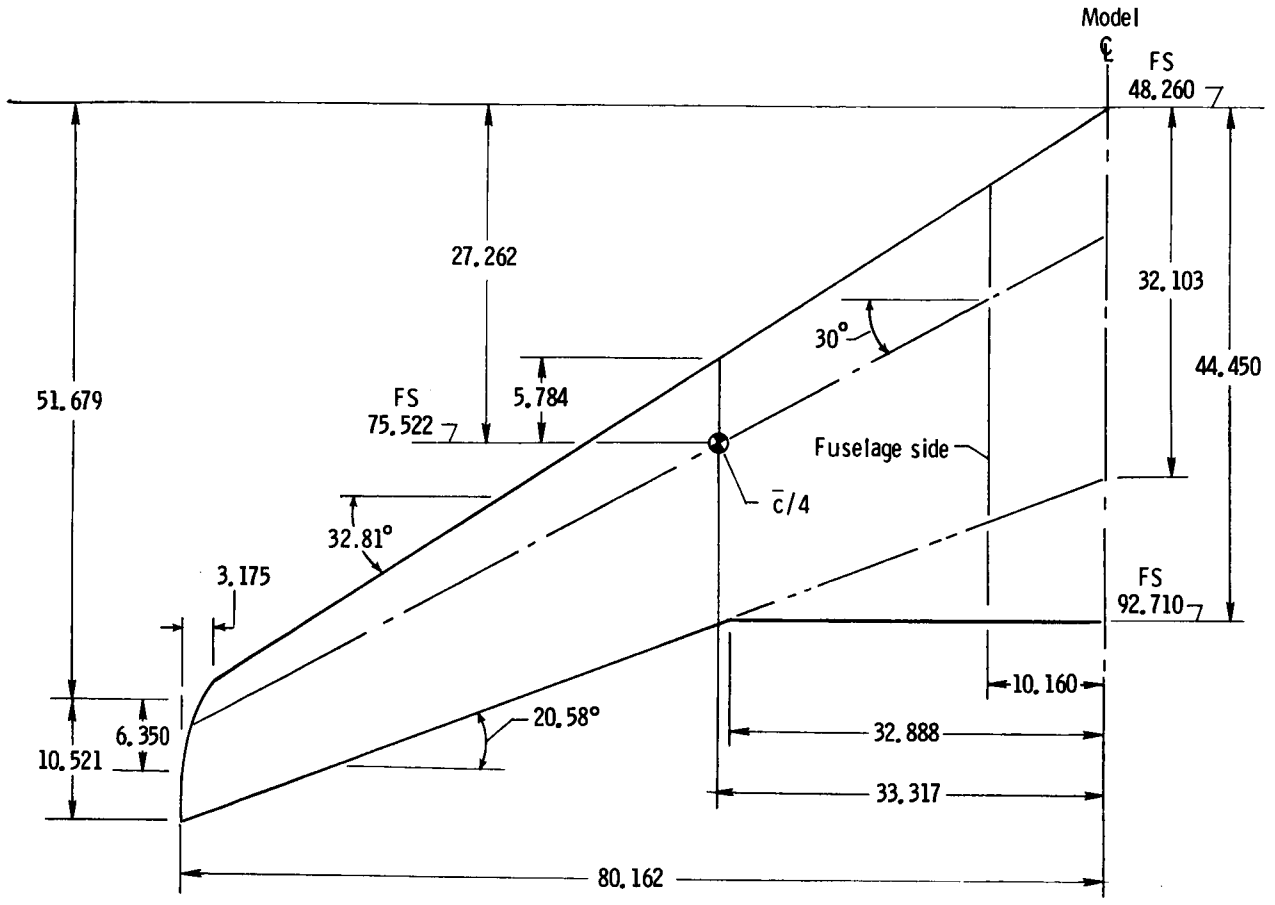

Aspect ratio	7.52
Taper ratio	0.328
Area (trapezoid), cm^2	3416.66
$\bar{c}$, cm	23.132
c_{av}, cm	21.311
Incidence, deg.....	0
Dihedral, deg.....	0

Figure 3. Sketch showing wing planform details. All dimensions are in centimeters unless otherwise noted.

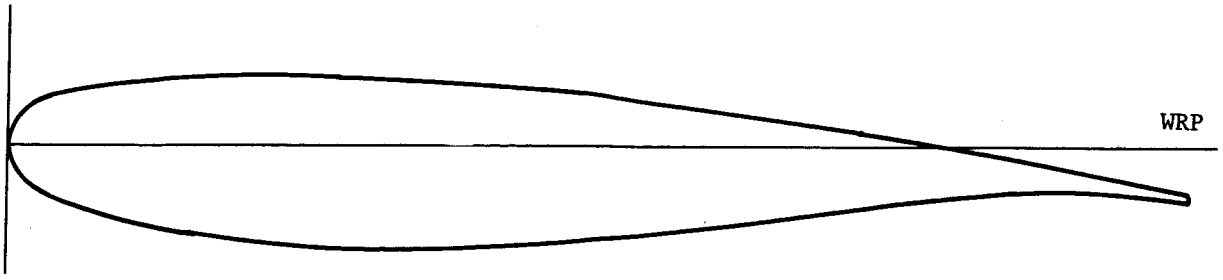

(a) Fuselage side. $t/c = 0.144$; BL 10.160.

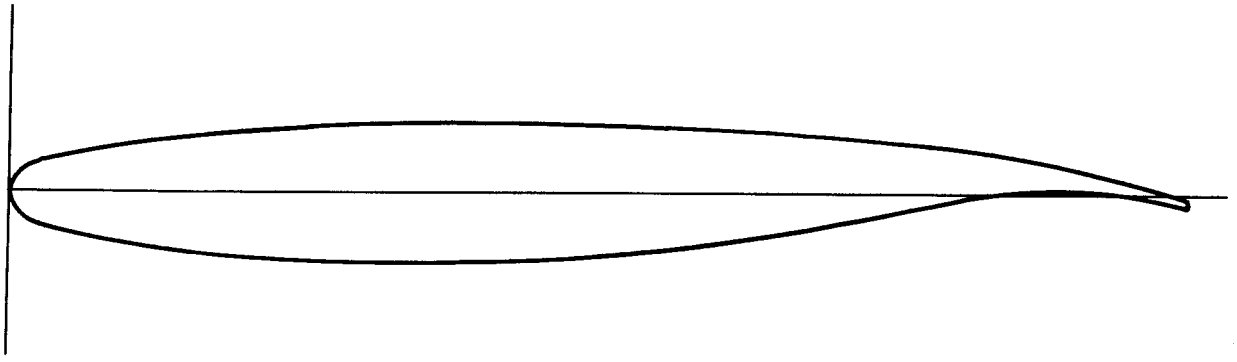

(b) Planform break. $t/c = 0.12$; BL 32.888.

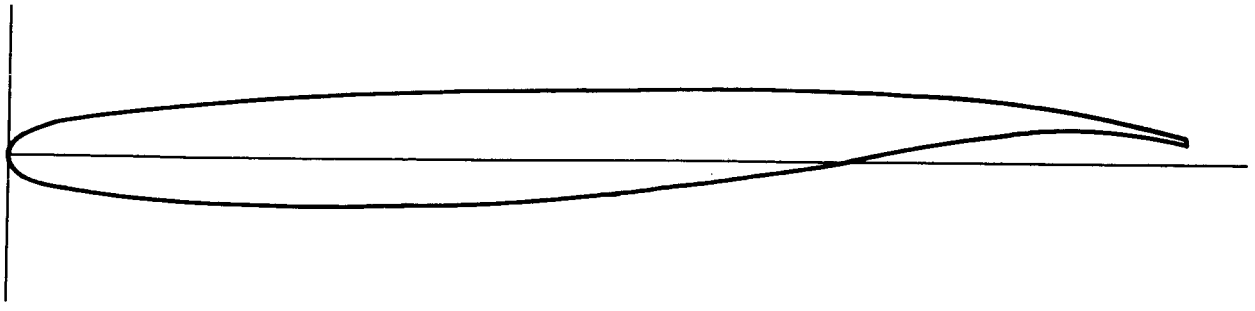

(c) Tip. $t/c = 0.10$; BL 80.162.

Figure 4. Defining airfoil sections of model wing. All dimensions are in centimeters unless otherwise noted.

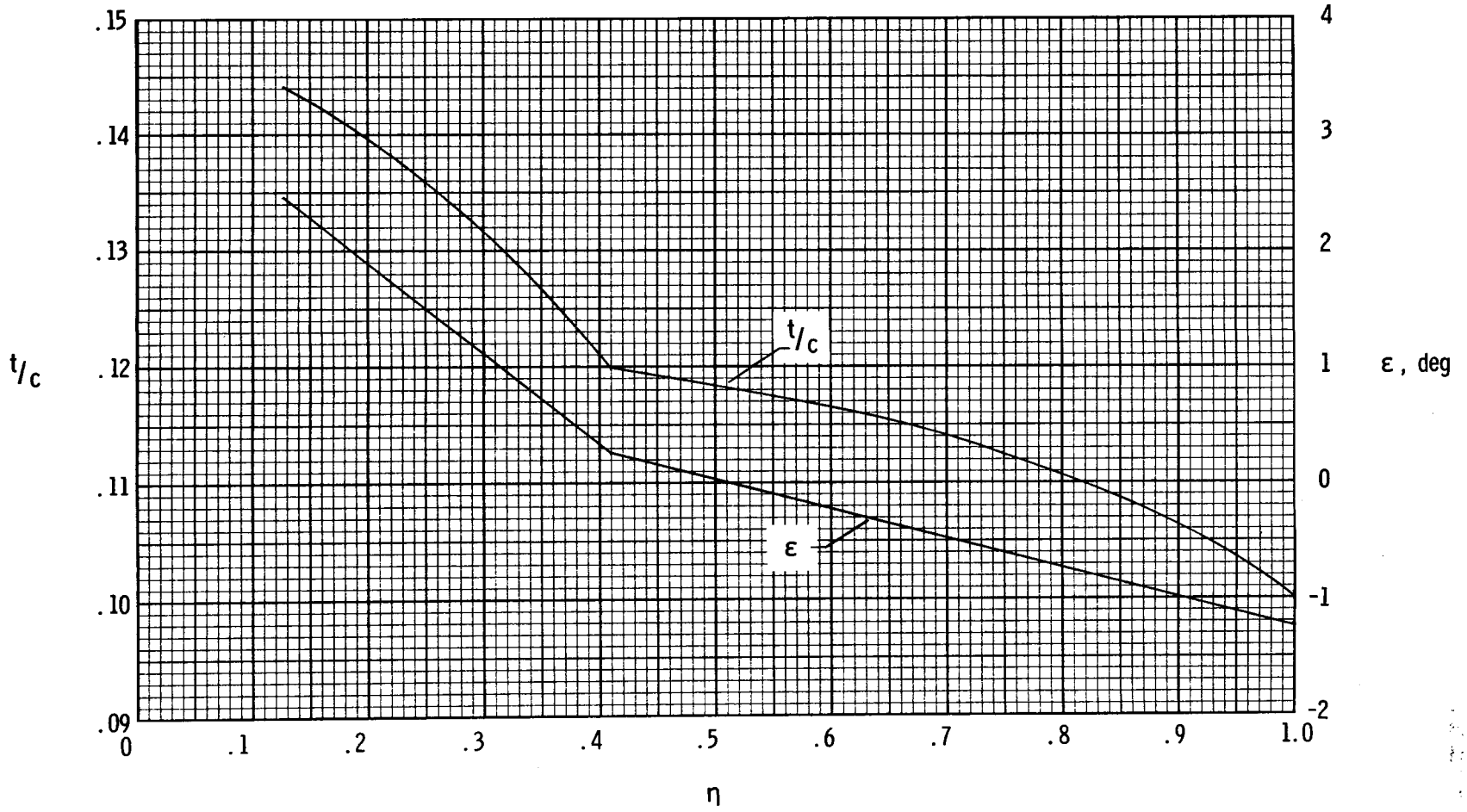

Figure 5. Spanwise thickness and twist distributions of wing.

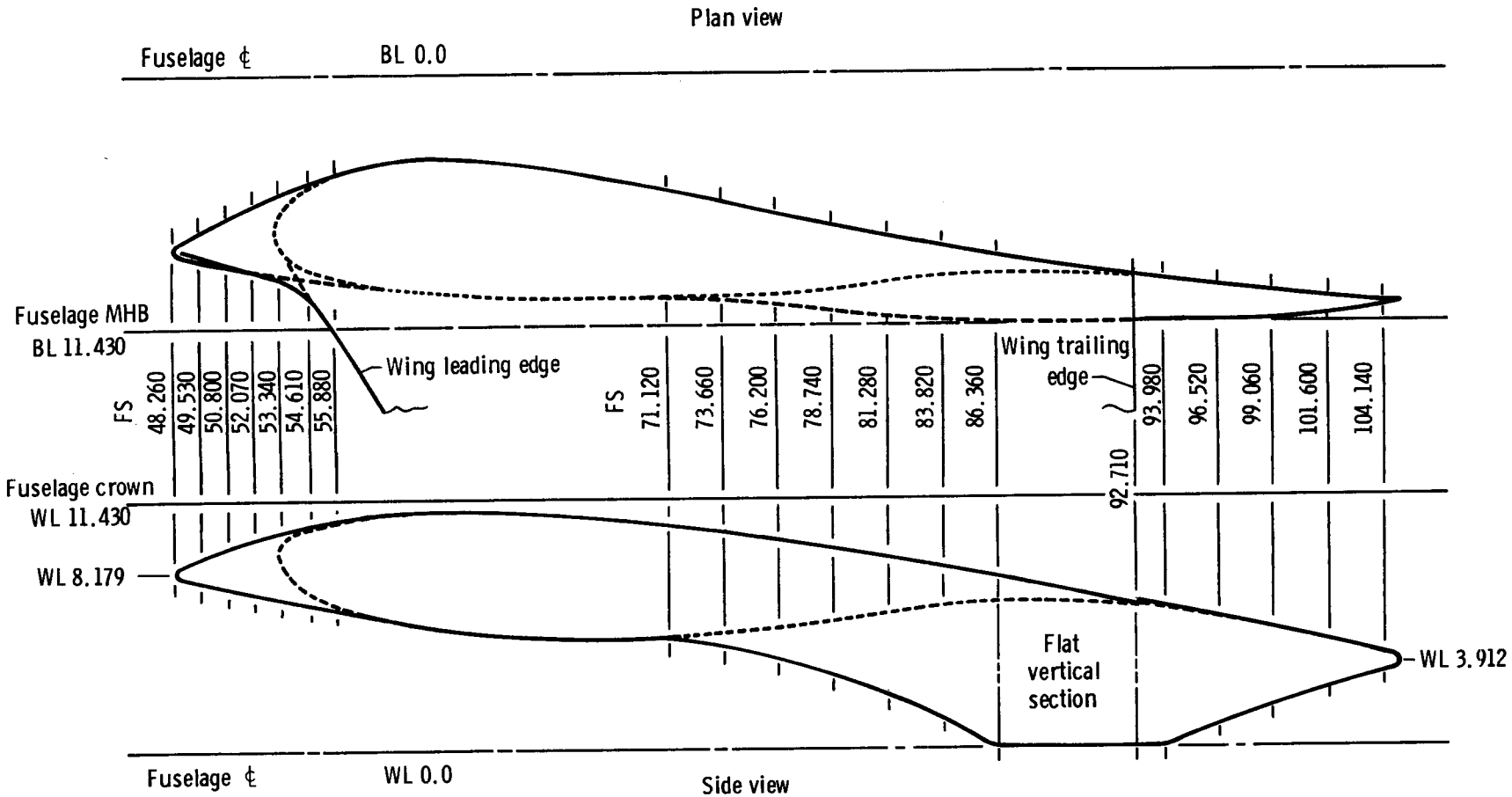

(a) Top and side profiles.

Figure 6. Details of wing-fuselage fairing. All dimensions are in centimeters.

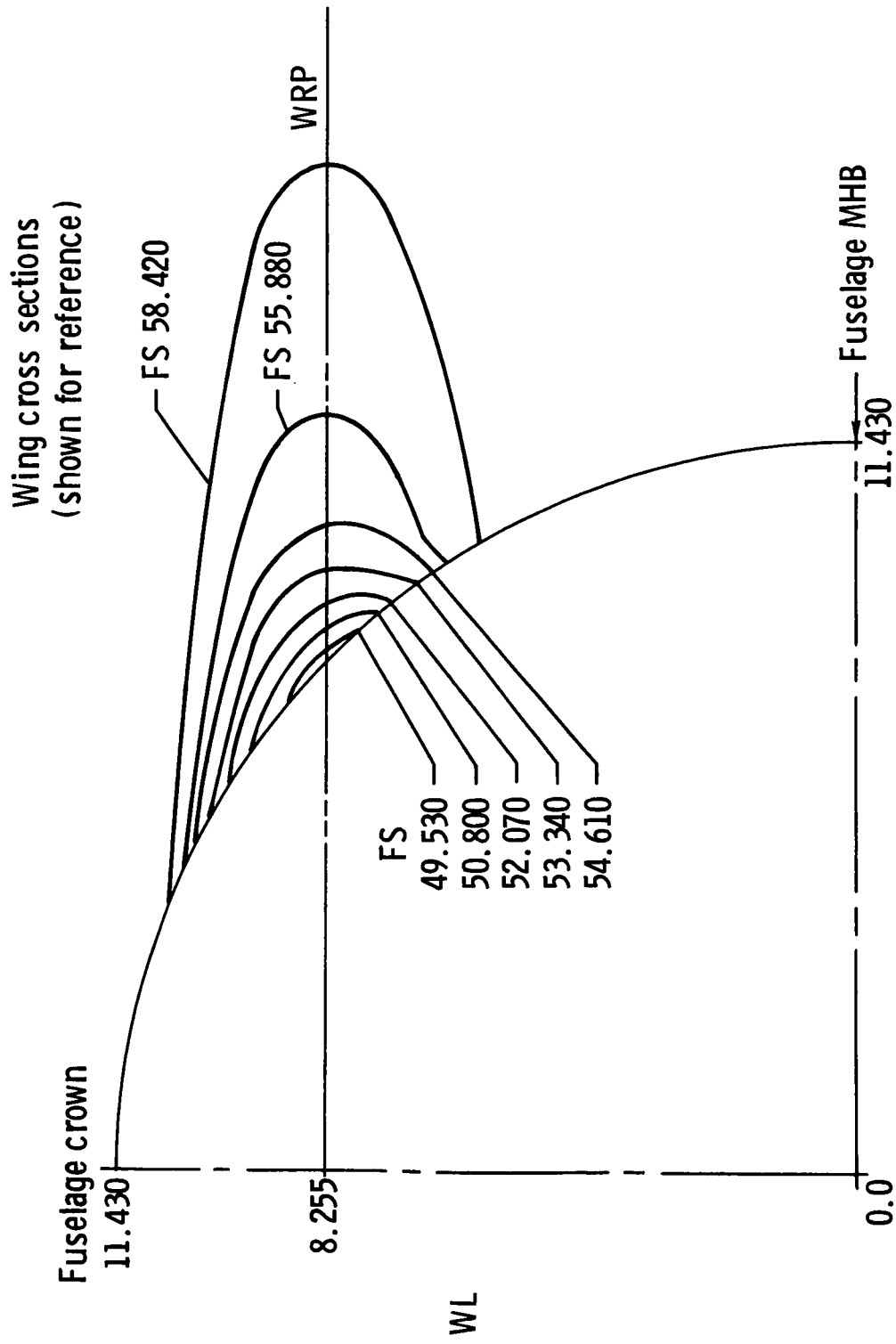

(b) Forward fairing cross sections.

Figure 6. Continued.

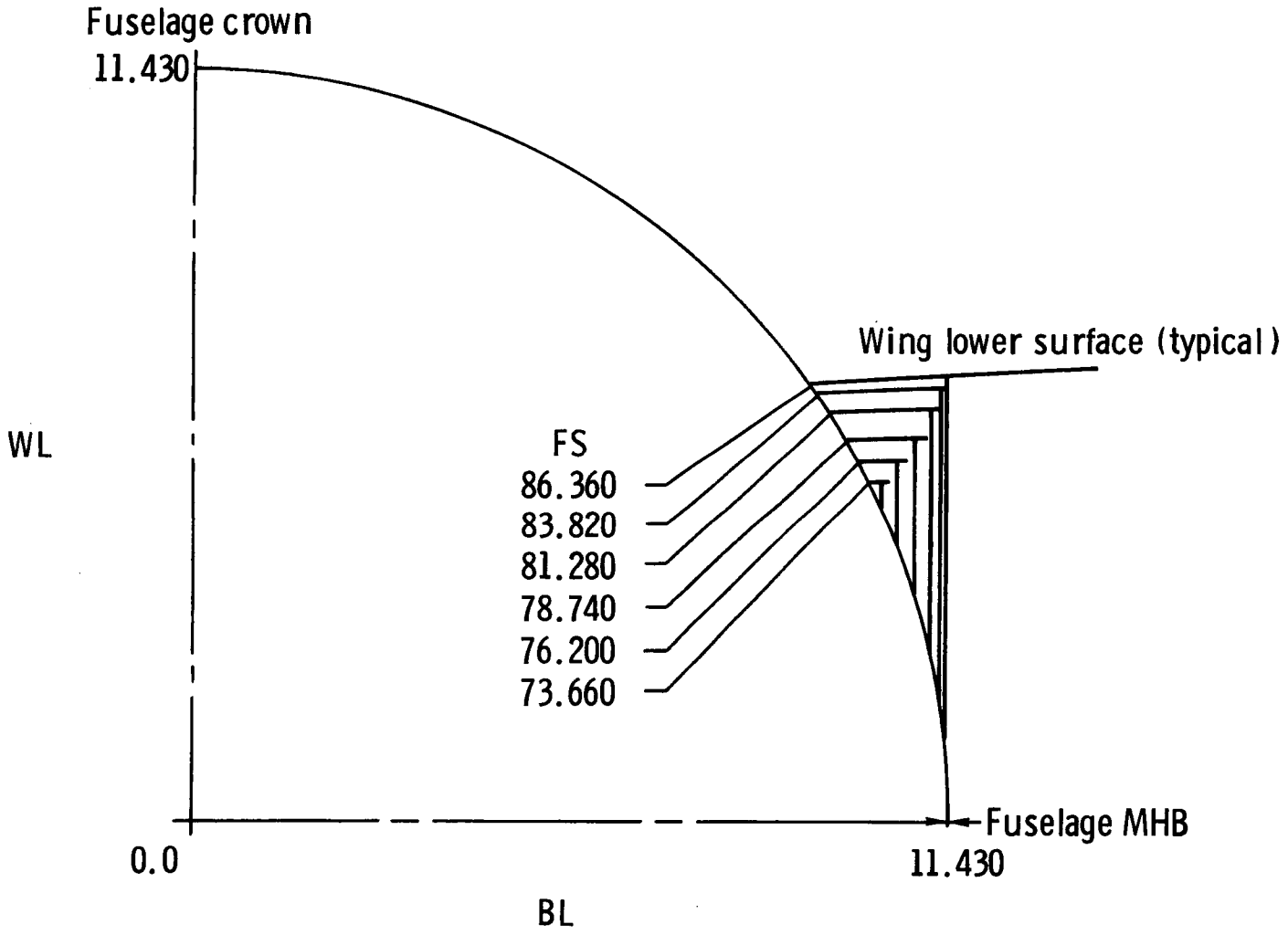

(c) Rear fairing cross sections. Wing lower surface.

Figure 6. Continued.

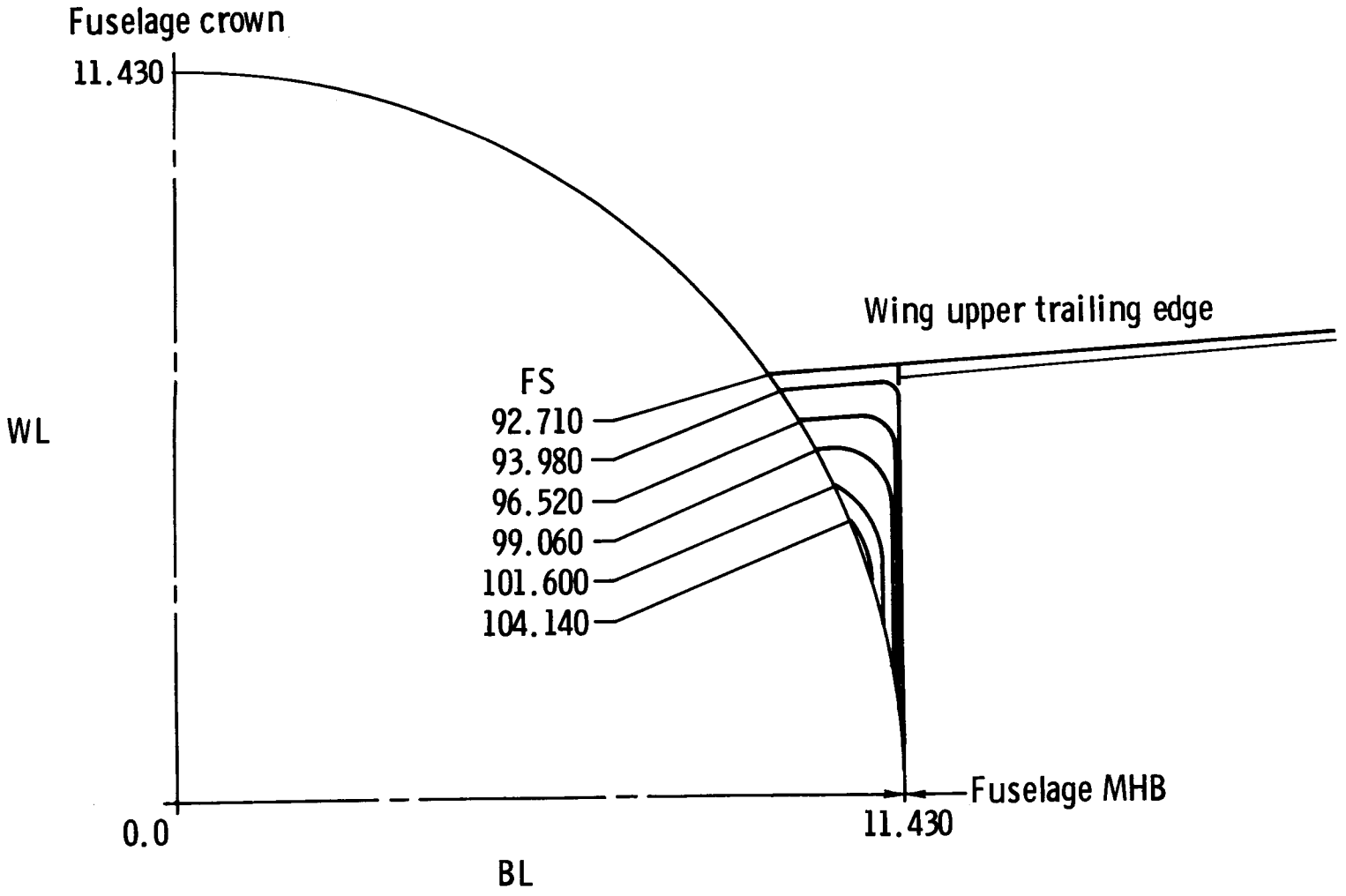

(d) Rear fairing cross sections. Wing upper trailing edge.

Figure 6. Concluded.

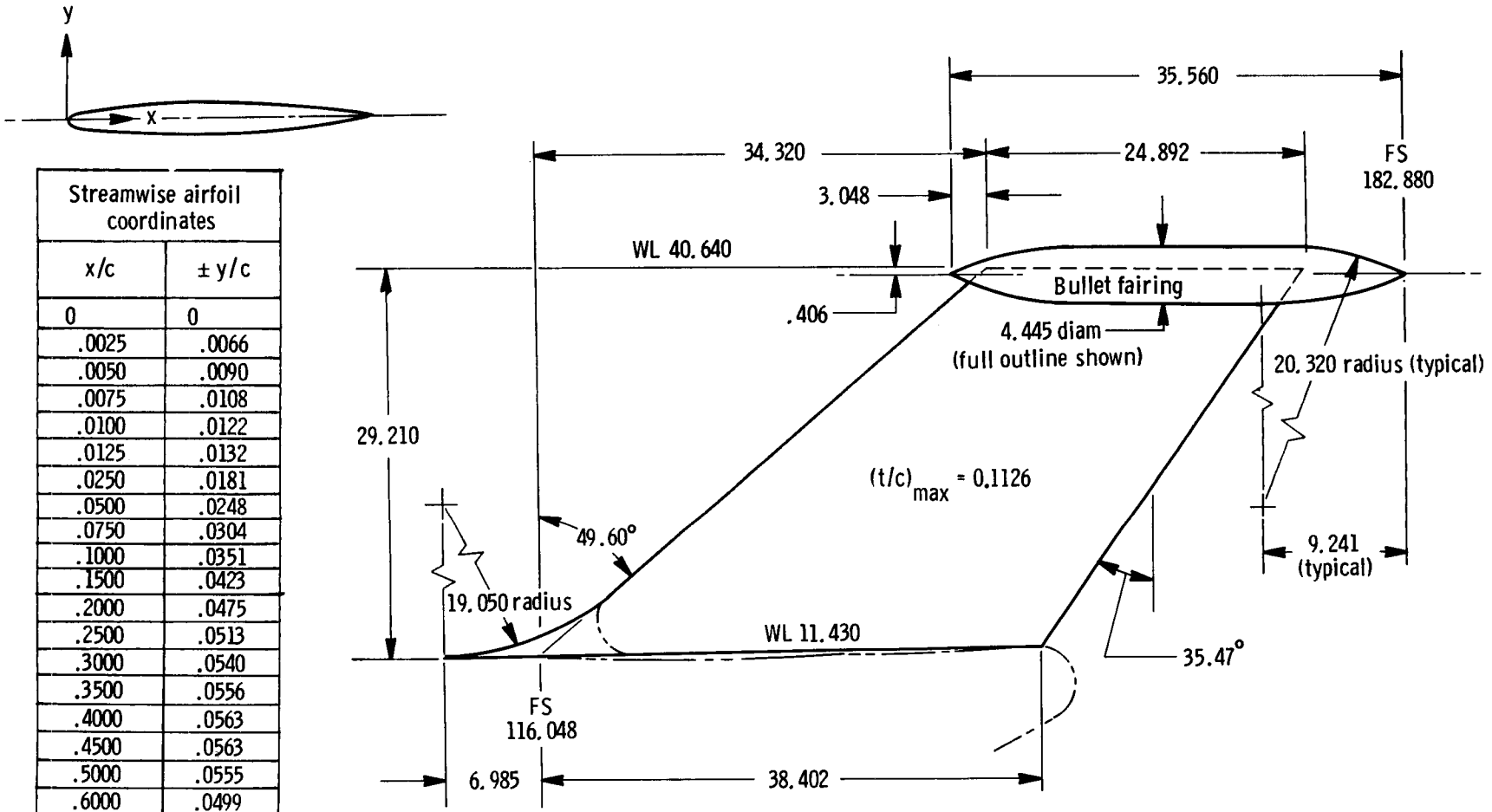

Streamwise airfoil coordinates	
x/c	± y/c
0	0
.0025	.0066
.0050	.0090
.0075	.0108
.0100	.0122
.0125	.0132
.0250	.0181
.0500	.0248
.0750	.0304
.1000	.0351
.1500	.0423
.2000	.0475
.2500	.0513
.3000	.0540
.3500	.0556
.4000	.0563
.4500	.0563
.5000	.0555
.6000	.0499
.7000	.0394
.7500	.0328
1.0000	.0004

LER/c = 0.0100

Figure 7. Sketch showing details of vertical tail. All dimensions are in centimeters unless otherwise noted.

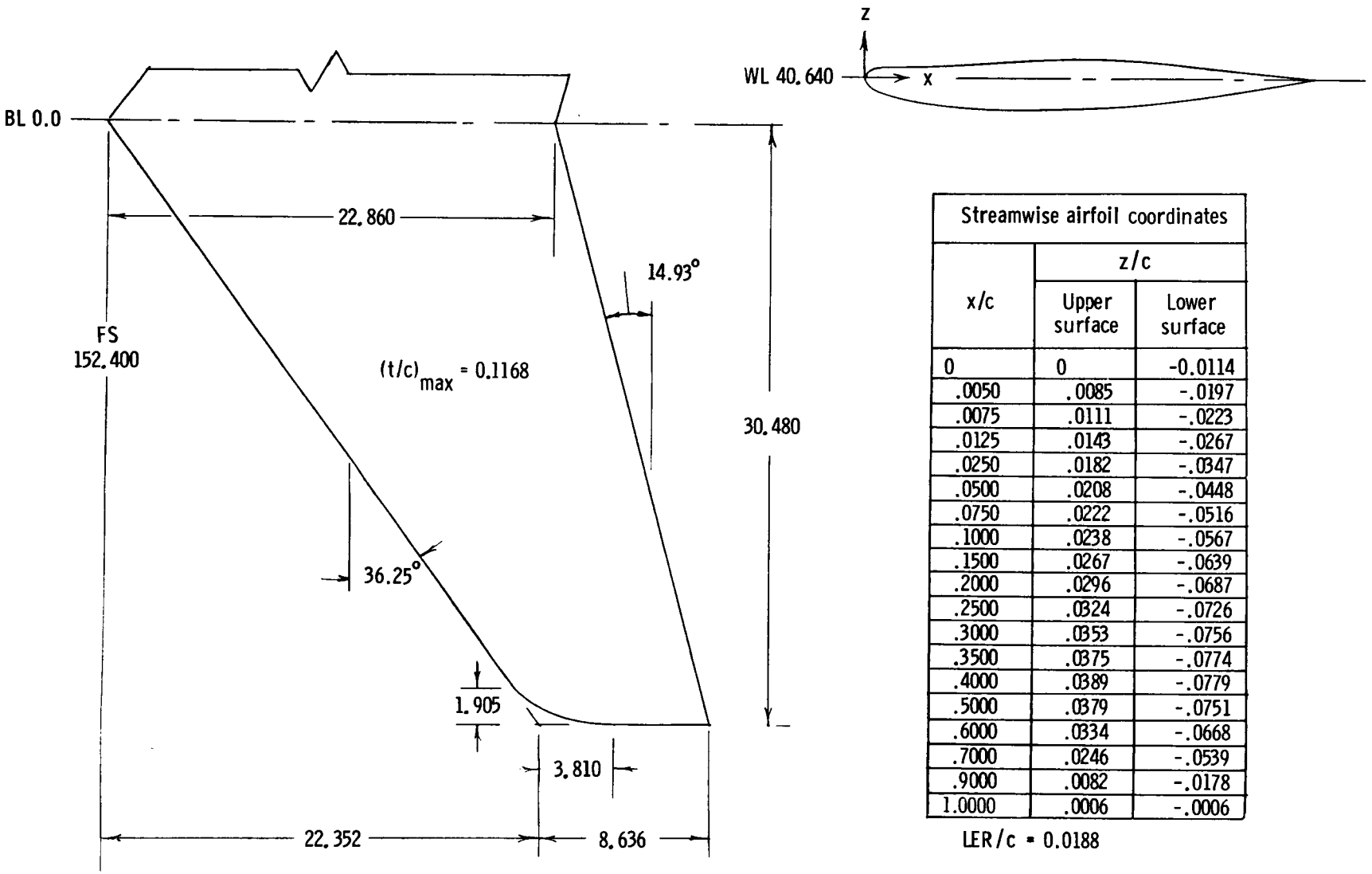

Streamwise airfoil coordinates		
x/c	z/c	
	Upper surface	Lower surface
0	0	-0.0114
.0050	.0085	-.0197
.0075	.0111	-.0223
.0125	.0143	-.0267
.0250	.0182	-.0347
.0500	.0208	-.0448
.0750	.0222	-.0516
.1000	.0238	-.0567
.1500	.0267	-.0639
.2000	.0296	-.0687
.2500	.0324	-.0726
.3000	.0353	-.0756
.3500	.0375	-.0774
.4000	.0389	-.0779
.5000	.0379	-.0751
.6000	.0334	-.0668
.7000	.0246	-.0539
.9000	.0082	-.0178
1.0000	.0006	-.0006

LER/c = 0.0188

Figure 8. Sketch showing details of horizontal tail. All dimensions are in centimeters unless otherwise noted.

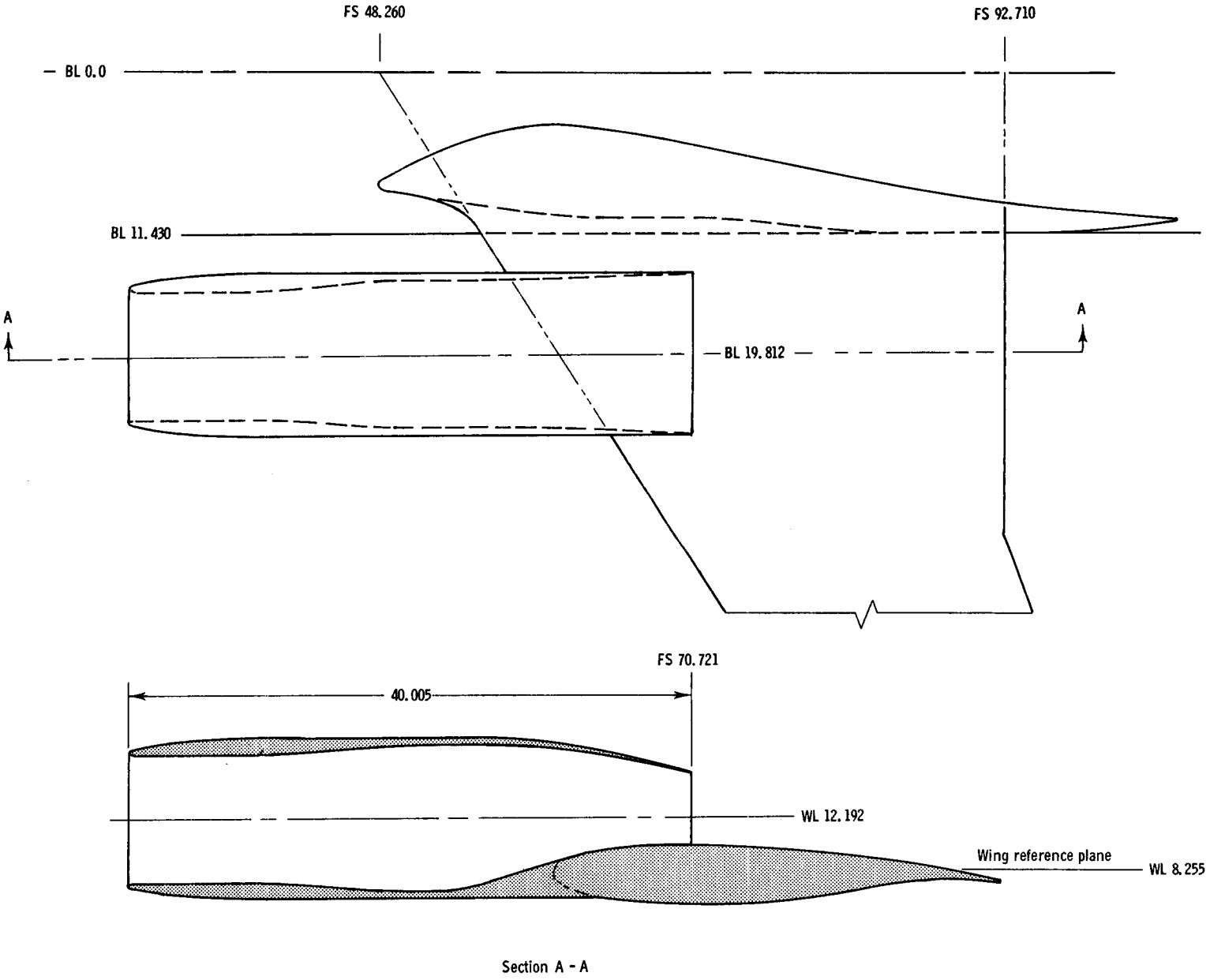

Figure 9. Sketch showing installation of straight upper-surface nacelle configuration (USBC) on wing. All dimensions are in centimeters unless otherwise noted.

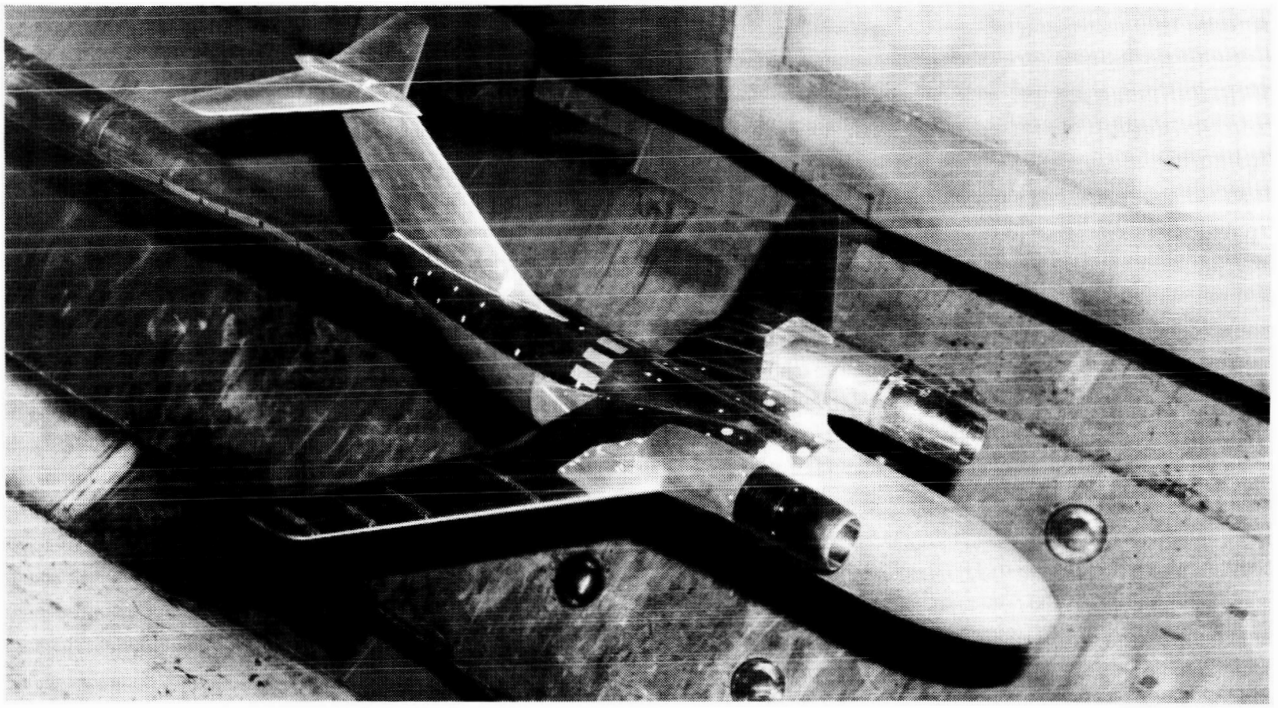

L-79-4204

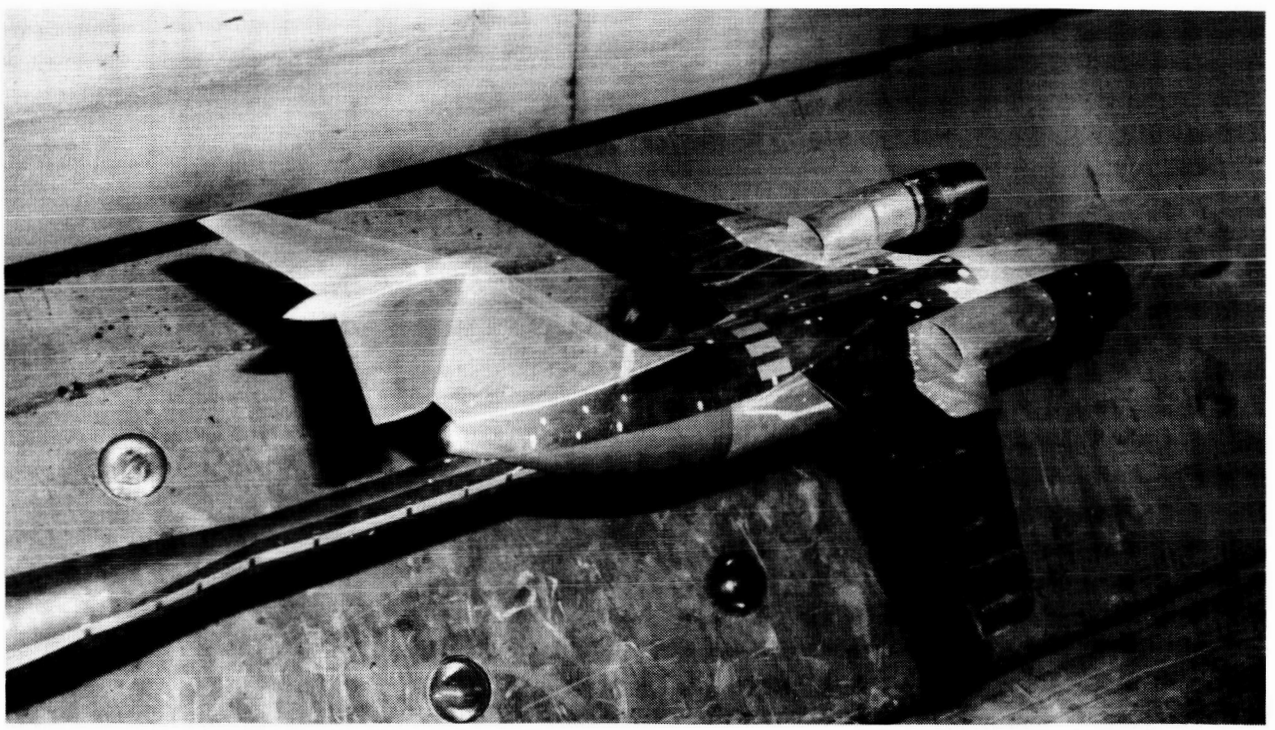

L-79-4205

Figure 10. Photographs of model with straight nacelle mounted in the Langley 16-Foot Transonic Tunnel.

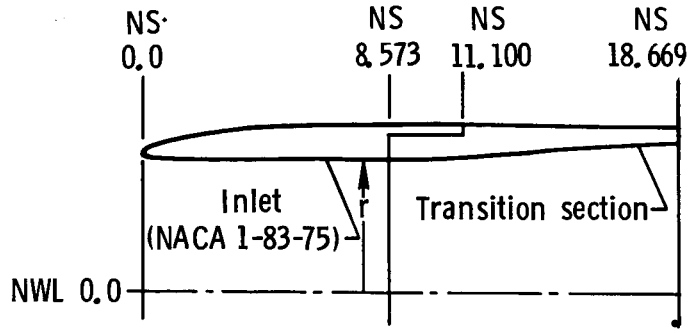

Inlet coordinates			
External		Internal	
NS	r	NS	r
0	4.760	0	4.760
.018	4.806	.018	4.699
.036	4.823	.036	4.676
.051	4.836	.051	4.658
.086	4.859	.086	4.633
.130	4.882	.130	4.608
.173	4.900	.173	4.592
.214	4.917	.214	4.577
.257	4.935	.257	4.569
.343	4.966	.373	4.559
.429	4.994	8.572	4.559
.599	5.042		
.859	5.105		
1.285	5.192		
1.714	5.263		
2.144	5.324		
2.570	5.380		
3.000	5.431		
3.429	5.474		
3.858	5.514		
4.288	5.550		
5.144	5.611		
5.999	5.657		
6.858	5.690		
7.717	5.710		
8.573	5.715		
11.100	5.715		

Transition section and nozzle coordinates	
Internal	
NS	r
8.572	4.559
9.748	4.577
10.922	4.628
12.098	4.699
13.272	4.788
14.448	4.884
15.621	4.978
16.797	5.067
17.970	5.138

Figure 11. Sketch showing details of inlet section of nacelles. All dimensions are in centimeters.

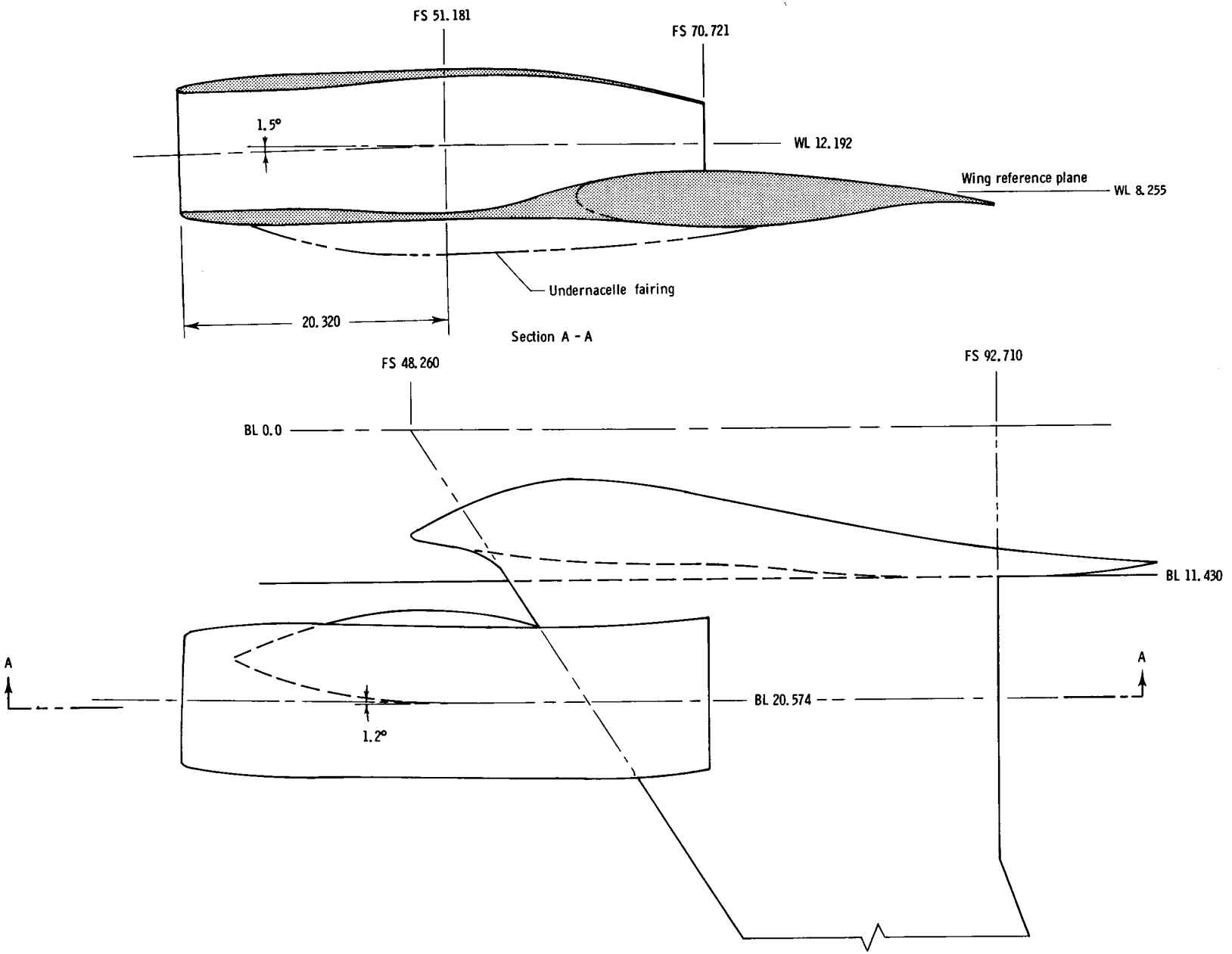

Figure 12. Sketch showing installation of contoured upper-surface nacelle configurations (USBC and USBC-F) on wing. All dimensions are in centimeters unless otherwise noted.

L-79-4317

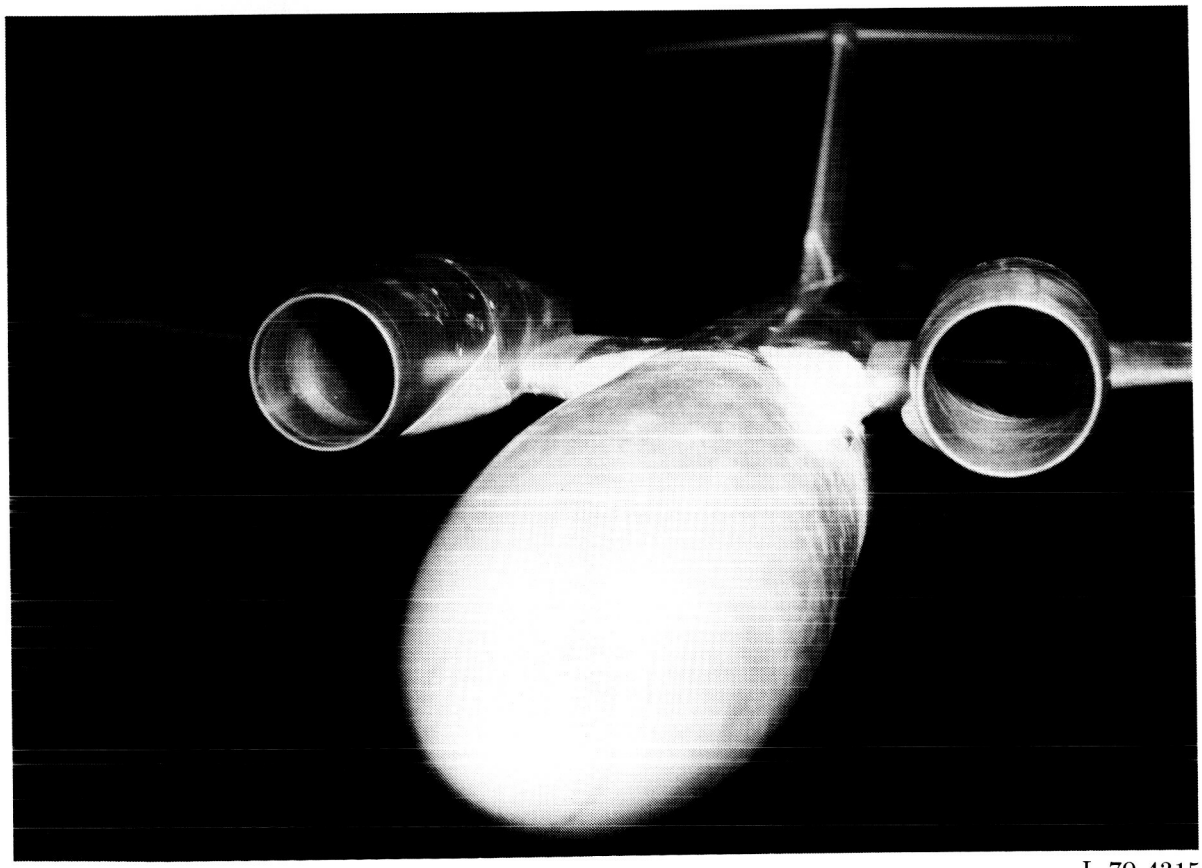

L-79-4315

(a) Model with contoured nacelles (USBC).

Figure 13. Photographs of contoured nacelle configurations in the Langley 16-Foot Transonic Tunnel.

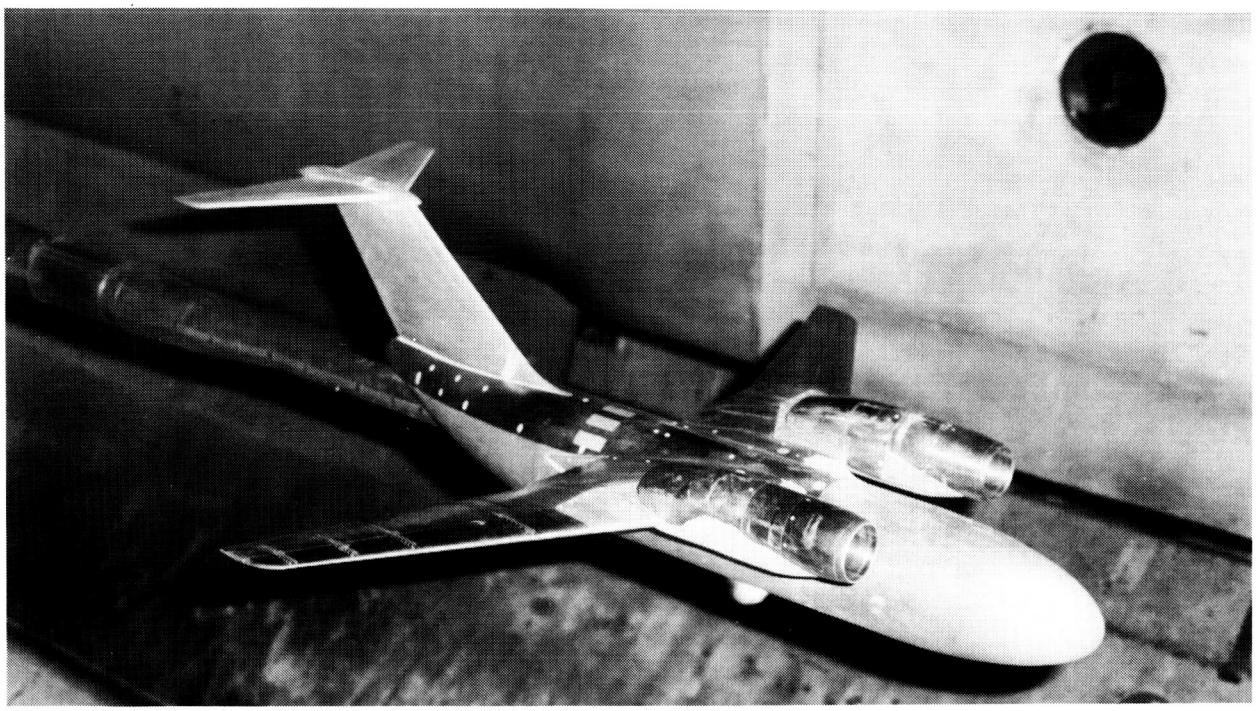

L-79-4348

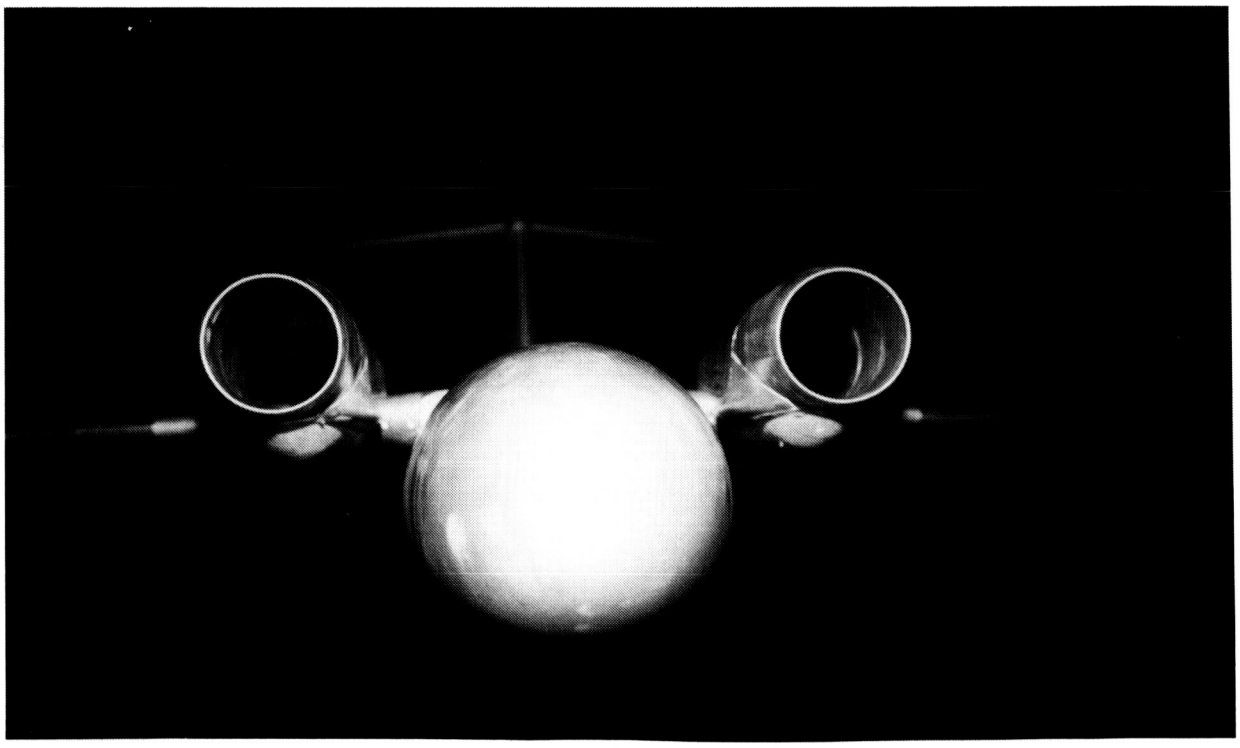

L-79-4346

(b) Model with contoured nacelles and undernacelle fairing (USBC-F).

Figure 13. Concluded.

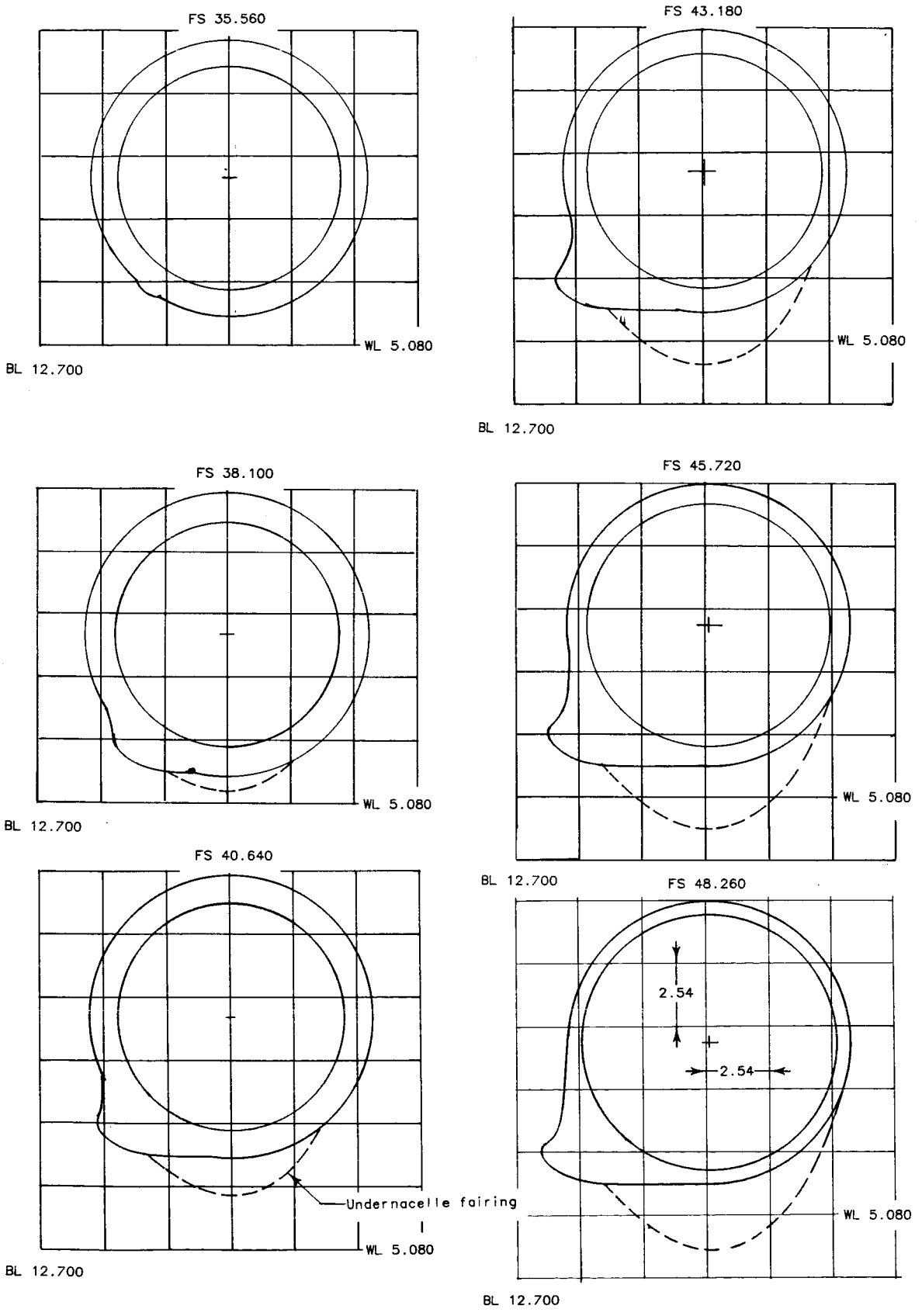

Figure 14. Cross sections of contoured nacelle and undernacelle fairing.

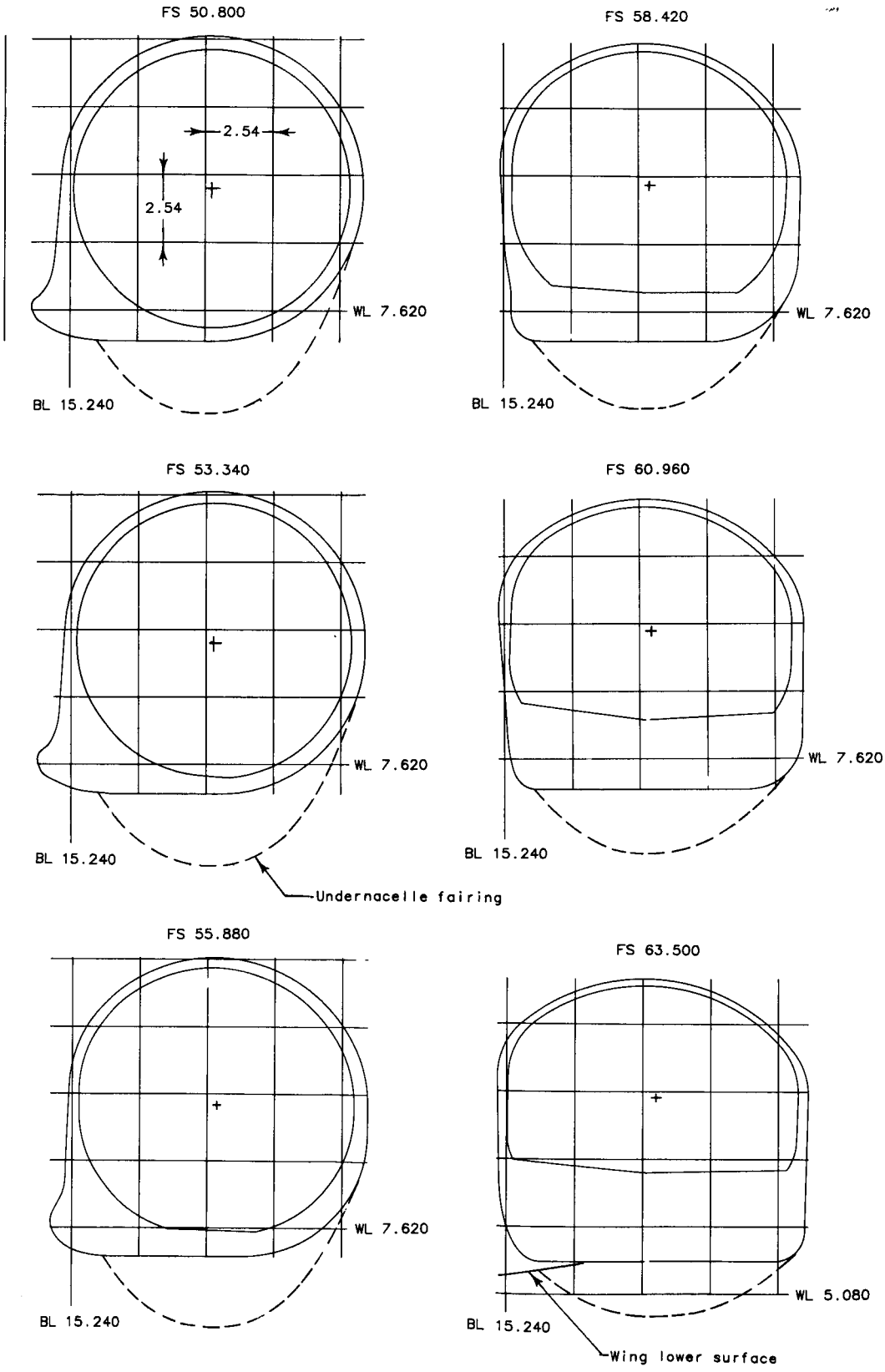

Figure 14. Continued.

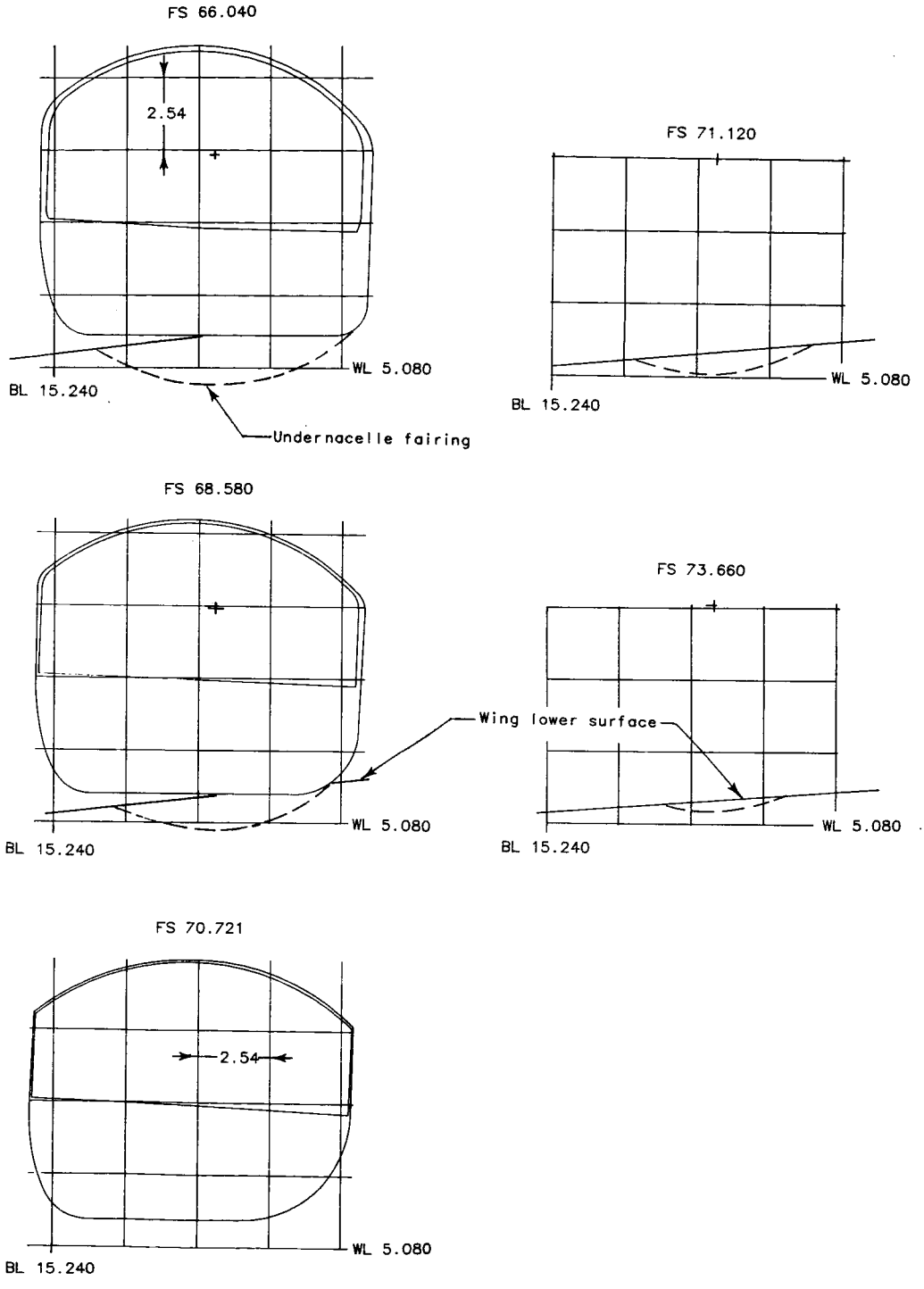

Figure 14. Concluded.

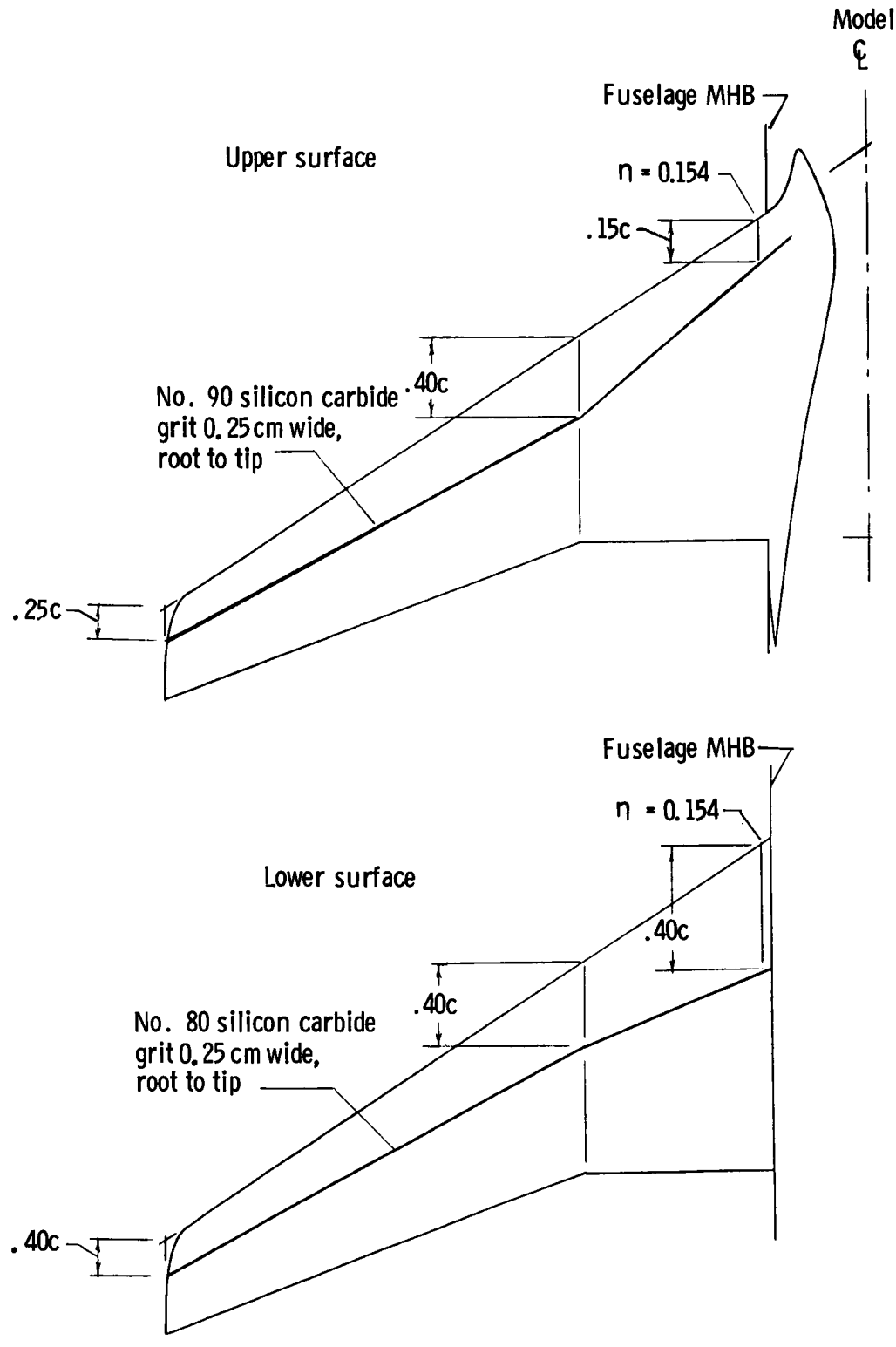

Figure 15. Sketch showing locations of boundary-layer transition strips on wing.

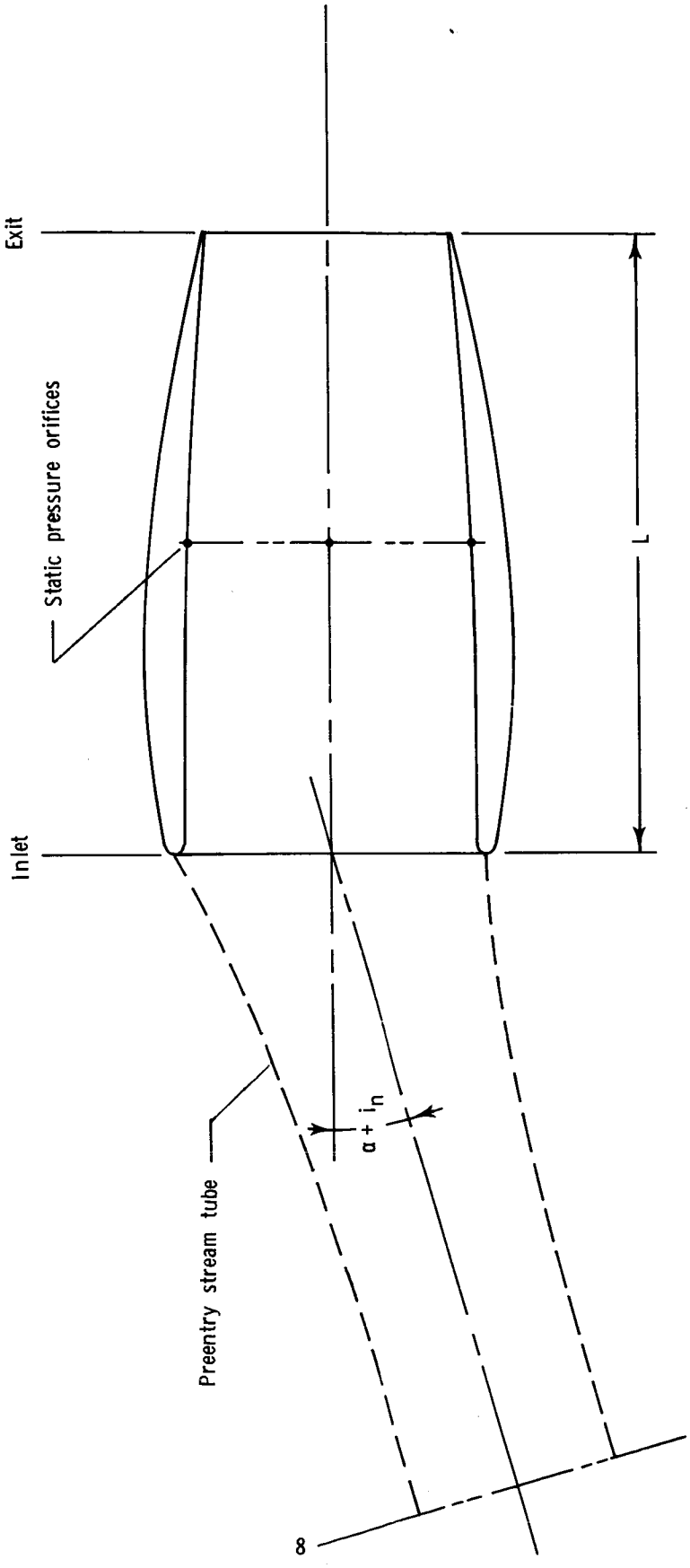

Figure 16. Schematic drawing of flow field for flow-through nacelle.

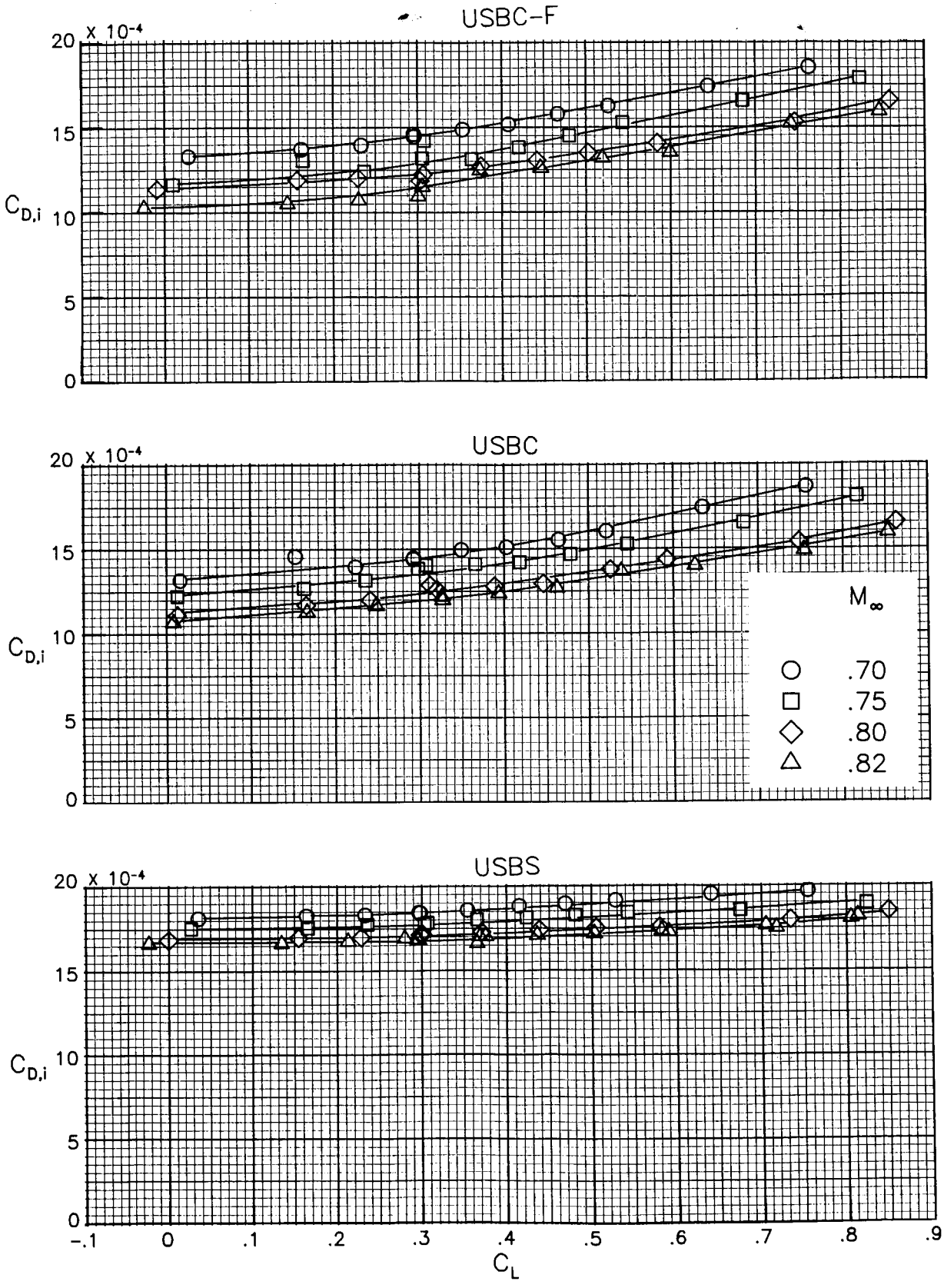

Figure 17. Variation of nacelle internal drag with lift coefficient and Mach number.

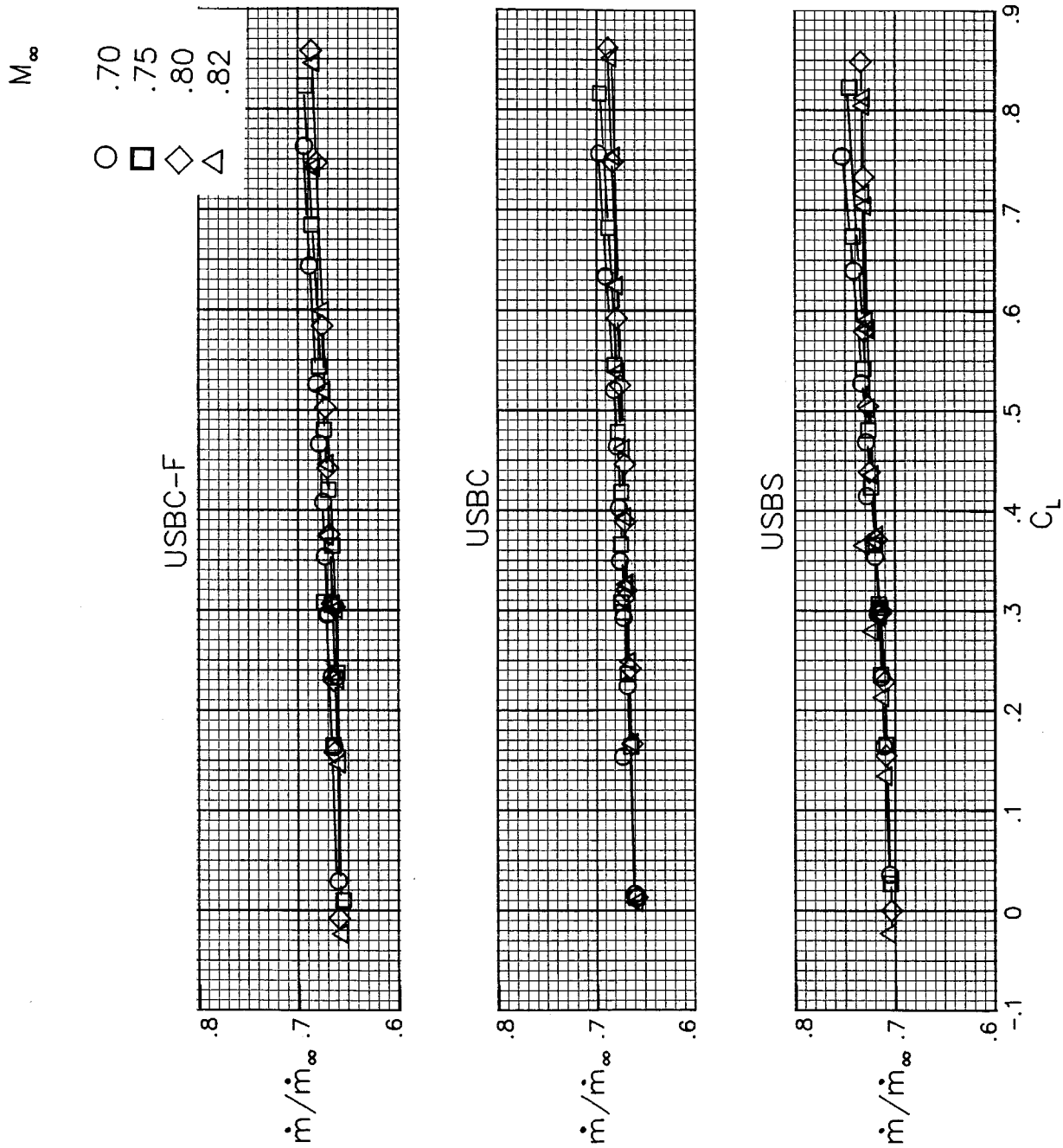

Figure 18. Variation of nacelle mass flow ratio with lift coefficient and Mach number.

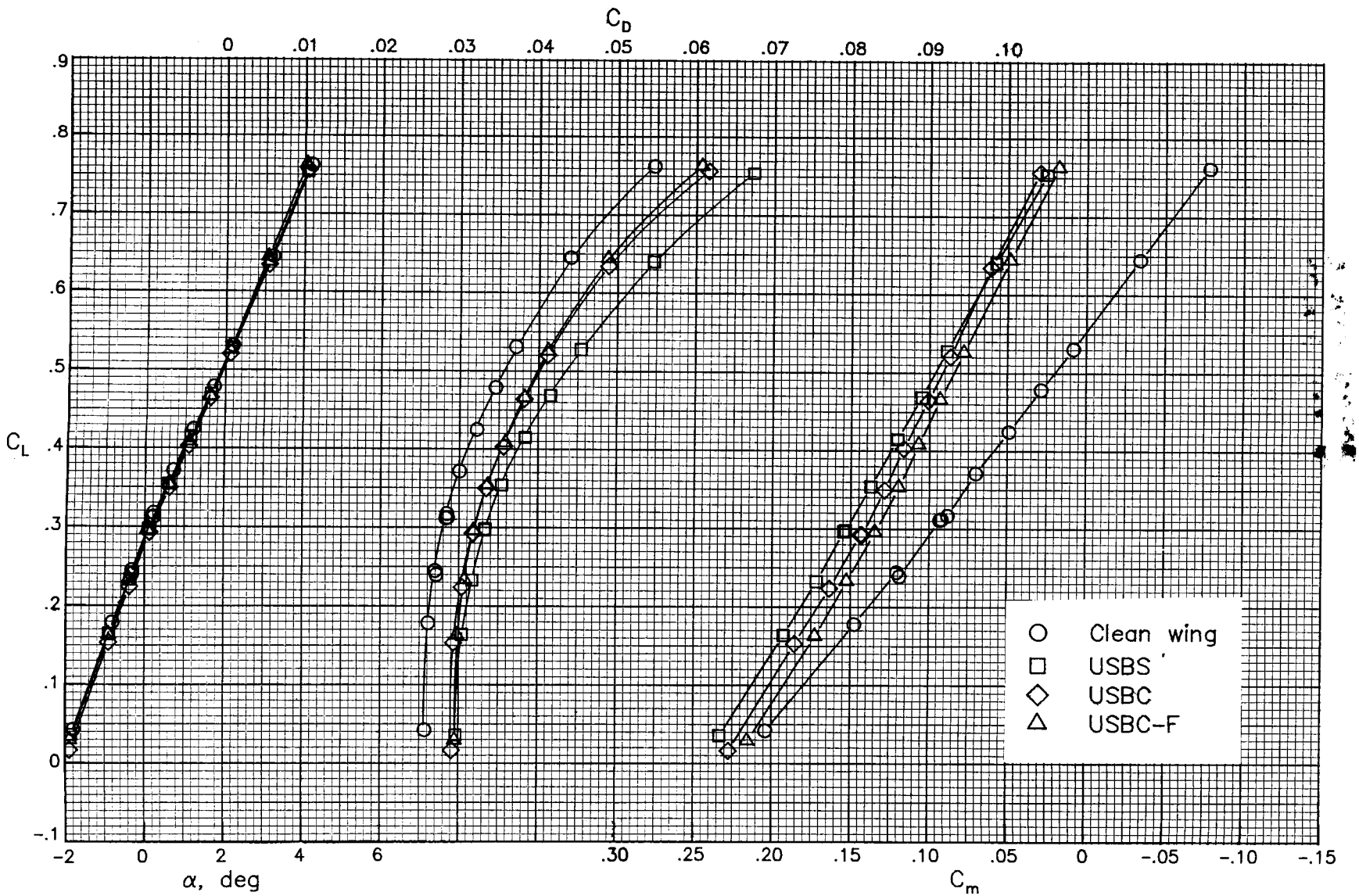

(a) $M = 0.70$.

Figure 19. Effects of nacelle addition, nacelle contouring, and undernacelle fairing on basic longitudinal aerodynamic characteristics of configuration.

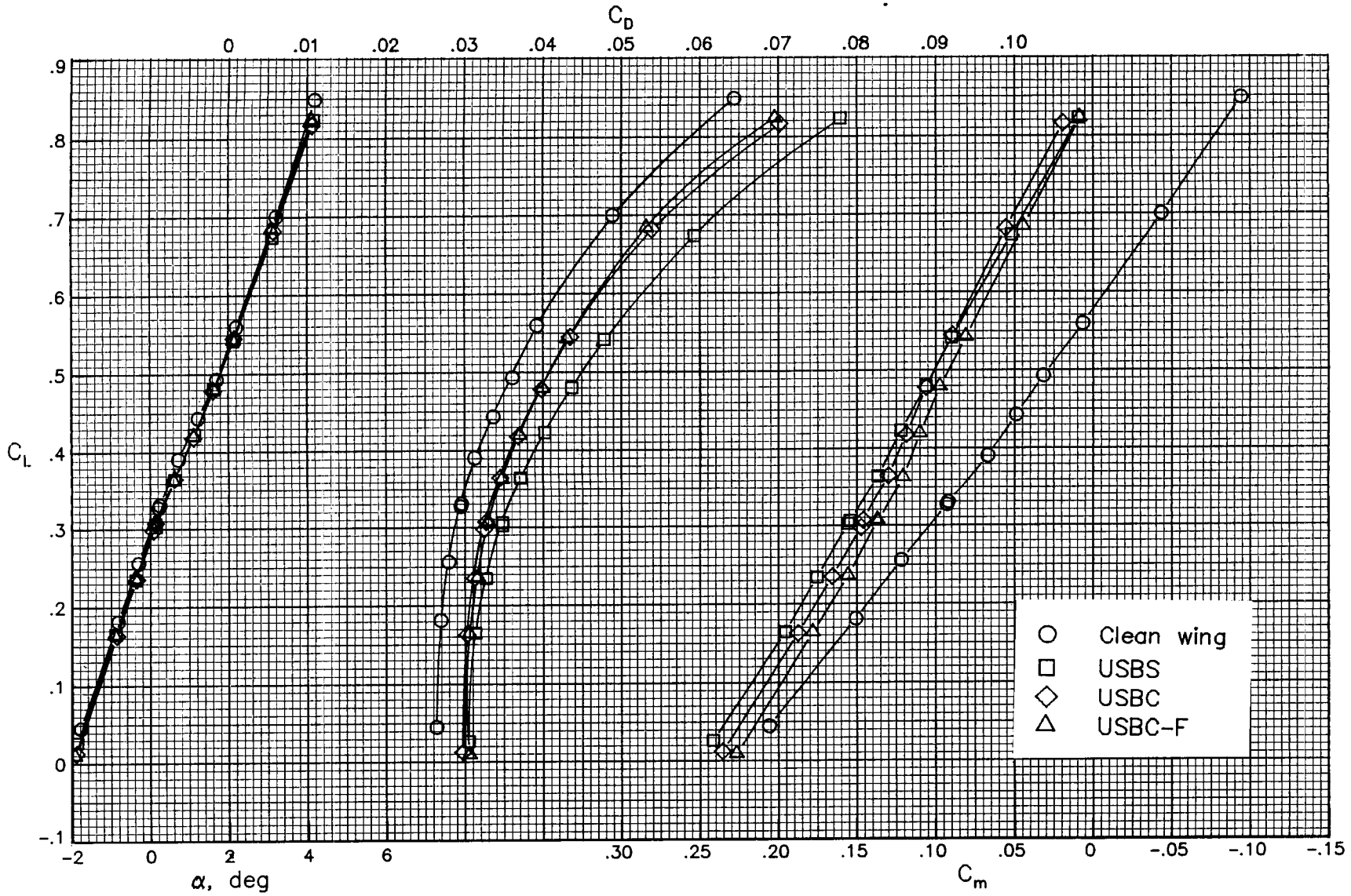

(b) $M = 0.75$.

Figure 19. Continued.

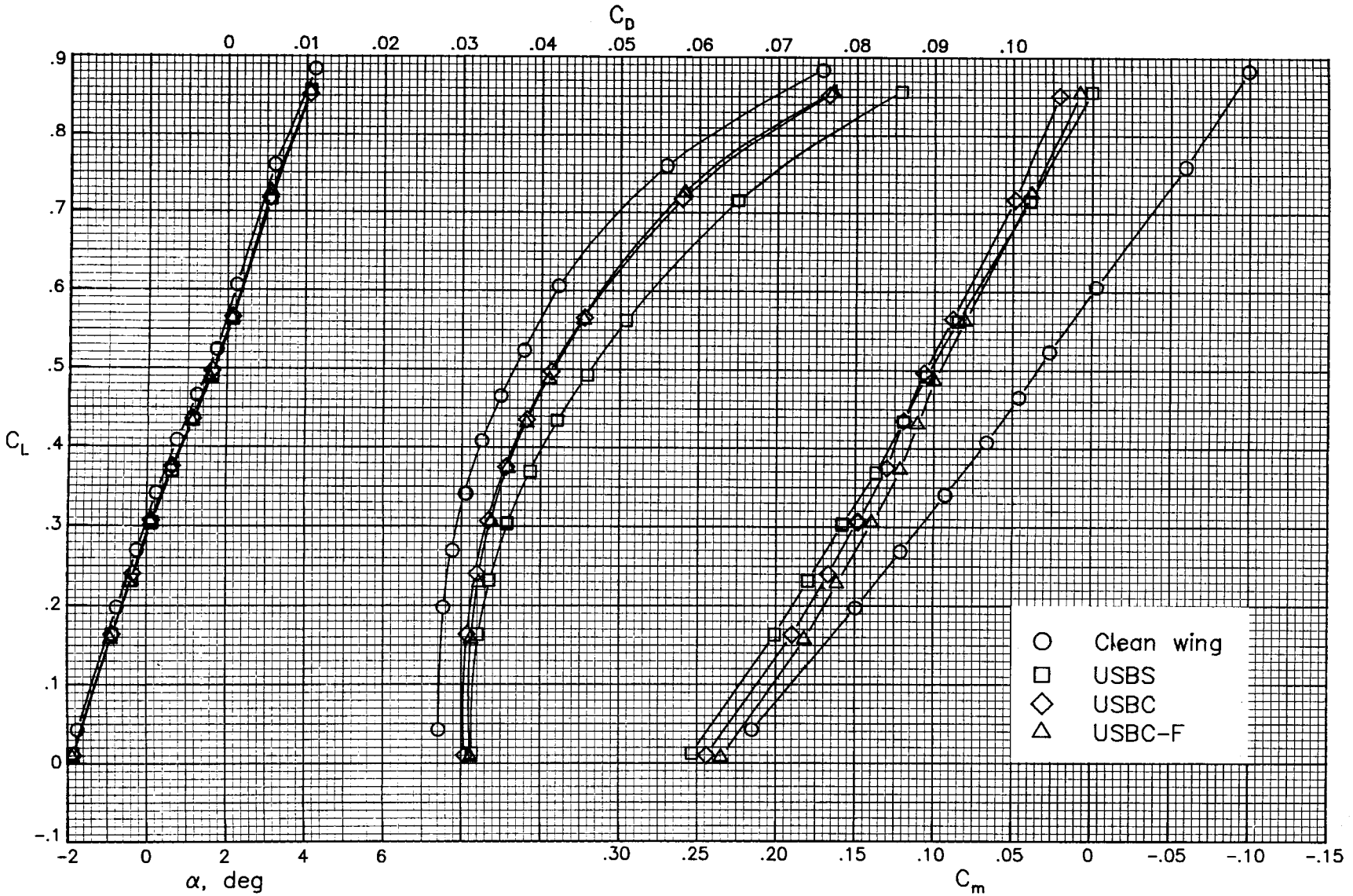

(c) $M = 0.78$.

Figure 19. Continued.

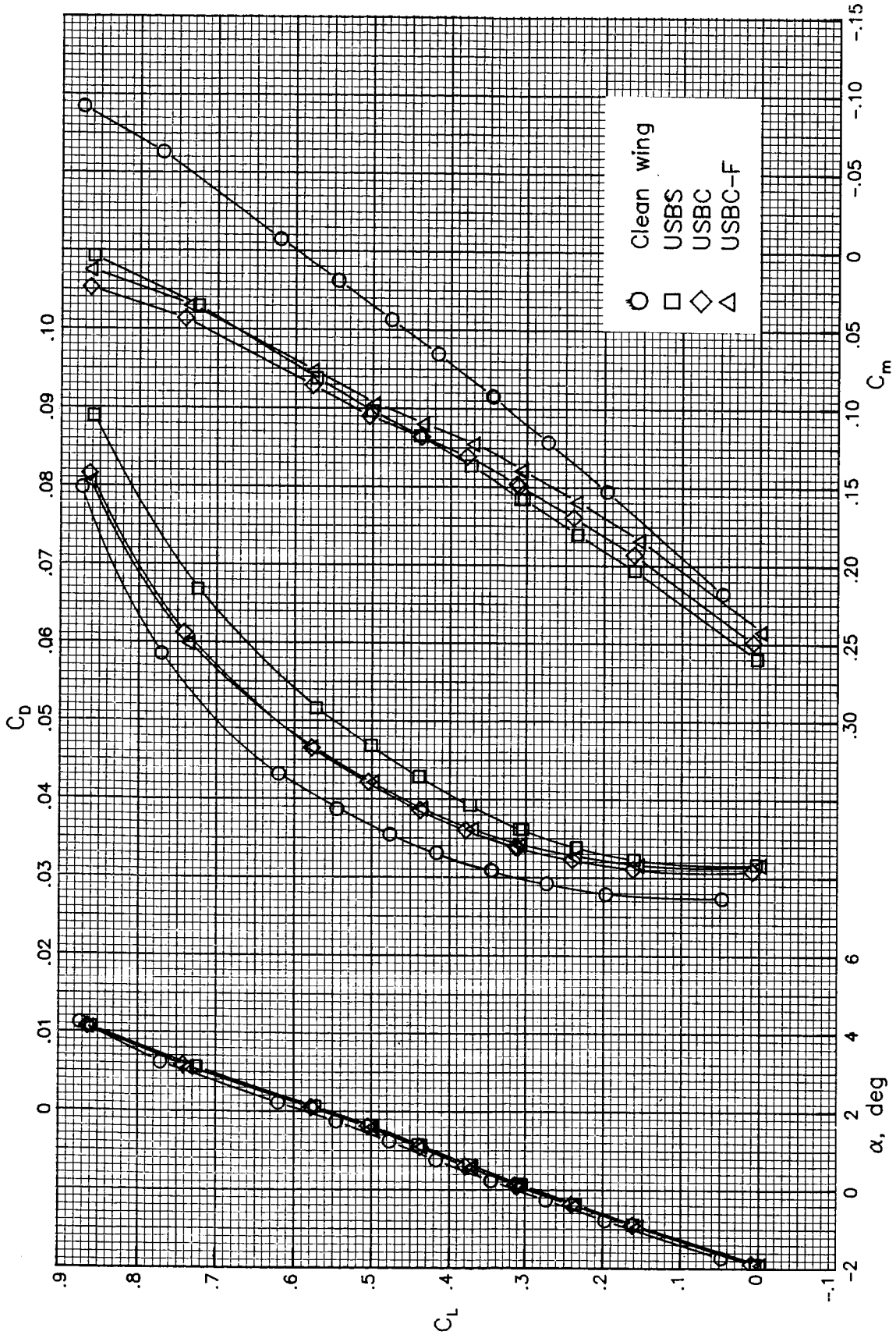

(d) $M = 0.79$.

Figure 19. Continued.

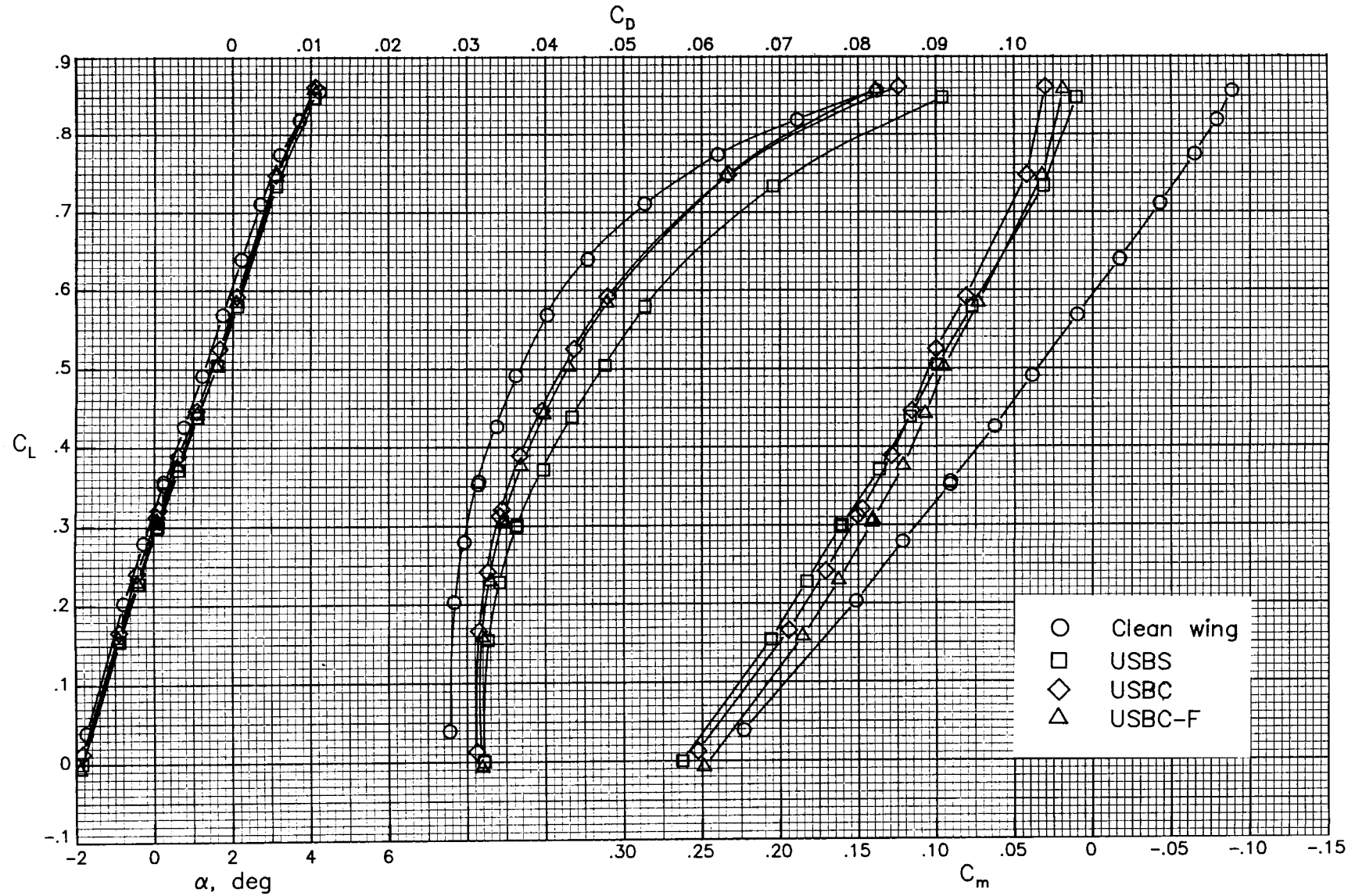

(e) $M = 0.80$.

Figure 19. Continued.

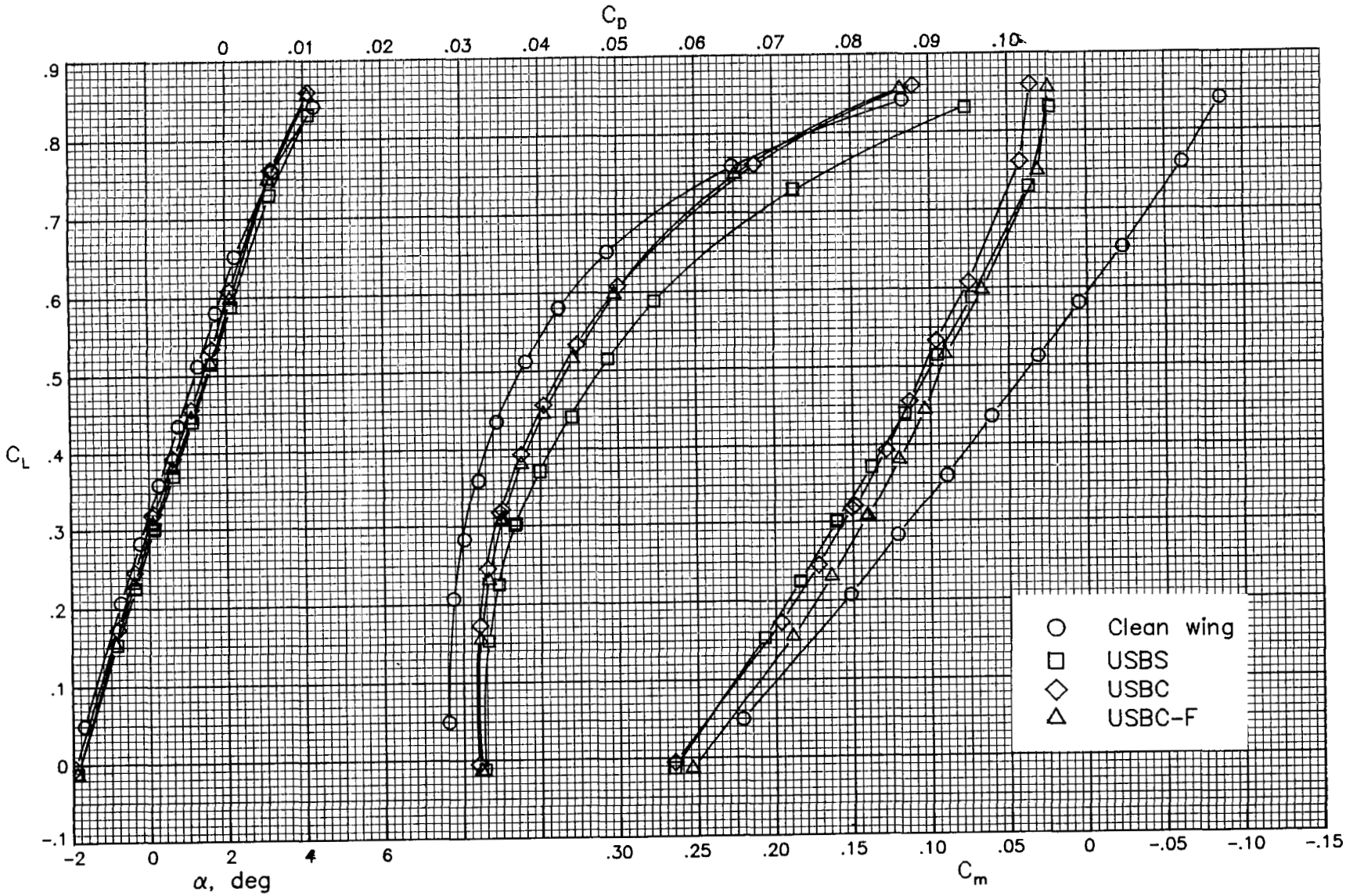

(f) $M = 0.81$.

Figure 19. Continued.

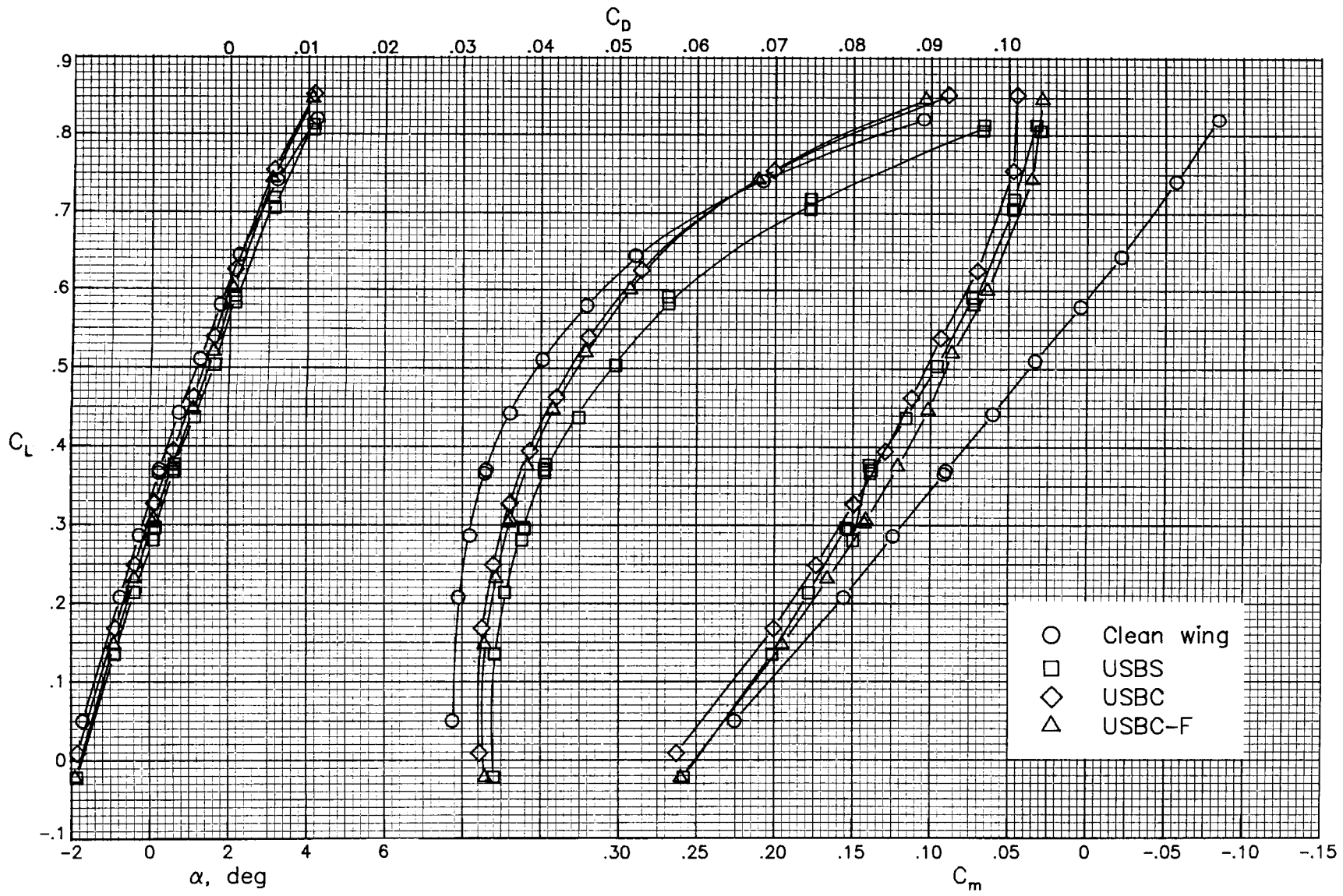

(g) $M = 0.82$.

Figure 19. Concluded.

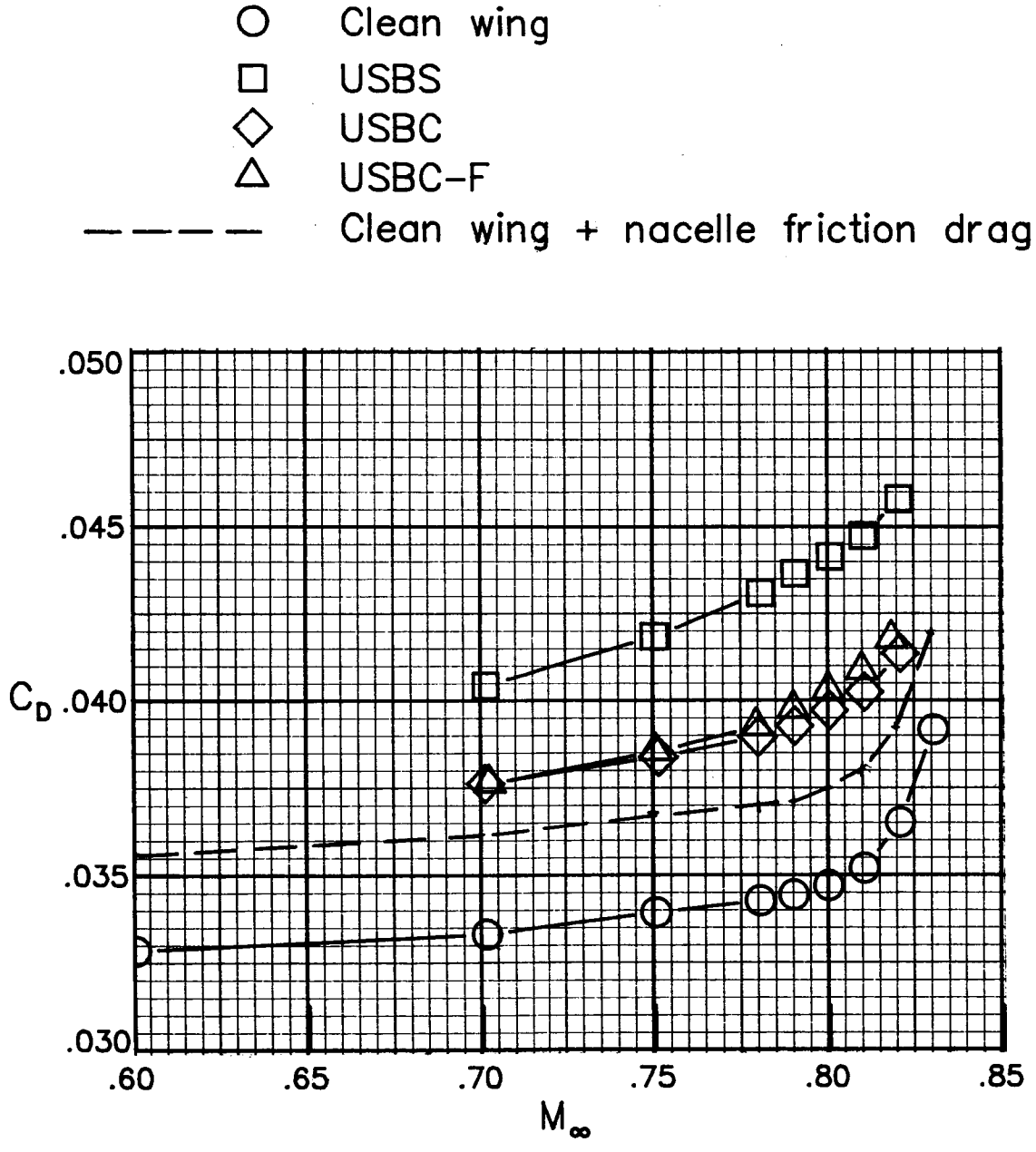

Figure 20. Effect of nacelle installation on drag coefficient at $C_L = 0.45$.

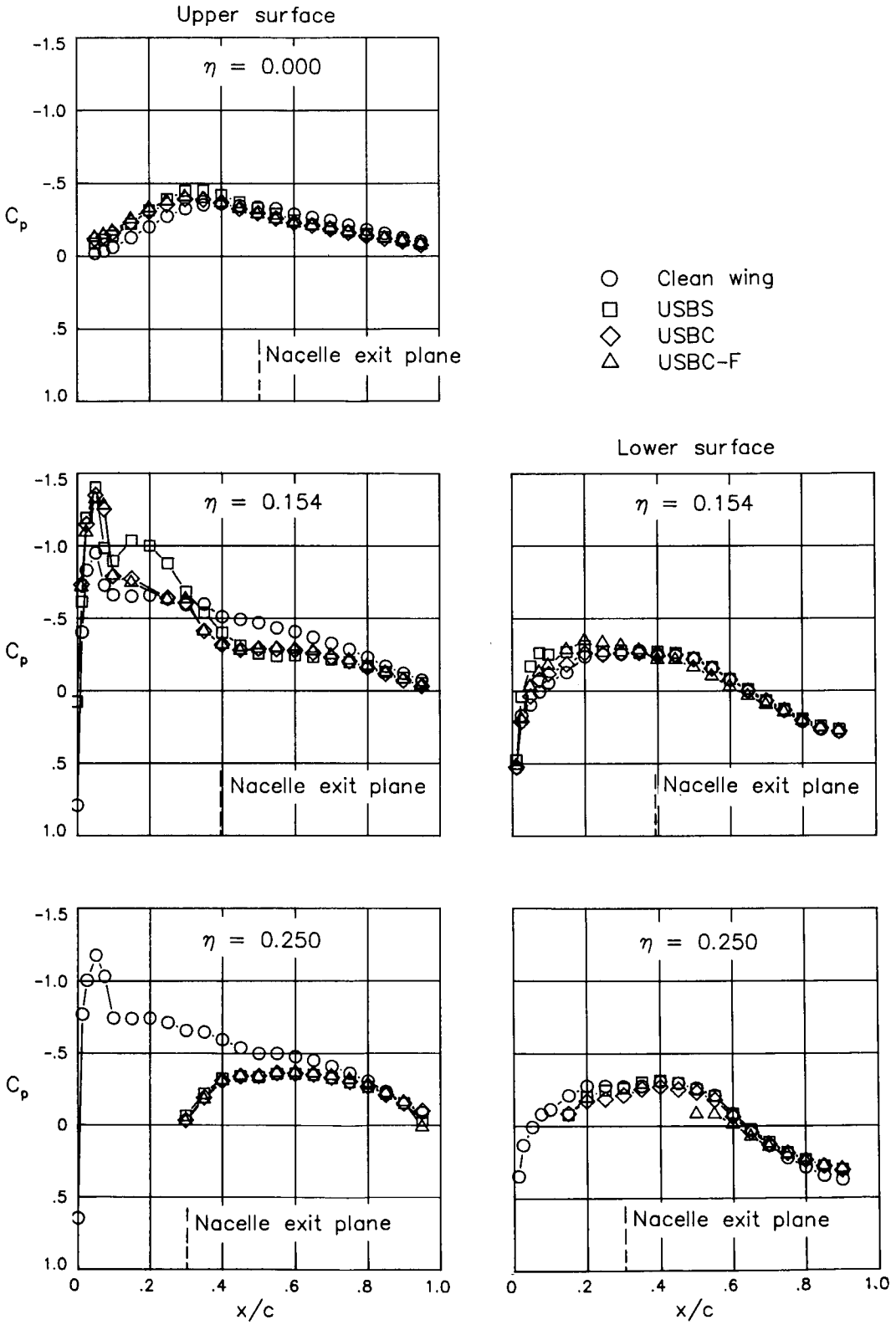

Figure 21. Effects of nacelle installations on wing pressure distributions at $M_\infty = 0.70$ and $C_L = 0.47$.

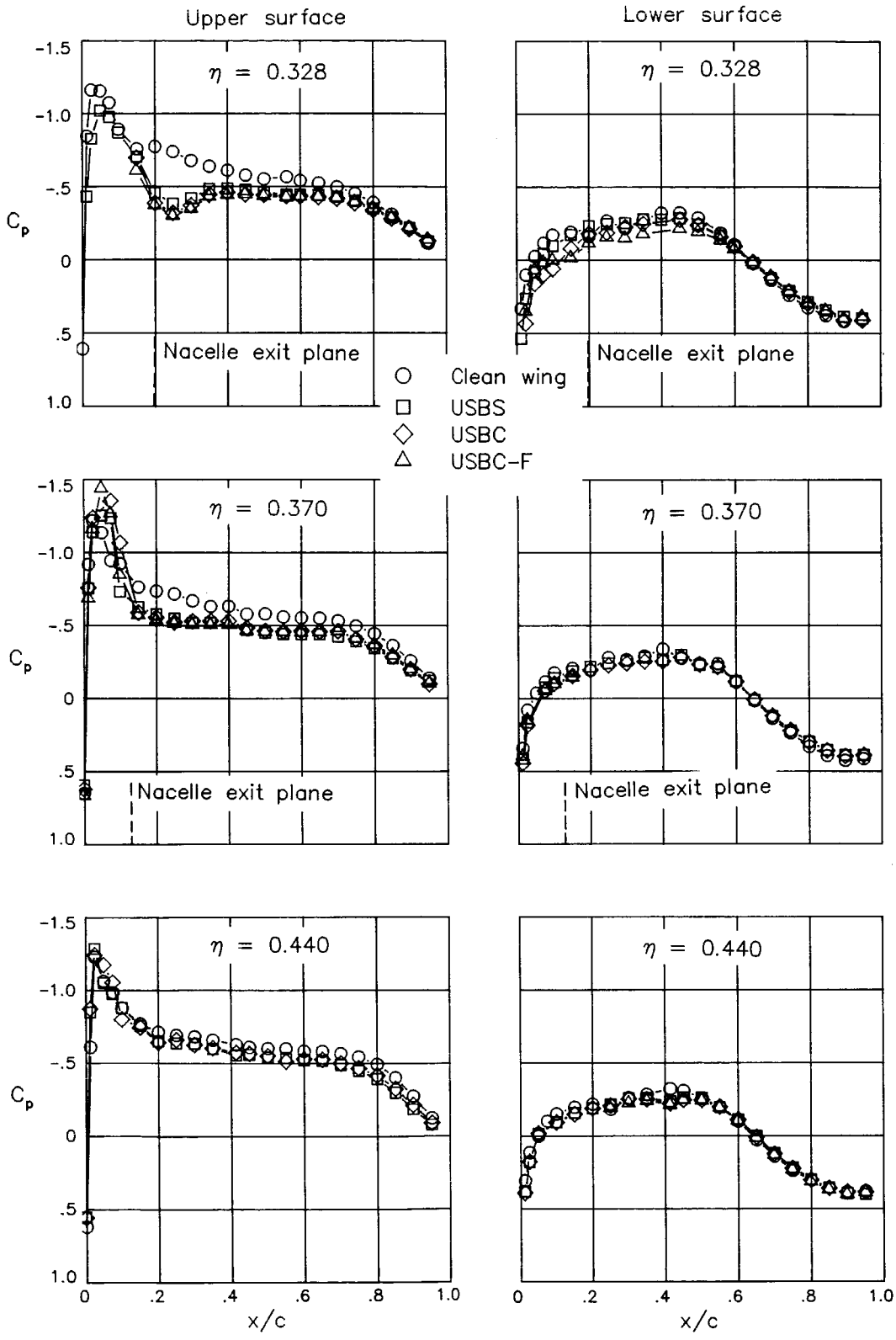

Figure 21. Continued.

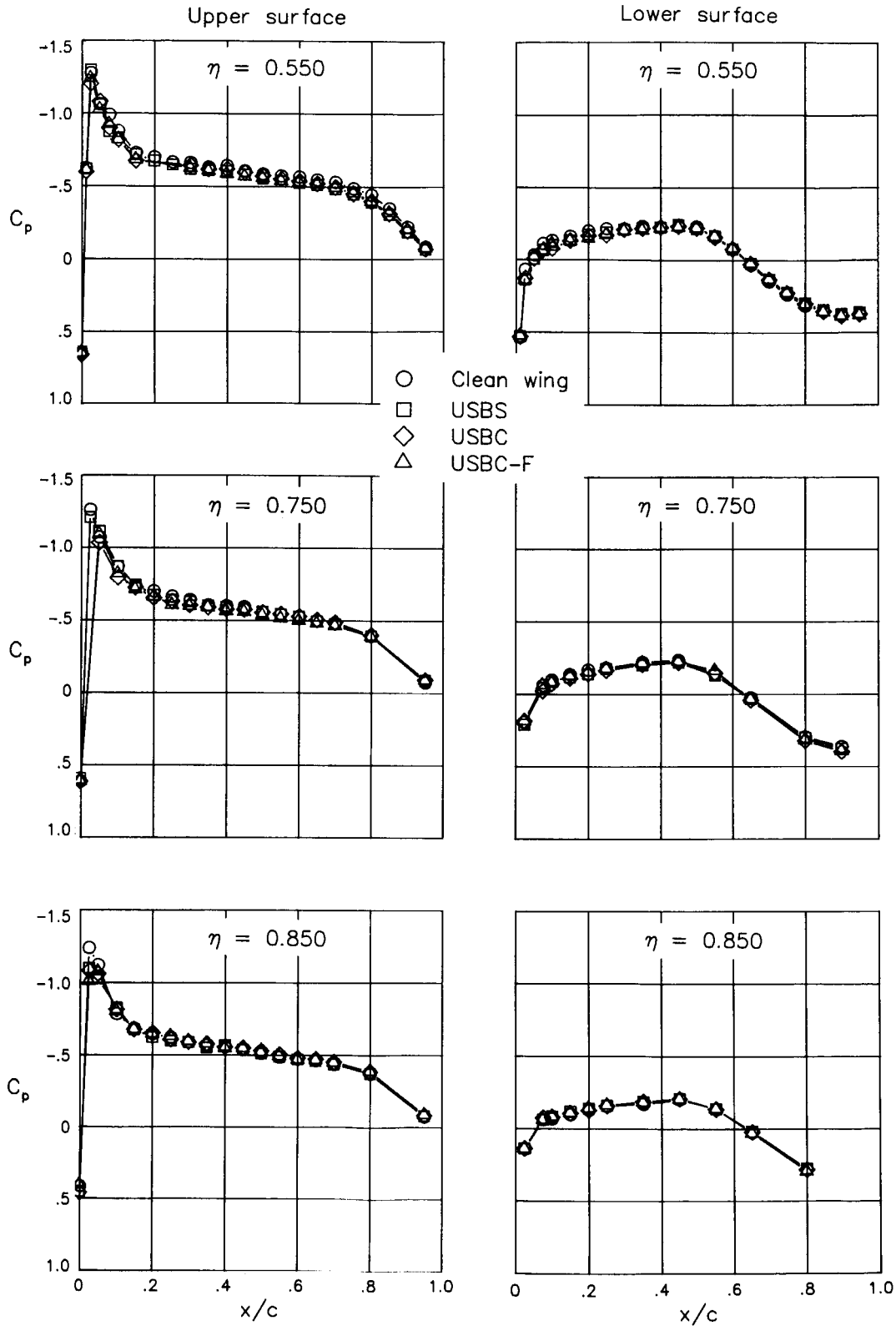

Figure 21. Concluded.

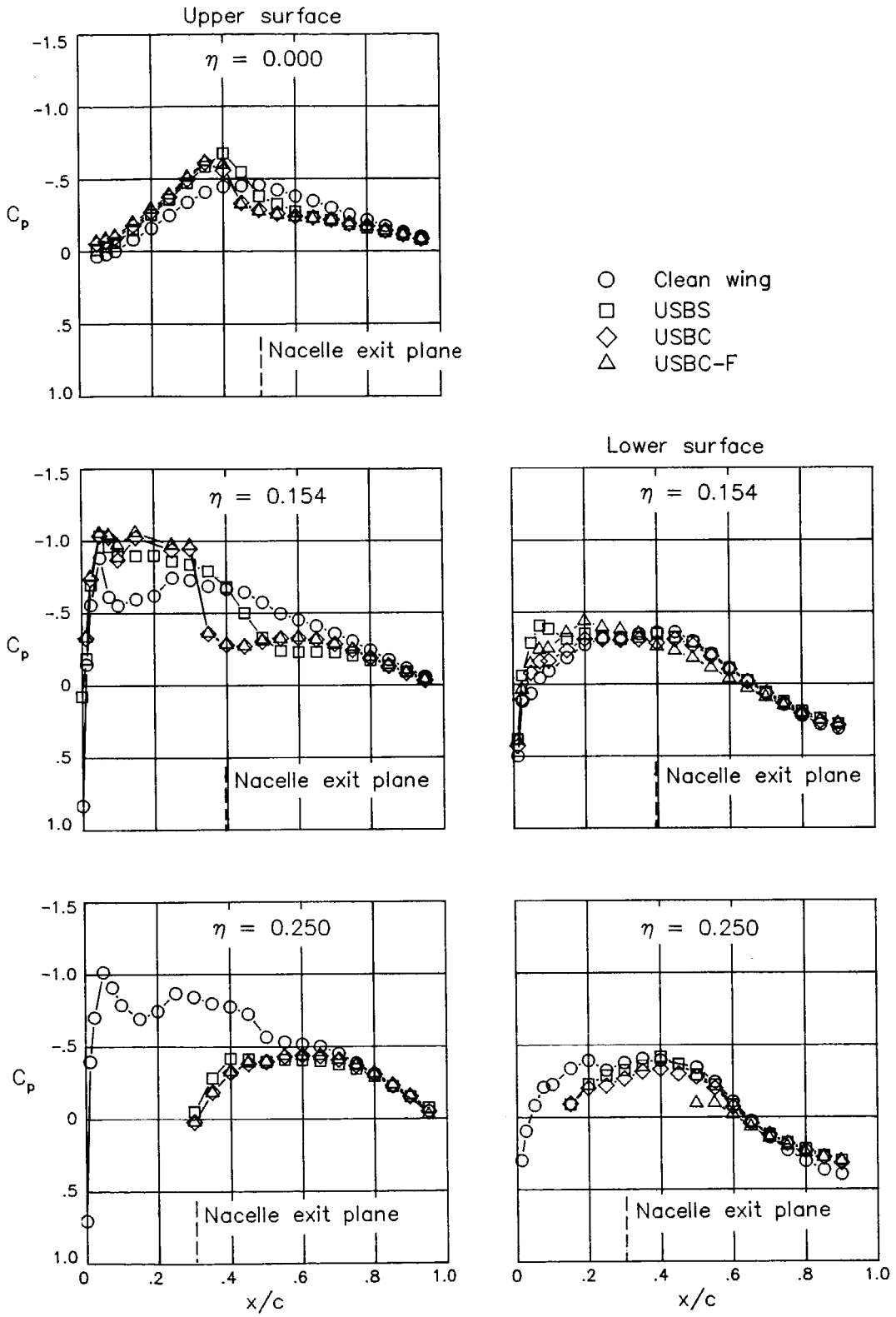

Figure 22. Effects of nacelle installations on wing pressure distributions at $M_\infty = 0.80$ and $C_L = 0.45$.

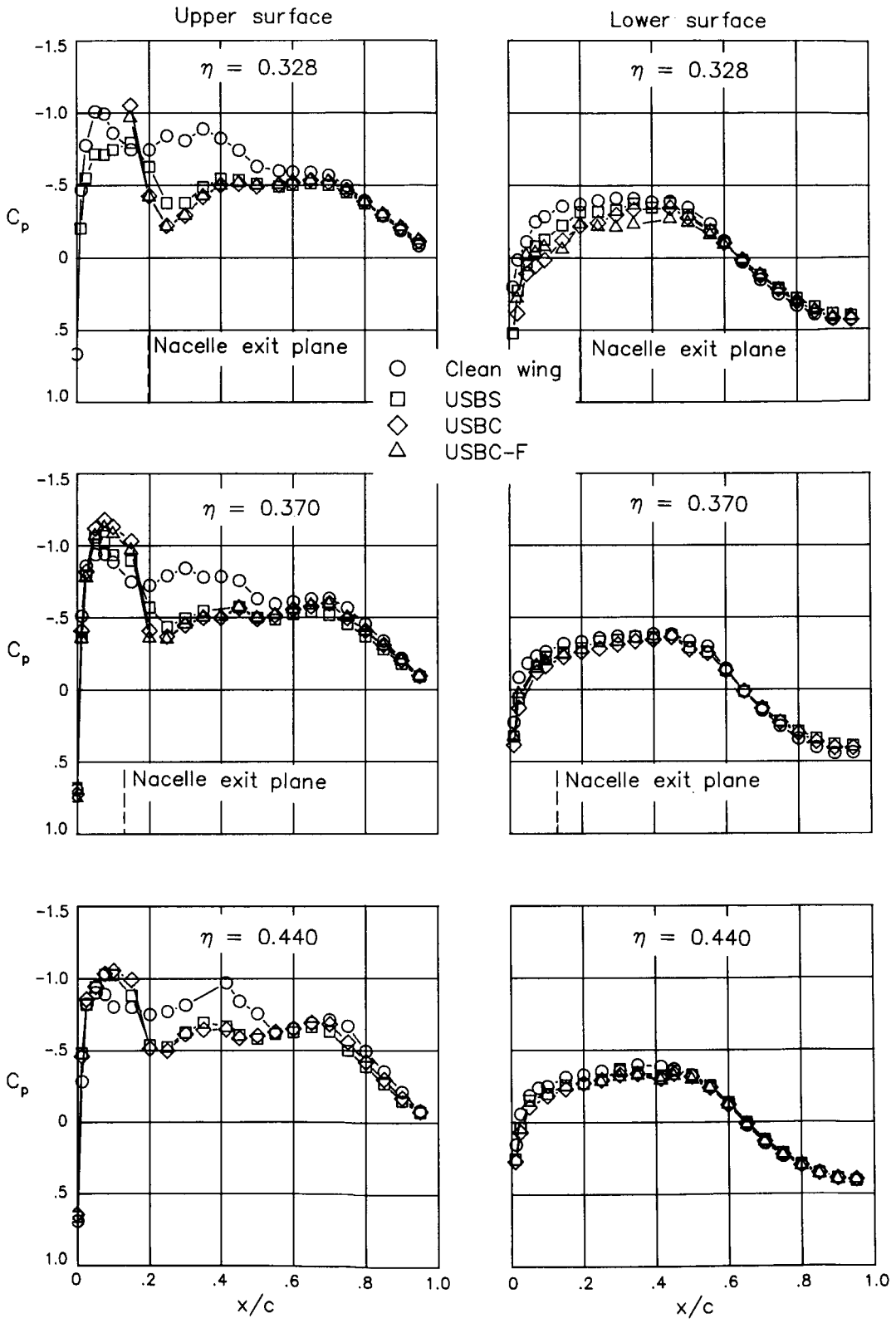

Figure 22. Continued.

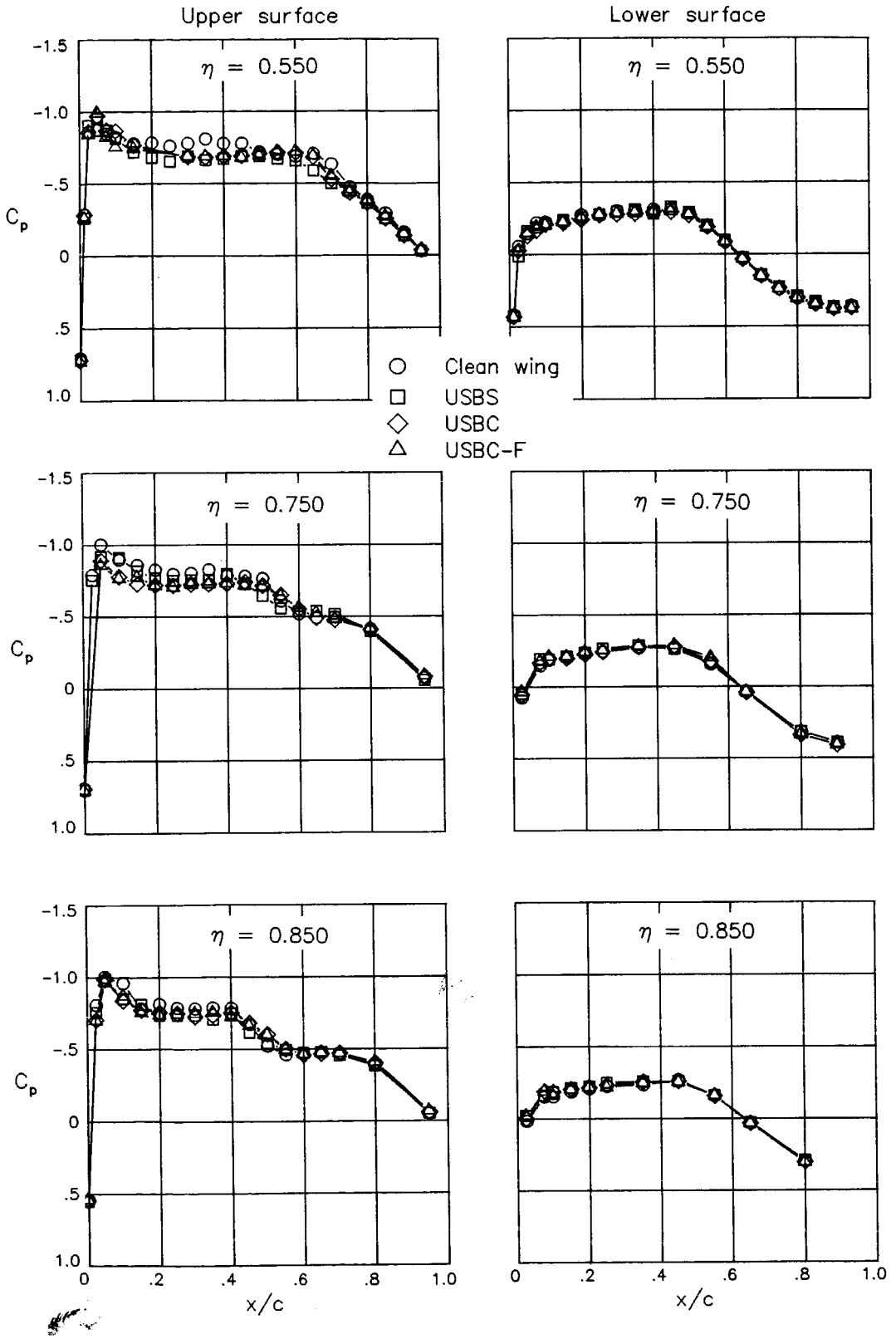

Figure 22. Concluded.

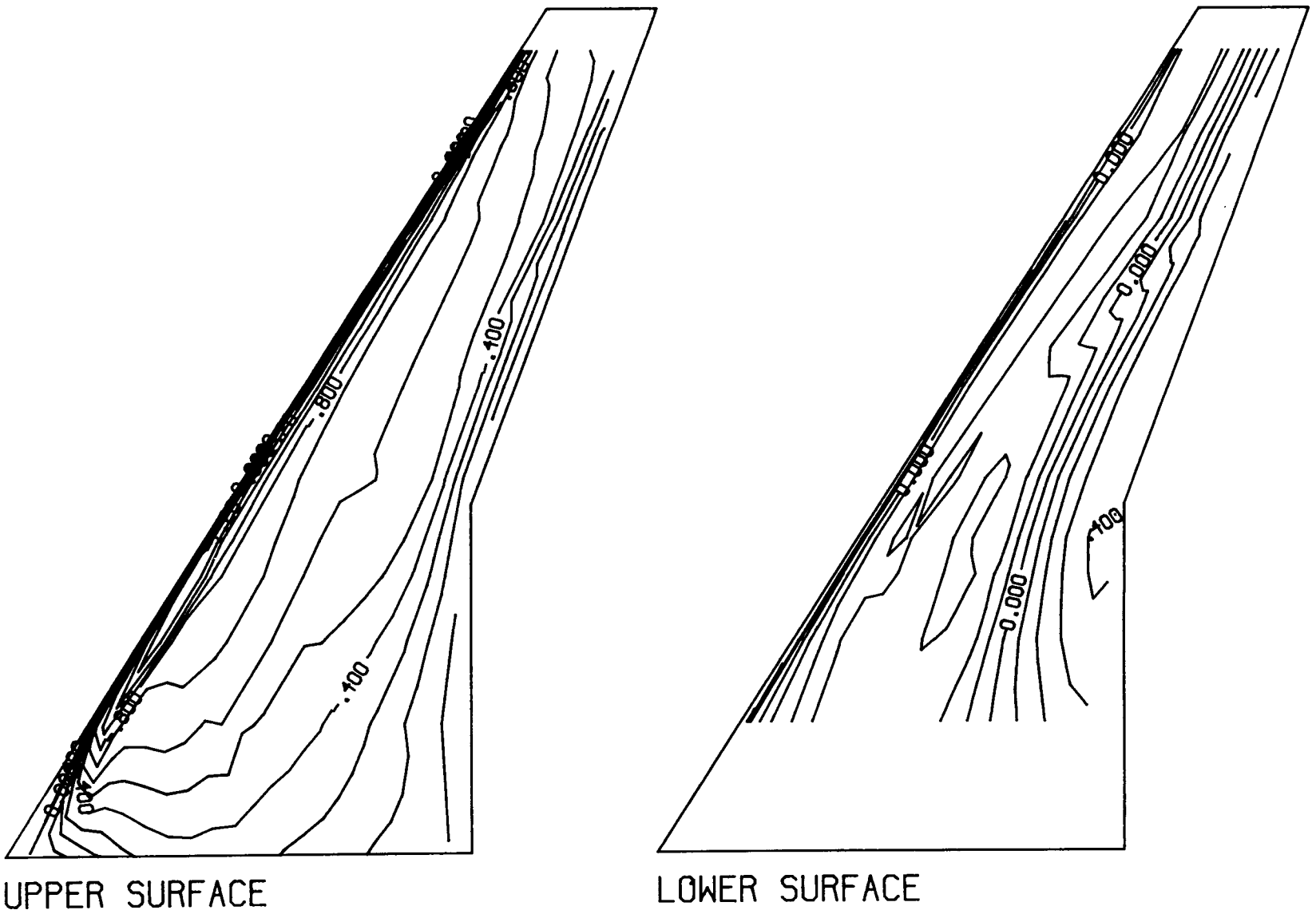

(a) Clean wing.

Figure 23. Wing pressure coefficient contours at $M_\infty = 0.70$ and $C_L = 0.45$.

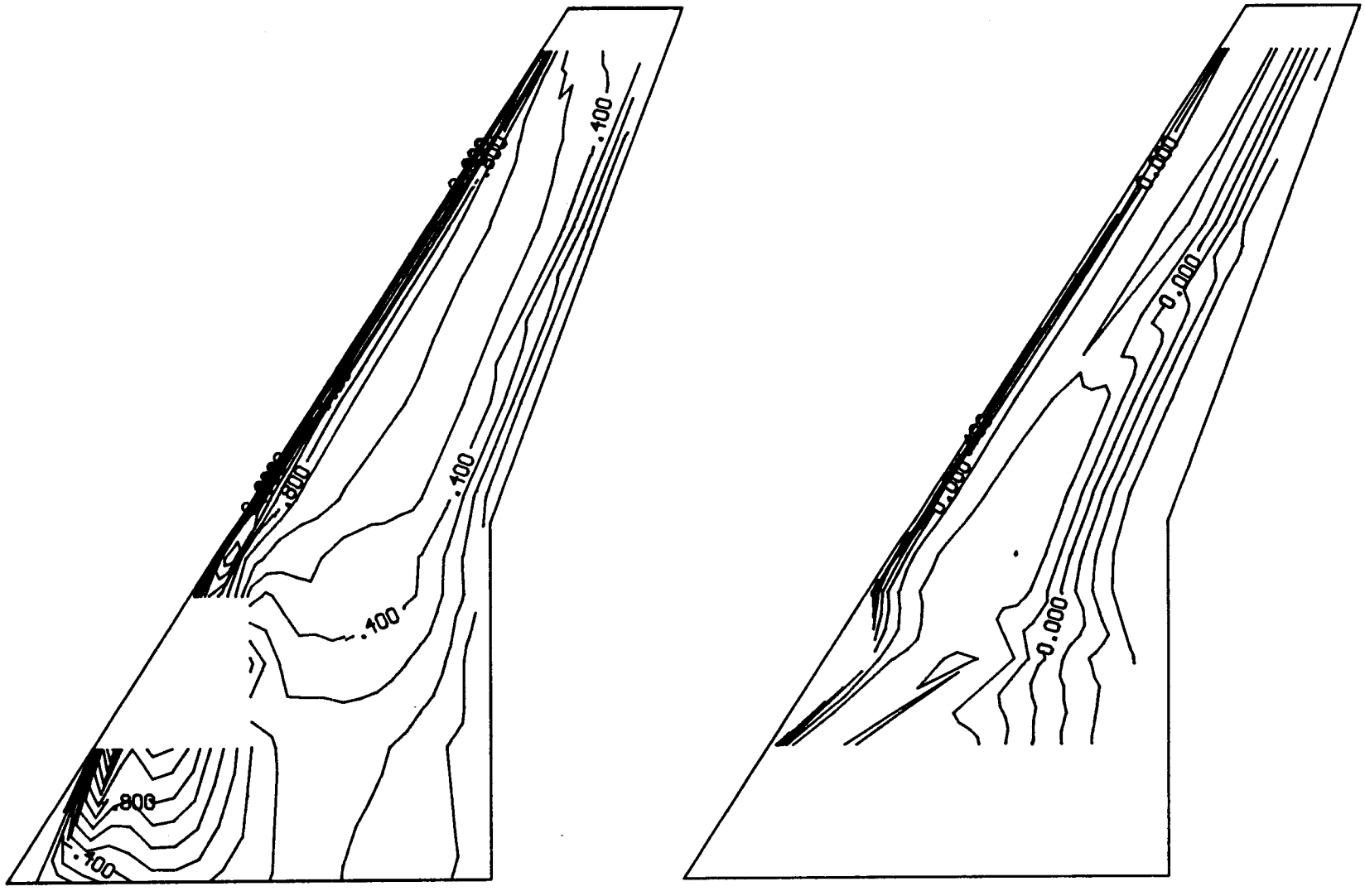

(b) USBS.

Figure 23. Continued.

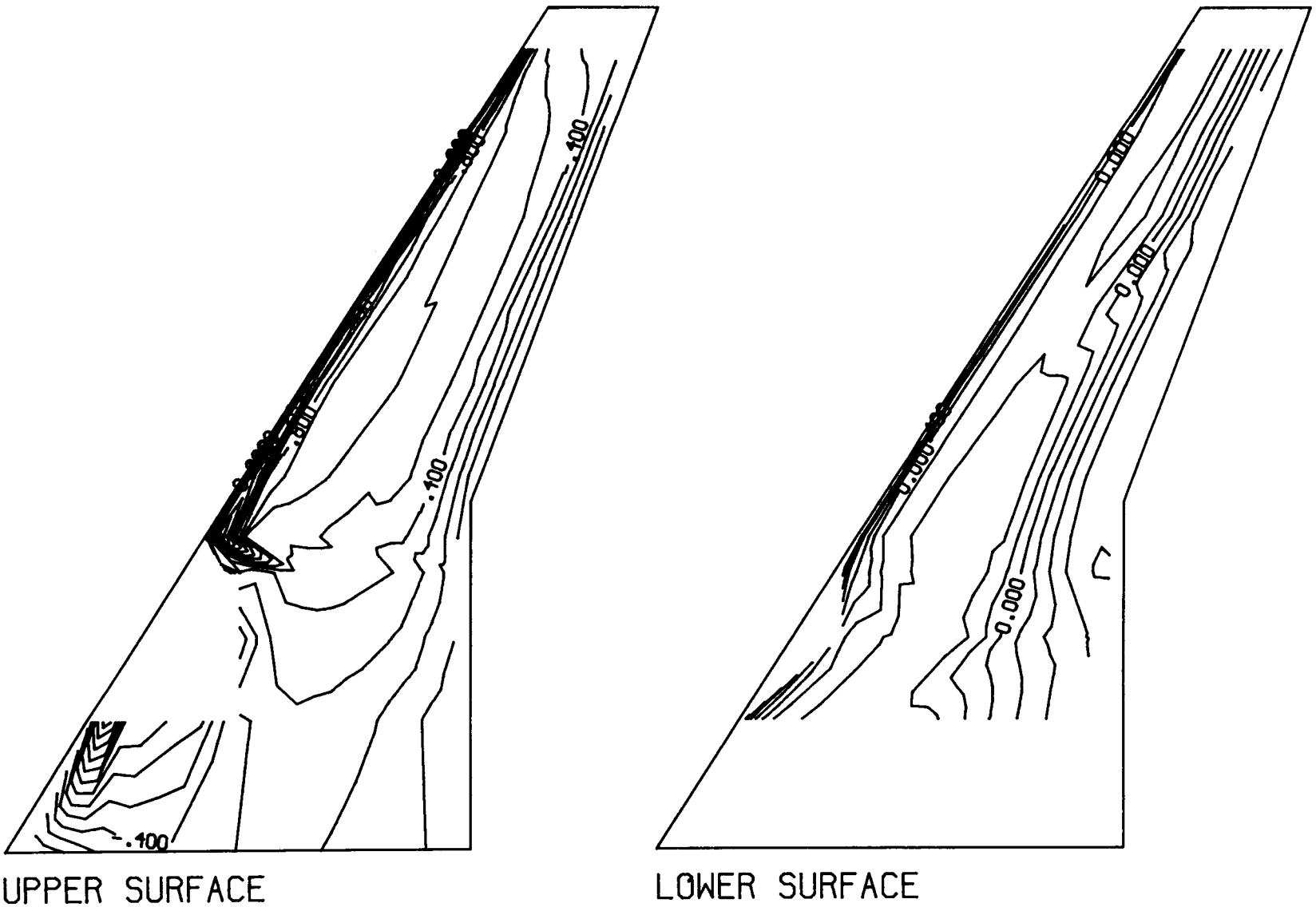

(c) USBC.

Figure 23. Continued.

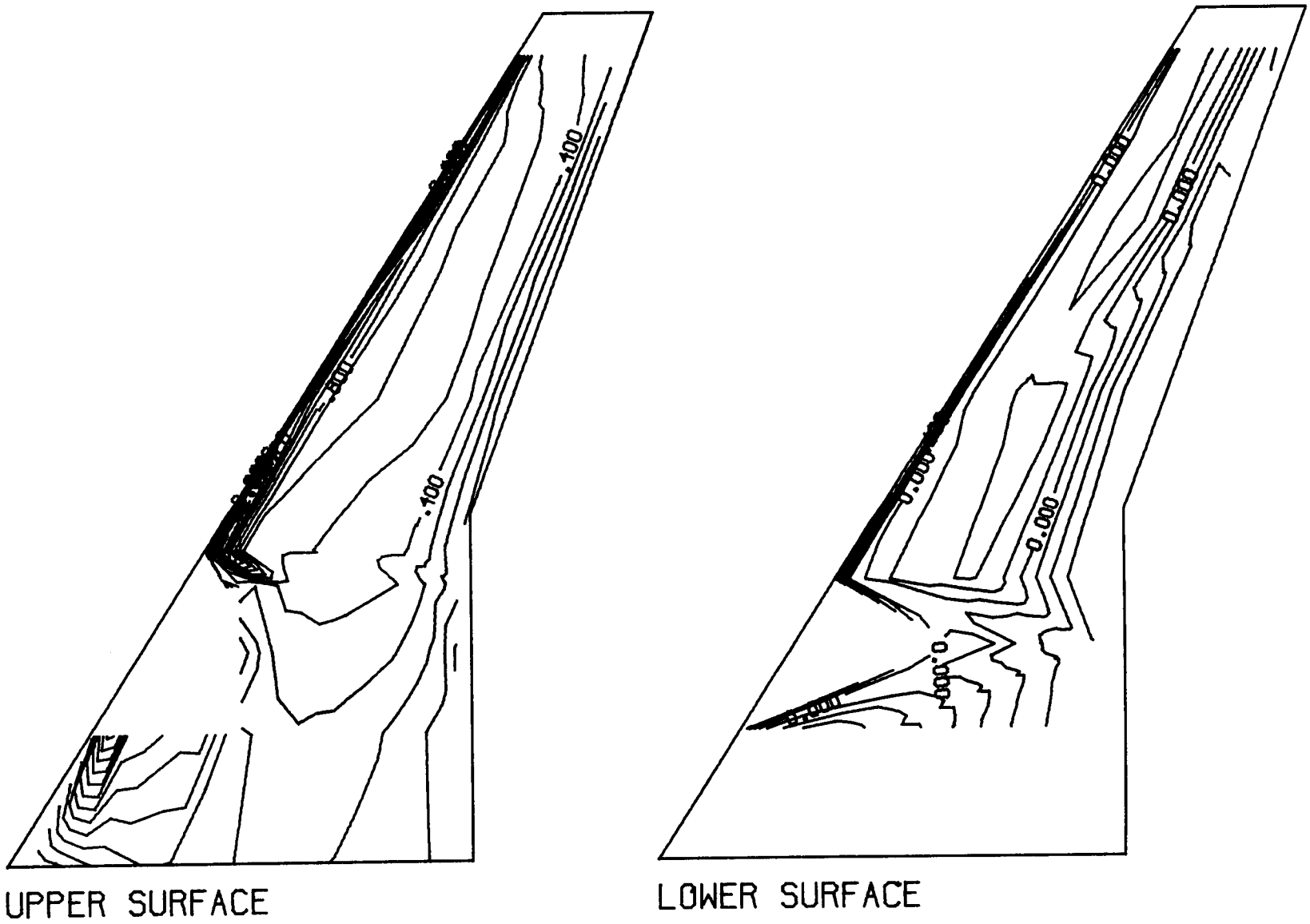

(d) USBC-F.

Figure 23. Concluded.

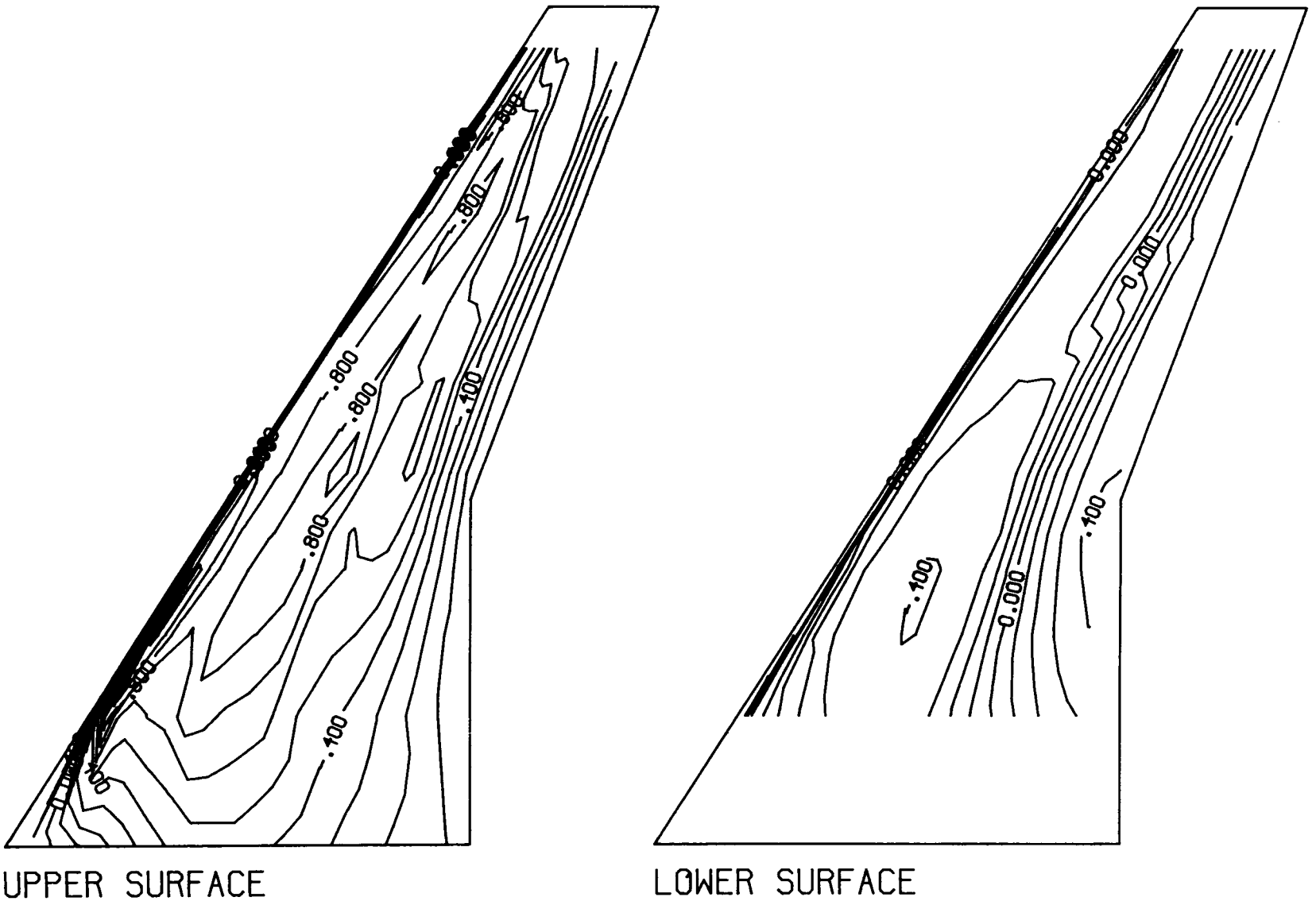

(a) Clean wing.

Figure 24. Wing pressure coefficient contours at $M_\infty = 0.80$ and $C_L = 0.45$.

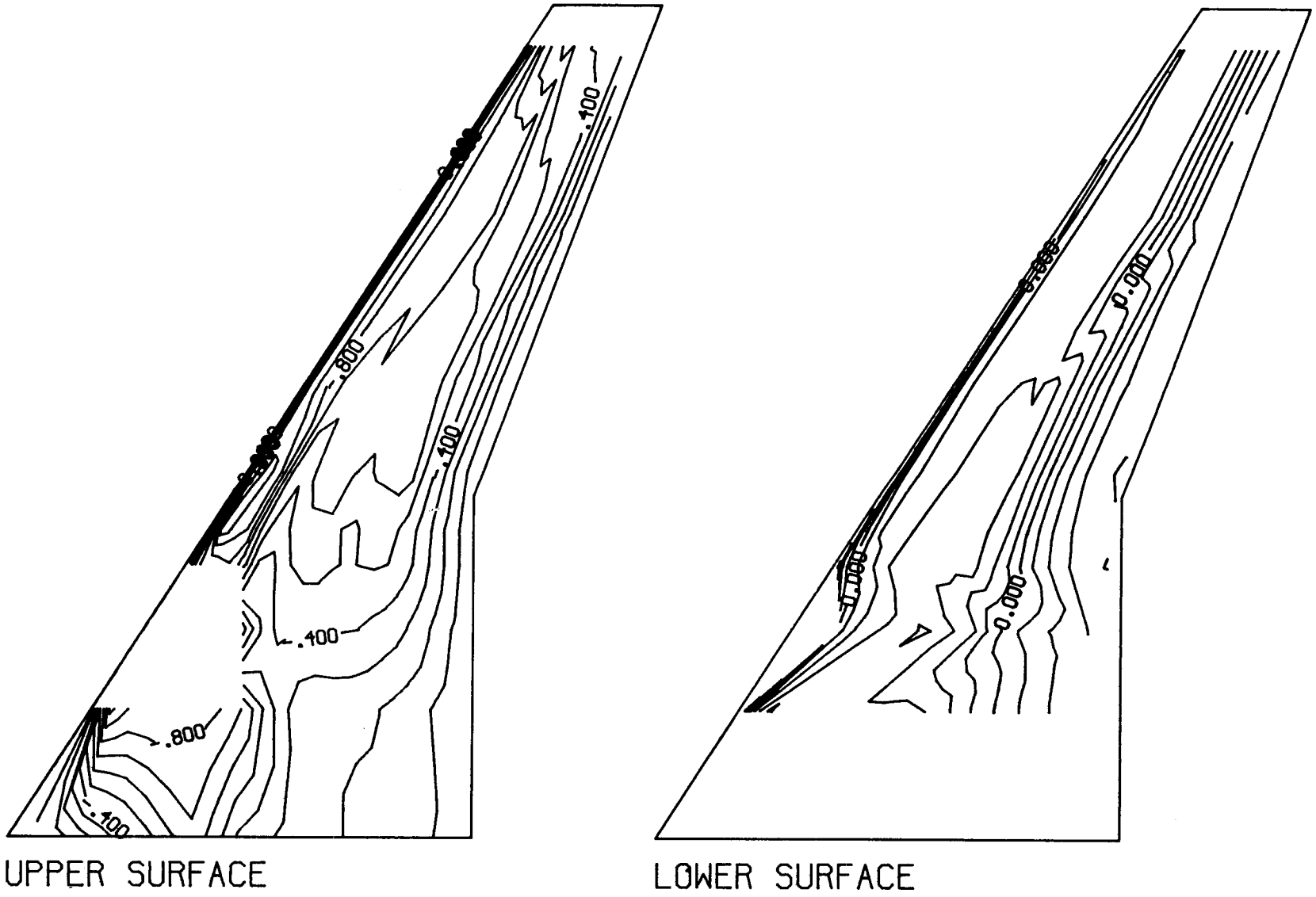

(b) USBS.

Figure 24. Continued.

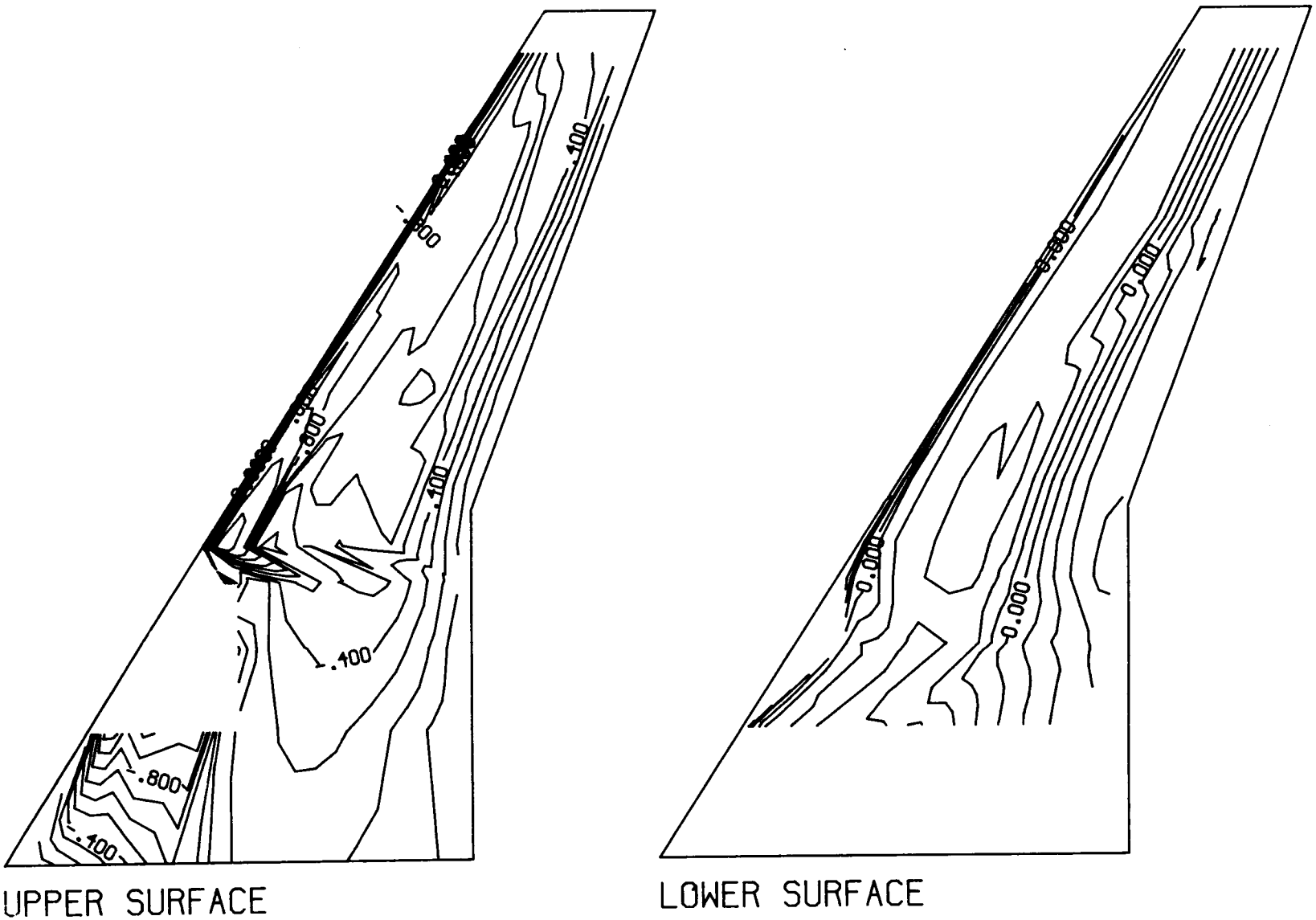

(c) USBC.

Figure 24. Continued.

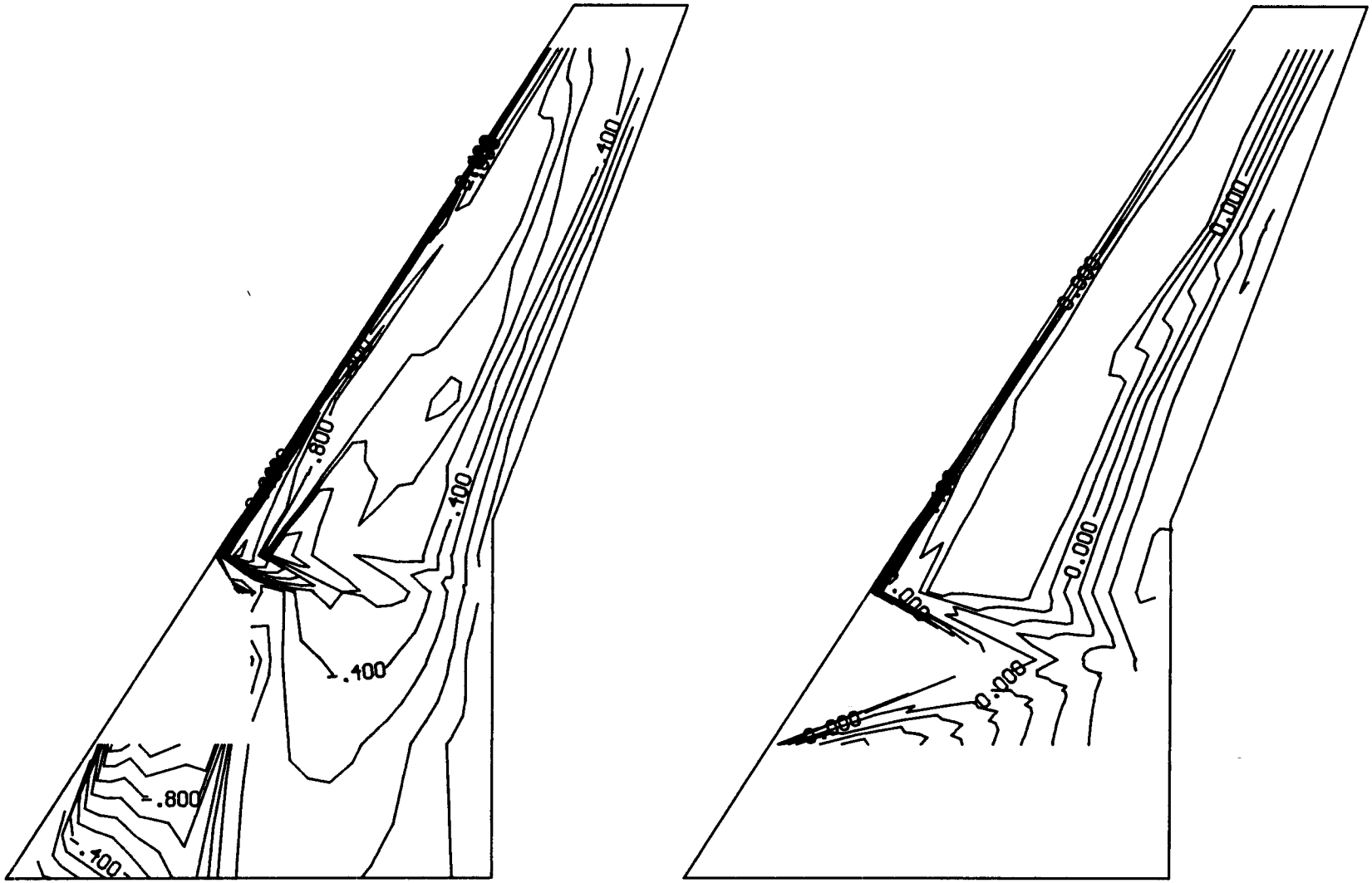

(d) USBC-F.

Figure 24. Concluded.

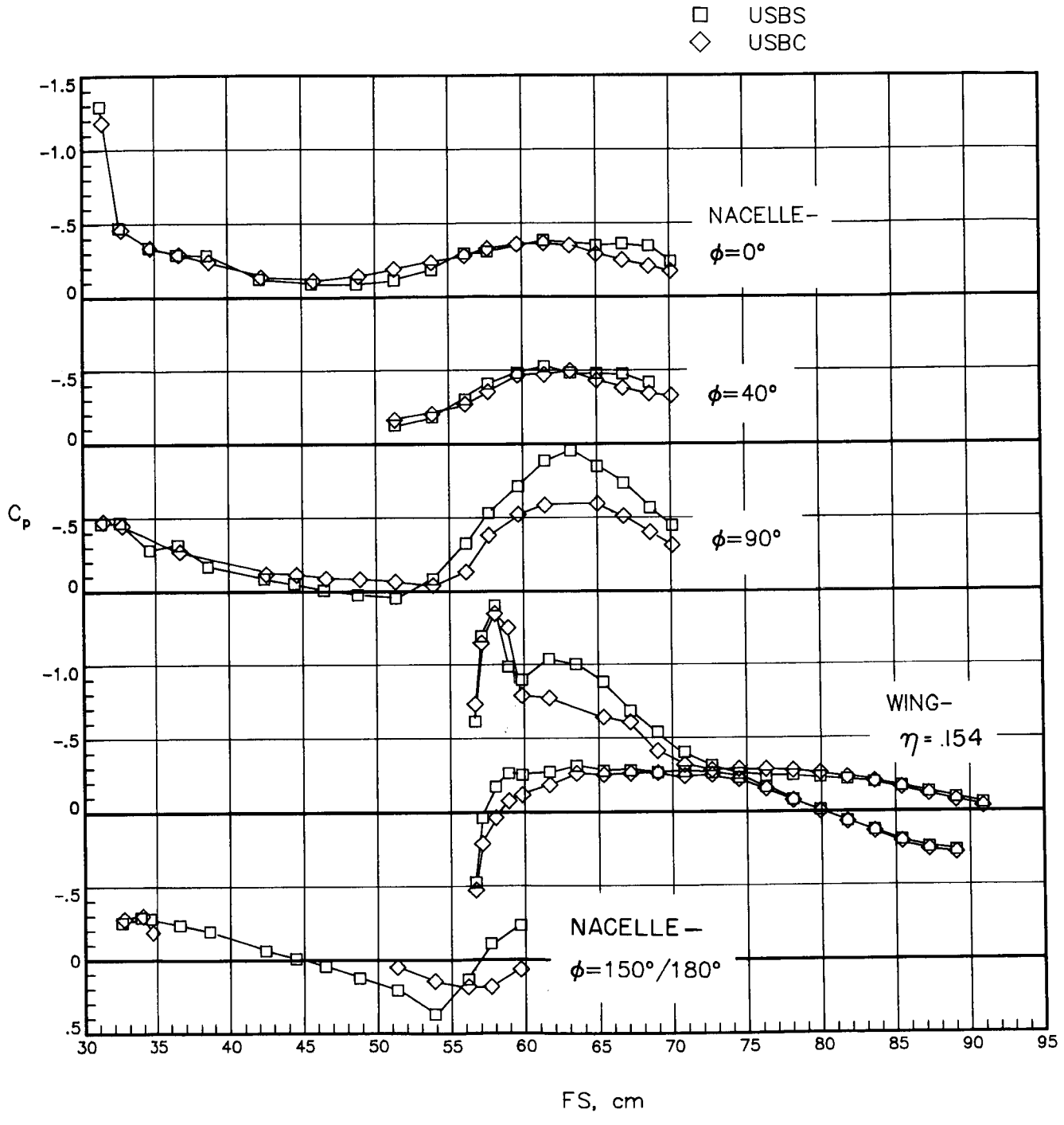

(a) Inboard side.

Figure 25. Effects of nacelle contouring on nacelle pressure distributions at $M_\infty = 0.70$ and $C_L = 0.47$.

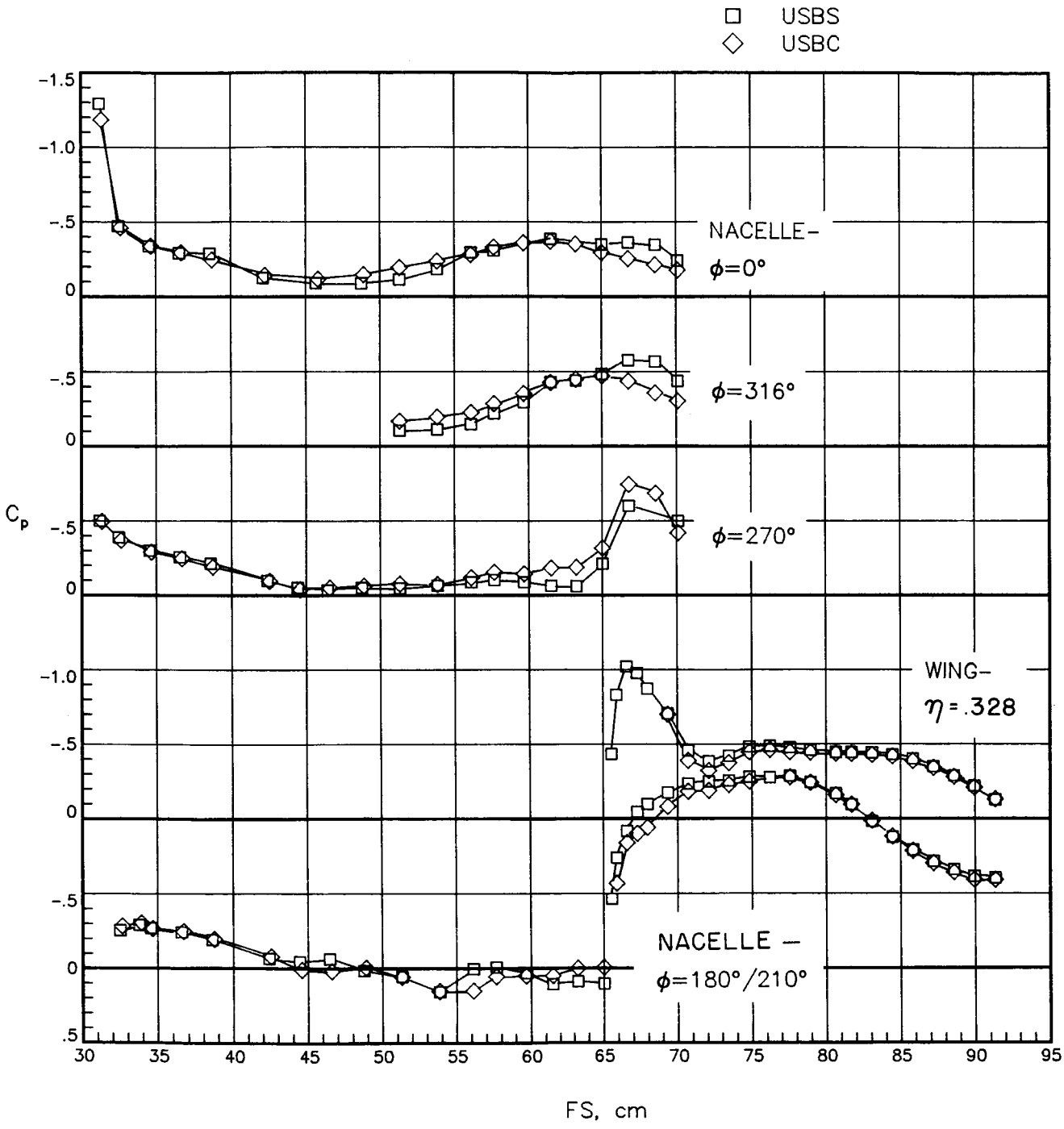

(b) Outboard side.

Figure 25. Concluded.

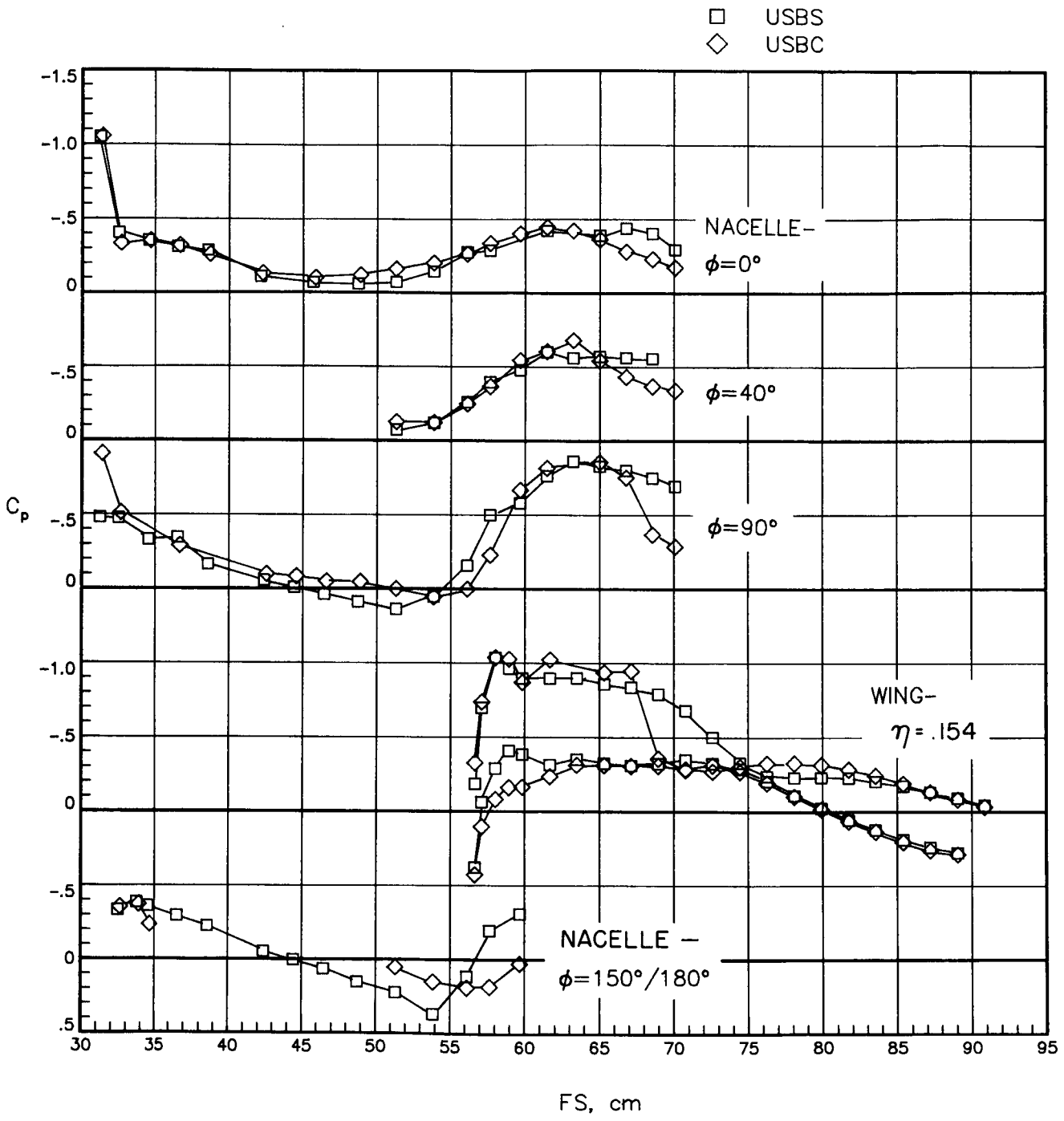

(a) Inboard side.

Figure 26. Effects of nacelle contouring on nacelle pressure distributions at $M_\infty = 0.80$ and $C_L = 0.44$.

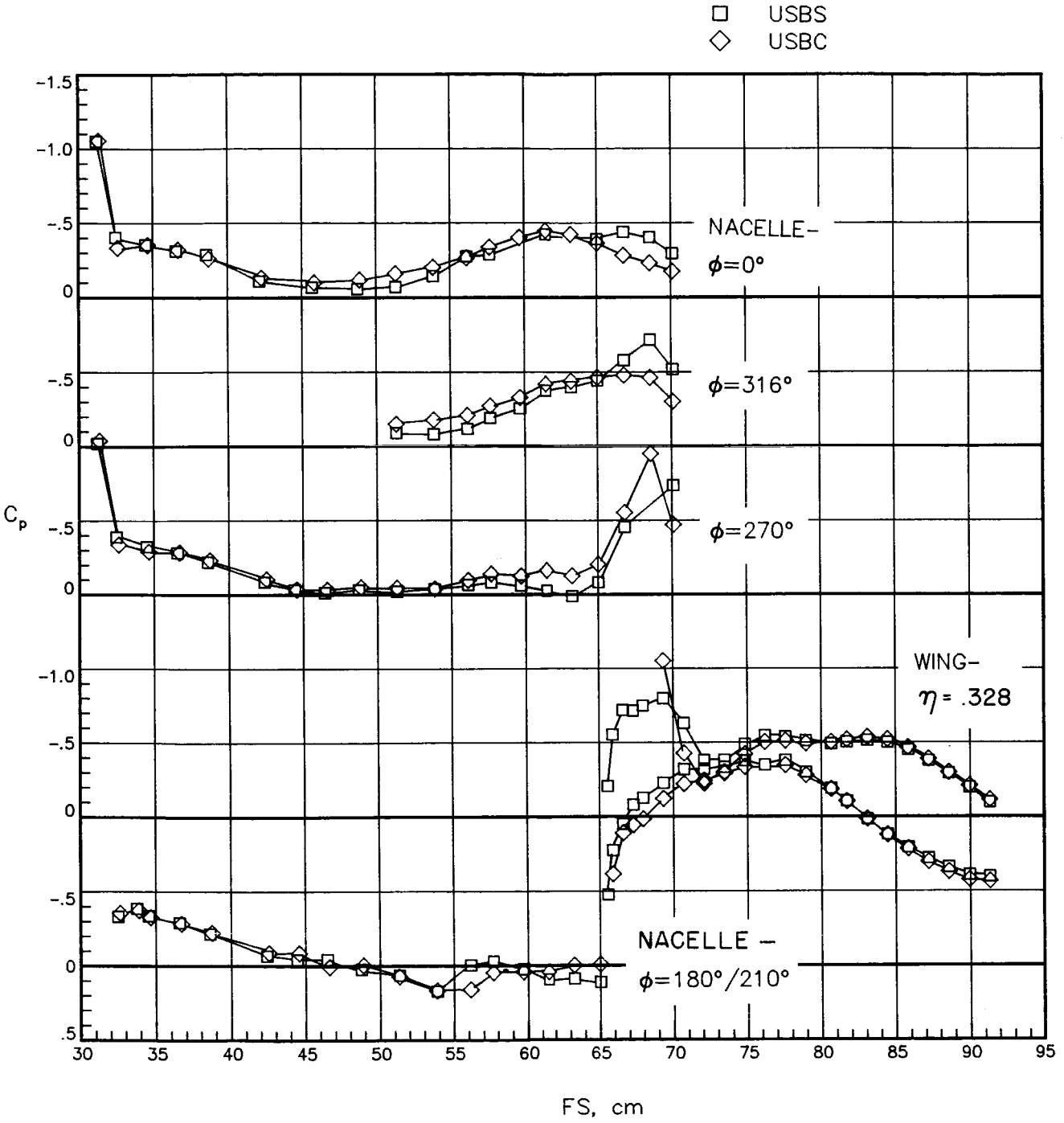

(b) Outboard side.

Figure 26. Concluded.

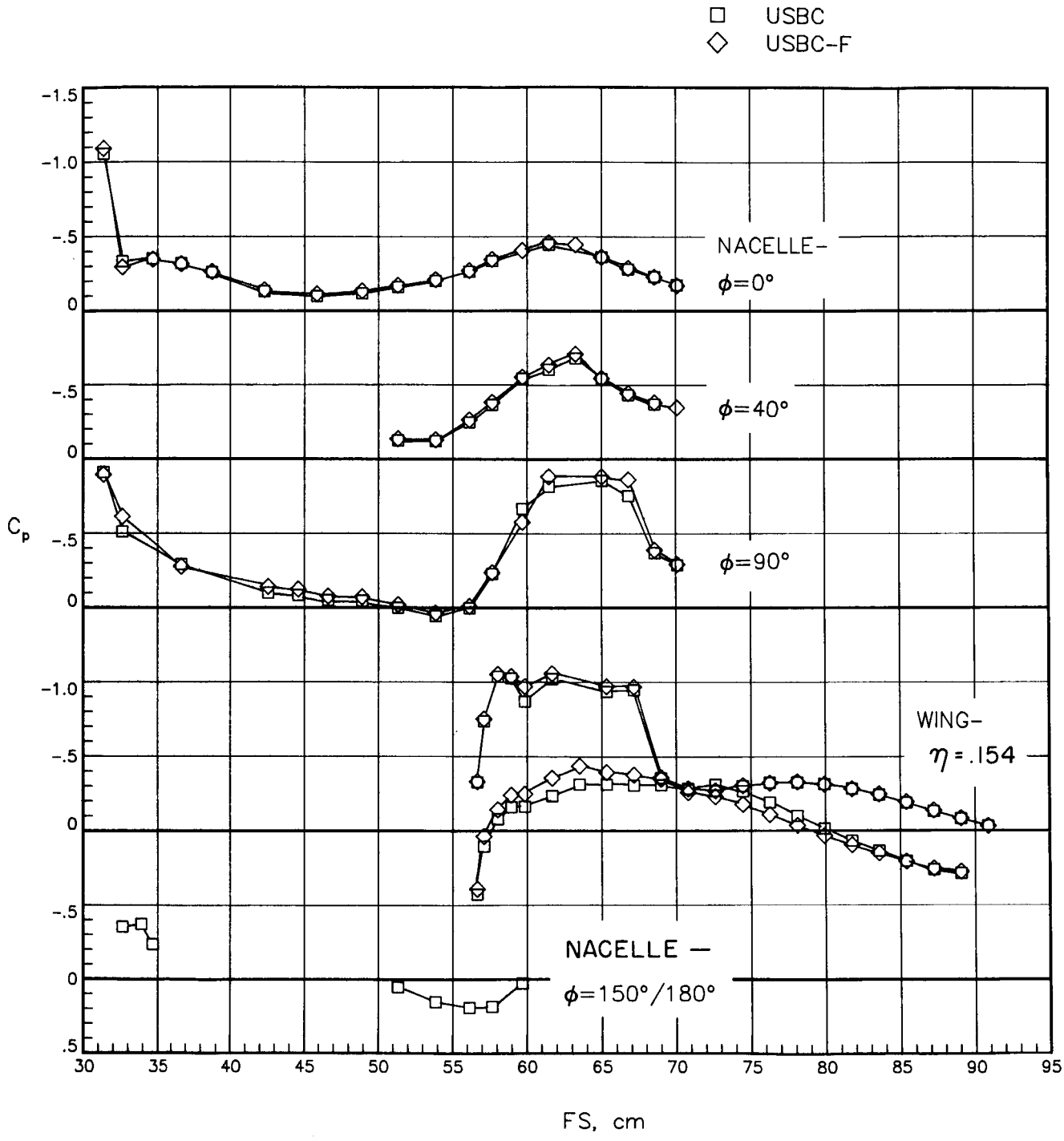

(a) Inboard side.

Figure 27. Effects of fairing on contoured nacelle pressure distributions at $M_\infty = 0.80$ and $C_L = 0.45$.

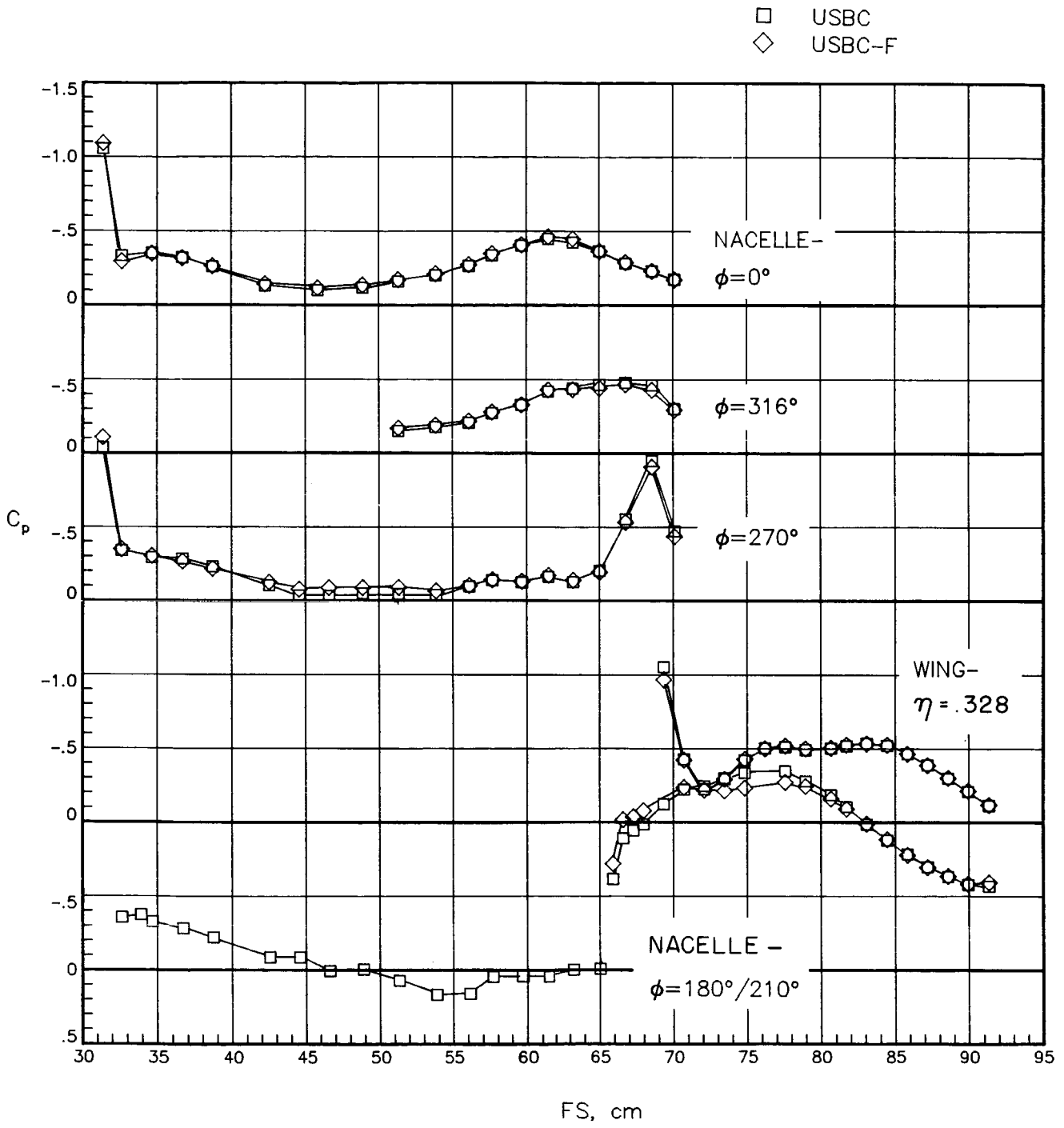

(b) Outboard side.

Figure 27. Concluded.

1. Report No. NASA TP-2579	2. Government Accession No.	3. Recipient's Catalog No.
4. Title and Subtitle Effects of Upper-Surface Nacelles on Longitudinal Aerodynamic Characteristics of High-Wing Transport Configuration		5. Report Date April 1986 6. Performing Organization Code 505-62-91-01
7. Author(s) Lawrence E. Putnam		8. Performing Organization Report No. L-16062
9. Performing Organization Name and Address NASA Langley Research Center Hampton, VA 23665-5225		10. Work Unit No. 11. Contract or Grant No.
12. Sponsoring Agency Name and Address National Aeronautics and Space Administration Washington, DC 20546-0001		13. Type of Report and Period Covered Technical Paper 14. Sponsoring Agency Code

15. Supplementary Notes

16. Abstract

An investigation has been conducted in the Langley 16-Foot Transonic Tunnel to determine the effects of installing and streamline contouring upper-surface nacelles on the longitudinal aerodynamic characteristics of a high-wing transport configuration. Also investigated were the effects of adding a fairing under the nacelle. The investigation was conducted at free-stream Mach numbers from 0.60 to 0.83 at angles of attack from $-2°$ to $4°$. Flow-through nacelles were used. Streamline contouring the nacelles substantially reduced the interference drag due to installing the nacelles.

17. Key Words (Suggested by Authors(s))
Transonic speeds
Transport airplanes
Upper-surface nacelles
Longitudinal aerodynamic characteristics
Streamline contouring

18. Distribution Statement
Unclassified—Unlimited

Subject Category 02

19. Security Classif.(of this report)	20. Security Classif.(of this page)	21. No. of Pages	22. Price
Unclassified	Unclassified	68	A04

For sale by the National Technical Information Service, Springfield, Virginia 22161

NASA-Langley, 1986